Master's thesis

NTNU
Norwegian University of Science and Technology
Faculty of Natural Sciences
Department of Materials Science and Engineering

Jan Eskil Flåm

Wire Arc Additive Manufacturing of an Al-Mg Aluminium Matrix Nanocompsite

Master's thesis in Chemical Engineering and Biotechnology
Supervisor: Hans Jørgen Roven
June 2020

NTNU
Norwegian University of
Science and Technology

Jan Eskil Flåm

Wire Arc Additive Manufacturing of an Al-Mg Aluminium Matrix Nanocompsite

Master's thesis in Chemical Engineering and Biotechnology
Supervisor: Hans Jørgen Roven
June 2020

Norwegian University of Science and Technology
Faculty of Natural Sciences
Department of Materials Science and Engineering

NTNU
Norwegian University of
Science and Technology

I Preface

This master's thesis has been written during spring 2020 at the Department of Materials Science and Engineering, NTNU.

I hereby declare that this master's thesis is written independently and in accordance with regulations at NTNU.

Jan Eskil Flåm
NTNU, Trondheim
June 2020

II Acknowledgements

As this thesis conclued a master' degree in Materials Science at the Norwegian University of Science and Technology in Trondheim, i would like to thank the following persons for help and guidance in completing this thesis:

Supervisor Professor Hans Jørgen Roven (NTNU), for clarifying discussions and introduction to the field of screw extruded aluminium alloys.

Co-supervisor PhD-candidate Geir Langelandsvik (SINTEF), for invaluable guidance during experiments, in addition to countless technical and theoretical discussions on relevant as well as irrelevant topics.

Researcher Stein Rørvik for performing Micro X-Ray computational tomography, Chief Engineer Pål Christian Skaret for performing tensile testing and Senior Engineer Yingda Yu for assistance with scanning electron microscopy.

III Aim

The aim of this master's thesis is to use an aluminium matrix nanocomposite wire manufactured by metal continuous screw extrusion (MCSE) for wire arc additive manufacturing (WAAM). The wire is reinforced with titanium carbide nanoparticles for strength enhancement. An uniform distribution of the titanium carbide nanoparticles in the additive manufactured component is imperative for isotropic mechanical properties throughout the component. A study of nanoparticle interaction during solidification is performed in order to gain knowledge about microstructure, porosity and oxide content. Additionally, processing parameters during MCSE and WAAM will be investigated to determine if there is a correlation to mechanical properties of additive manufactured components.

IV Abstract

The aim of this study was to utilize extruded 10 mm profiles from metal continuous screw extrusion (MCSE), a novel solid-state production method, for wire arc additive manufacturing (WAAM) of an aluminium matrix nanocomposite thin wall using cold metal transfer (CMT) technology.

In this thesis, an extruded 10 mm diameter profile of an AA5183 aluminium-magnesium alloy reinforced with 3 wt% titanium carbide (TiC) nanoparticles (and one without reinforcement were drawn and shaved to a 1.2 mm welding wire for wire arc additive manufacturing (WAAM) of a 233x8x84 mm^3 thin wall on a AA6082 base plate. One-third of the wall was deposited without nanoparticle addition, for comparison. The microstructure of the WAAM thin wall was characterised using optical light microscopy. Porosity was investigated using micro X-Ray computational tomography (microCT) and scanning electron microscopy (SEM). Vickers microhardness and tensile strength were investigated to assess mechanical properties of the WAAM component.

Comparison of the wall sections revealed a 86% decrease in grain size due to TiC nanoparticle addition. A decrease in grain size from $64\,\mu\mathrm{m}$ to $9\,\mu\mathrm{m}$ was observed. The TiC-reinforced WAAM section showed equiaxed microstructure, inhibiting the formation of columnar grain structure, whereas the unreinforced section showed large regions with columnar grain growth due to large temperature gradients promoting a columnar grain morphology. TiC nanoparticles were mainly found to agglomerate at grain boundaries, suggesting particle pushing at the solid/liquid interface during solidification in WAAM. *In-situ* formation of the intermetallic phase Al_3Ti was observed, originating from the reaction between TiC nanoparticles and the aluminium matrix occurred due to elevated temperatures during WAAM.

Investigation of porosity showed extreme porosity in the WAAM thin wall with TiC reinforcement particles, 25 vol%. The average pore diameter was estimated to $102\,\mu\mathrm{m}$ for the TiC-reinforced sections, and $42\,\mu\mathrm{m}$ for the unreinforced section. It is assumed that several factors contribute to porosity in the WAAM thin wall, such as: high oxide amount, hydrogen storage capacity of TiC nanoparticles, as well as processing parameters during MCSE and WAAM.

Mechanical testing showed a Vickers microhardness of 88 $HV_{0.1}$ for the TiC-reinforced section. Tensile testing showed anisotropic tensile properties throughout the WAAM thin wall, demonstrating a higher ductility 5.9 $\%EL$ and ultimate tensile strength (σ_{UTS}) of 179 MPa parallel to the deposition direction (x), compared to 2.7 $\%EL$ and 118 MPa in the perpendicular deposition direction (z). The extreme porosity is believed to be the main contributor to poor tensile properties.

By carefully tailoring aluminium matrix nanocomposites through nanoparticle selection, porosity mitigation and processing parameters, significant strength enhancement is possible for additive manufactured components in the future.

V Sammendrag

Målet med denne studien var å benytte 10 mm ekstrudatprofiler fra kontinuerlig skrueekstrusjon av metaller (Metal Continuous Scew Extrusion, MCSE), en ny metode for fast tilstandsproduksjons av metalltråd for additiv tilvirkning av en aluminium matriks nanokompositt tynnvegg ved bruk av kaldmetalloverføringteknologi (CMT). I denne masteroppgaven ble et titankarbid-forsterket 10 mm ekstrudat av AA5183 aluminium-magnesium-legering benyttet, samt et AA5183 ekstrudat uten forsterkning. Ekstrudatene ble trukket og barbert ned til 1.2 mm diameter sveisetråd for additiv tilvirkning med metalltråd og lysbue av en 233x8x84 mm^3 tynnvegg på en AA6082 baseplate. En tredjedel av veggen ble deponert uten titankarbid nanopartikkel-forsterkning for sammenligning. Mikrostrukturen i tynnveggen ble karakterisert ved bruk av optisk lysmikroskopi. Porositet ble undersøkt ved micro X-ray computational tomography (micro-CT) og scanning electron microscopy (SEM). Vickers mikrohardhet og mekanisk styrke ble undersøkt for å vurdere komponentens mekansike egenskaper.

Sammenligning av de to seksjonene i veggen viste en nedgang på 86% i kornstørrelse ved tilsats av titankarbid nanopartikler til AA5183-legeringen. En nedgang i kornstørrelse fra $64\,\mu\mathrm{m}$ til $9\,\mu\mathrm{m}$. Den titankarbid-forsterkede delen av veggen viste likeakset mikrostruktur, hvorledes den uforsterkede delen viste store områder med kolumnær kornstruktur grunnet store temperaturgradienter innad i materialet, som hindret kolumnær til likeakset overgang. Titankarbid nanopartikler ble hovedsaklig funnet agglomerert på korngrensene, som tyder på partikkelskyving under den raske størkningen av fast/flytende grensesenittet. Formasjon av intermetallisk Al_3Ti ble observert, med opprinnelse fra kjemisk reaksjon mellom titankarbidpartiklene og aluminiumsmatriksen ved høye temperaturer.

Undersøkelse av porositet viste ekstrem poredannelse i tynnveggen, hele 25%. Gjennomsnittlig porediameter ble estimert til $102\,\mu\mathrm{m}$ for den titankarbid-forsterkede delene av tynnveggen, og $42\,\mu\mathrm{m}$ for den uforsterkede delen. Det er antatt at flere faktorer bidrar til porositet i tynnveggen, slik som: høyt oksidinnhold, hydrogenlargrinskapasitet i titankarbidpartikler, samt prosessparametere under ekstrudering og additiv tilvirkning.

Mekanisk testing viste en Vickers microhardhet på 88 $HV_{0.1}$ for den titankarbid-forsterkede delen. Strekktesting viste anisotropiske strekkegenskaper gjennom hele tynnveggen, med en forlengelse på 5.9 EL og strekkfasthet på 179 MPa parallelt på deponeringsretningen (x), sammenlignet med en forlengelse på 2.7 EL og strekkfasthet på 118 MPa i vinkelrett på deponeringsretningen. Den ekstreme porositeten er antatt å være hovedårsak til svake strekkegenskaper.

Ved å tilpasse aluminiummatriks nanokompositter gjennom valg av nanopartikler, begrense porositet og tuning av prosessparametere, kan en signifikant forbedring av additivt tilvirkede komponenter være mulig i fremtiden.

Table of Contents

I Preface **i**

II Acknowledgements **iii**

III Aim **v**

IV Abstract **vii**

V Sammendrag **i**

Table of Contents **v**

1 Introduction **1**

2 Literature review **3**
- 2.1 Aluminium . . . 3
  - 2.1.1 Aluminium demand and supply . . . 3
  - 2.1.2 The Al-Mg system . . . 5
  - 2.1.3 Oxidation of Al-Mg alloys . . . 7
- 2.2 Composite materials . . . 9
  - 2.2.1 Metal Matrix composites . . . 9
  - 2.2.2 Aluminium matrix composites . . . 10
- 2.3 Strengthening mechanisms . . . 11
  - 2.3.1 Hall-Petch strengthening . . . 12
  - 2.3.2 Orowan strengthening . . . 13
  - 2.3.3 Coefficient of thermal expansion (CTE) mismatch strengthening . . . 13
  - 2.3.4 Load transfer effect . . . 13
  - 2.3.5 Elastic modulus mismatch (EM strengthening) . . . 14
  - 2.3.6 Total strength contribution . . . 14
- 2.4 Strengthening by ceramic nanoparticles . . . 14
  - 2.4.1 Edge-to-edge match . . . 14
  - 2.4.2 Heterogeneous nucleation . . . 15
- 2.5 Screw Extrusion . . . 17
  - 2.5.1 Metal Continuous Screw Extrusion . . . 17
- 2.6 Additive manufacturing . . . 19

2.6.1 Additive manufacturing technologies 20
2.6.2 Wire and arc additive manufacturing (WAAM) 21
2.6.3 Cold Metal Transfer (CMT) 23
2.7 Additive manufacturing of aluminum alloys 24
2.7.1 Solidification of aluminium alloys 24
2.7.2 Porosity in additive manufactured aluminium components 28

3 Experimental **31**
3.1 Extrudate material 32
3.2 Drawing and shaving of extrudate 34
3.3 Heat treatment of extrudate and welding wire 34
3.4 Wire arc additive manufacturing 35
3.5 Sample preparation 35
3.5.1 Microscopy images 36
3.5.2 Micro X-Ray computational tomography 38
3.5.3 Tensile testing 38
3.5.4 Microhardness 38
3.6 Additional work on AA6082 aluminum alloy 40

4 Results **41**
4.1 Heat-treatment of feedstock material 41
4.1.1 MCSE extrudate 10 mm profiles 41
4.1.2 Welding wire 1.2 mm 42
4.2 Macroscopic appearance of WAAM thin wall 45
4.3 Microstructure 45
4.4 Distribution of titanium in the aluminium matrix composite 48
4.5 Porosity 52
4.6 Microhardness 58
4.7 Tensile properties 59

5 Discussion **61**
5.1 Heat-treatment of feedstock material 61
5.1.1 MCSE 10 mm extrudate profiles 61
5.1.2 Welding wire 1.2 mm 62
5.2 Macroscopic appearance of WAAM thin wall 62
5.3 Microstructure 63
5.3.1 Solidification behaviour in WAAM thin wall 63
5.3.2 Effect of thermal conductivity of nanoparticle during solidification . . . 66
5.3.3 Nanoparticle inhibition of grain growth 70
5.3.4 Intermetallic Al_3Ti phase 71
5.4 Porosity 73
5.4.1 Oxides 74
5.4.2 TiC nanoparticles 76
5.4.3 WAAM parameters 78
5.5 Microhardness 80
5.6 Tensile properties 80
5.7 Other ceramic nanoparticles for use in aluminium matrix composites 84

6 Conclusion 87

7 Further work 89

References 89

Appendices 105

A AA6082 aluminium alloy 105
A.1 Preparation of material 105
A.2 Nanoparticle coating 106
A.3 Metal continuous screw extrusion 106

B Identification of phases by EDS point analysis 107

C Characterization of AA5183 heat-treated welding wires 110

D Additional SEM images of porosity 113

Chapter 1

Introduction

The demand for aluminium alloys in industrial applications is expected to increase at an annual rate of 3.2% from 2019 to 2026 [1]. Aluminium alloys are increasingly in demand in automotive, aerospace, agriculture, marine and defence industries, owing to their great combination of structural integrity, high strength, resistance to corrosion and light weight [2]. In recent years, environmental concerns has led to escalating focus on green-house gas reductions, pushing for lower fuel consumption in the transport sector and higher efficiency in other industrial sectors [3]. Conventional aluminium alloys often fall short when strength to weight ratio is considered. Development of new and improved materials is required to meet recent developments in environmental awareness, as well as new frontiers in space exploration and the aerospace industry.

Aluminium matrix composites (AMC) are a promising group of advanced materials, possessing improved mechanical properties such as superior strength to weight ratio, high strength, excellent corrosion resistance and good ductility. AMCs are made by reinforcing the aluminium matrix by adding particles or fibers, often ceramic materials. Existing production methods for AMCs are highly energy demanding, often involving remelting of metal before the reinforcement material is added to the melt [4]. In addition, obtaining an even distribution of particles in the solidified structure has been challenging, often combined with formation of secondary phases through chemical reactions with the aluminium matrix [5, 6].

A novel solid-state production method mitigating the necessity of a remelting step is metal continuous screw extrusion (MCSE), developed at *NTNU - Norwegian University of Science and Technology* in close collaboration with one of the leading aluminium producers worldwide, *Norsk Hydro* [7]. MCSE is seen as a promising production method for several aluminium alloys in the future [6, 8, 9, 10, 11]. The feasibility of environmentally friendly solid-state production of AMCs has proven interesting, especially for the production of strengthening enhanced welding wire for additive manufacturing [12].

Additive manufacturing (AM) has long been expected to radically change the manufacturing industry, and has in recent years increased its presence globally [2]. The evolving AM technology offers production of geometrically complex structures, reducing weight, emissions and cost for manufacturers, as well as consumers [13]. Production time varies with a wide range of technologies being available. Metal powder-based processes offers good precision at a low deposition rate of $0.6\,\mathrm{kg\,h^{-1}}$, in addition to being highly energy demanding. Mentioned properties are not well-suited for large-scale industrial production of components [14, 15].

More efficient AM technologies has been developed, with wire arc additive manufacturing

(WAAM) being the most promising technology for large-scale production. The low production time achievable by a $10\,\mathrm{kg\,h^{-1}}$ deposition rate, combined with high raw material utilization renders WAAM technology favorable for several industries [15].

However, the emerging WAAM technology presents several challenges related to rapid solidification during deposition. High porosity regions and columnar grain structure are desirably avoided, as the mechanical properties of the material are impaired by anisotropy [16]. By using cold metal transfer (CMT) deposition technique, the solidification process can be controlled to a certain extent, by controlling heat input. Lower heat input during deposition reduces the temperature gradient in the material, thus leading to grain refinement of WAAM-CMT aluminium matrix nanocompsites [17].

In this study, a WAAM thin wall of a titanium carbide (TiC) reinforced AA5183 aluminium alloy will be manufactured from MCSE extrudate profiles using CMT-technology. Microstructure, porosity and mechanical properties will be explored in detail.

Chapter 2

Literature review

Parts of the literature in sections 2.1, 2.6 and 2.7 are taken from the authors' preliminary project thesis [18]. The literature has been reviewed and identified as relevant background material. The material is amended with new publications and information found relevant to this thesis.

2.1 Aluminium

2.1.1 Aluminium demand and supply

Aluminium is the most consumed non-ferrous metal in the world, with annual production at 64 million tonnes of primary aluminium in 2018, illustrated by Figure 2.1. The production of recycled aluminium was close to 32 million tonnes for 2019 [19]. Aluminium alloys offer high strength and low weight in combination with good corrosion resistance, properties that has experienced increased demand in recent years [20].

In the recent two decades, demand for primary and recycled aluminium has strongly been driven by China, as rapid developing trends within lightweight automotive constructions, as well as increased consumption of aluminium in the aerospace industry is booming [21]. Going forward, the automotive industry is a key growth driver for the aluminium industry, as aluminium has received increasing attention in recent years due to political pressure to reduce green-house gas emissions by using lightweight materials. Weight reduction is a strong contributor to increasing the range of electric cars, which has led to several car manufacturers replacing steel with aluminium [22]. Aluminium used in automotive applications are estimated to lower fuel consumption by 5-7% for every 10% weight reduction by substituting steel [23]. According to the market analyser CRU, utilization of aluminium will rise by 15-27% in electric vehicles, compared to internal combustion engine cars. Plug-in hybrid and full battery electric vehicles already use 25-27% more aluminium than the typical internal combustion engine car today [24]. The series-produced car on the market with highest aluminum content is the *Tesla Model S*, containing 661 kg of aluminium in total [25]. In light of megatrends such as electrical vehicles, light weight materials and additive manufacturing, new applications employing aluminium materials are increasingly sought-after.

Today, all primary aluminum is manufactured by the *Hall-Heroult* process, an electrolytic reduction process. Aluminum oxide is (Al_2O_3) produced by the *Bayer process* and dissolved in molten cryolite (Na_3AlF_6) at temperatures ranging from 950–970 °C, then carbothermally reduced to aluminum in an electrolysis cell [27]. The process is highly energy intensive because

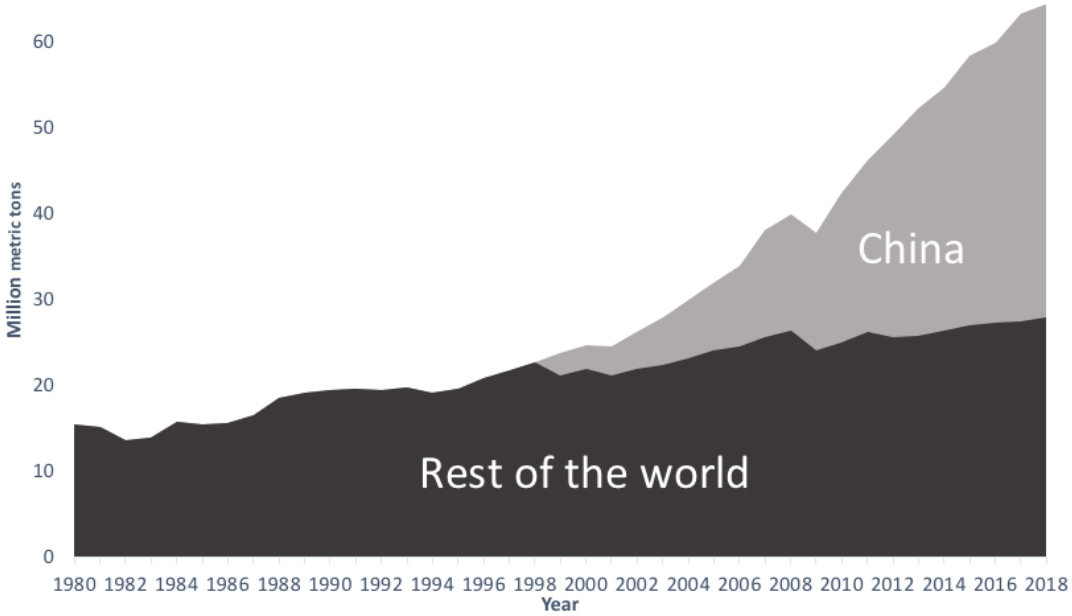

Figure 2.1: Global annual production of primary aluminium from 1980 to 2018, showing a total of 64 million tonnes produced in 2018. China alone produced 36 million tons of primary aluminium in 2018, 56% of the global production [26].

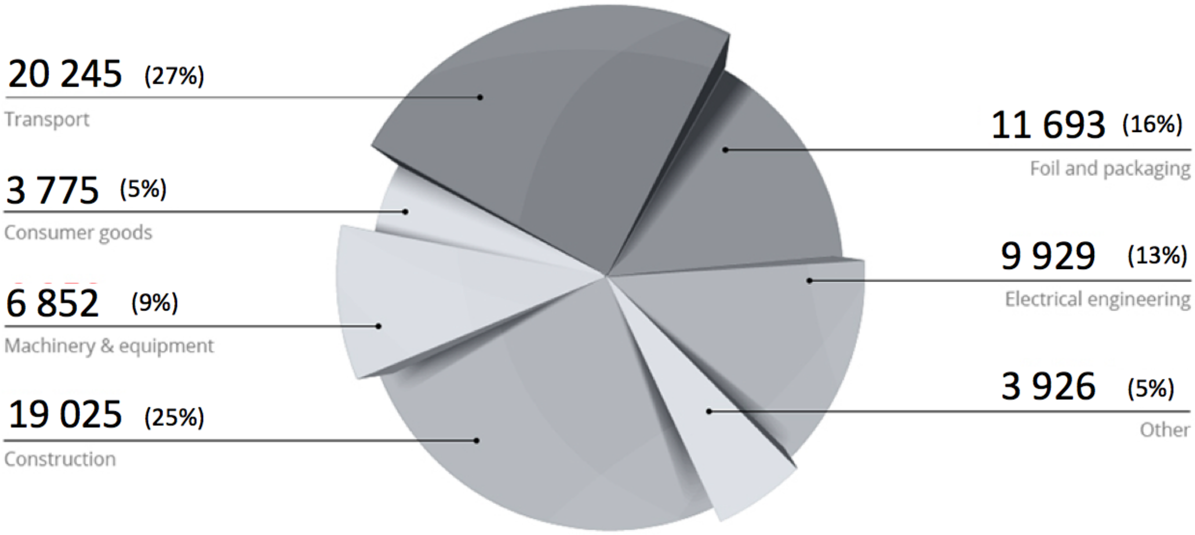

Figure 2.2: Aluminium consumption by industry.

oxygen has a high affinity for aluminum, preventing aluminium to appear naturally in its elemental form. Aluminium is always found in oxide form. The production of 1 kg of aluminum requires 4 kg of bauxite and about 14 kWh of electrical energy [28].

Commercially pure aluminium contains 99.5–99.8% aluminium, and have a modulus of elasticity at 71 GPa, a third of the value for steel. The density for aluminum is $2.7\,\mathrm{g\,cm^{-3}}$, a third of the density of steel. Aluminum has a FCC crystal structure, which causes the metal to have lower strength compared to BCC steel. In FCC metals, the internal resistance to dislocation slip is very small, due to *Peierls stress forces*. To achieve high strength in aluminium, alloying elements are added to provide solid solution hardening or precipitation hardening [28]. The alloys are classified according to their major alloying elements as shown in Table 2.1.

Table 2.1: Classification of wrought aluminium alloys based on the major alloying element [27].

Wrought alloys	
Major alloying element	**Series**
Pure Al (min. 99%)	1xxx
Copper	2xxx
Manganese	3xxx
Silicon	4xxx
Magnesium	5xxx
Magnesium and silicon	6xxx
Zinc	7xxx
Other elements	8xxx
Unused	9xxx

Another classification of aluminium, is with respect to the fabrication process, *cast* or *wrought*. Cast alloys typically contains high amount of alloying elements, and is normally casted close to the eutectic composition. Wrought alloys are typically low-alloyed, and hot or cold worked without remelting, e.g extrusion, drawing and forging. Wrought alloys are delivered in form of slabs, billets or rods [27].

2.1.2 The Al-Mg system

Aluminium with magnesium (Mg) as primary alloying element is designated as a 5xxx-alloy. 5xxx-series aluminium alloys are non-heat-treatable, i.e not hardenable by precipitation hard-

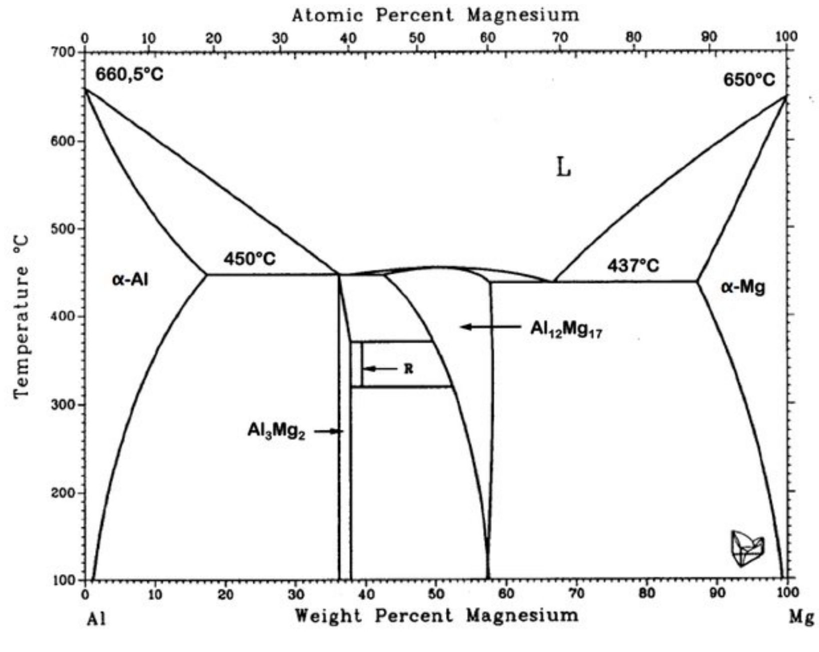

Figure 2.3: Al-Mg binary phase diagram. Obtained from [28].

ening [20]. Magnesium has lower density than aluminium at a value of $1.7\,\mathrm{g\,cm^{-3}}$, resulting in an alloy that is lighter due to its low total density [27].

Figure 2.3 shows the binary phase diagram for Al-Mg. The solid solubility of Mg in Al increases up to 18.9 wt% at a temperature of 450°C. Al-Mg alloys are normally held below 5 wt% Mg to avoid the formation of the unwanted β-$\mathrm{Mg_5Al_8}$ phase at grain boundaries. The β-phase is brittle, and anodic relative to the Al-Mg-phase, making the material prone to intergranular corrosion and deteriorating mechanical properties [27]. At concentrations below 5 wt% Mg, the alloy exhibits good corrosion properties because Mg diffuses to become part of the protective oxide film on the material surface [20].

Most Al-Mg alloys used commercially exhibit saturation of Mg in solid solution, giving rise to solid solution hardening and strain hardening. The strengthening by addition of Mg is related to the larger atomic radius of Mg compared to Al, giving rise to strain fields in the lattice, impeding dislocation mobility during deformation of the alloy [20]. Al-Mg alloys show increasing ultimate tensile strength (σ_{UTS}) with increasing magnesium content up to about 20 wt% Mg. The tensile elongation decreases for small additions of magnesium, typically 1-2 wt% Mg. The strength is mainly developed through work hardening, illustrated in Figure 2.4 by the rapid increase in ultimate tensile strength (σ_{UTS}) compared to yield strength [29].

A major strength contribution in 5xxx alloys is the effect of grain size. The effect of grain size is larger in Al-Mg than most other aluminium alloys [30]. The mobility of dislocations is hindered by grain boundaries, as the dislocations cannot continue slip motion into another grain due to different orientation of the slip planes. This allows grain boundaries to act as barriers by piling up dislocations close to the boundaries. Lower grain size means more grain boundaries, thus contributing to further strengthening. The strength contribution from grain size can be described by the Hall-Petch relation shown by Equation (2.1.1) [27].

$$\sigma_Y = \sigma_f + k_1 d^{-m} \tag{2.1.1}$$

Where σ_f is the frictional stress, k a material specific constant related to the difficulty of slips across grain boundaries, d is the grain size and m is a material specific constant, typically $1/2$ for grain size hardening.

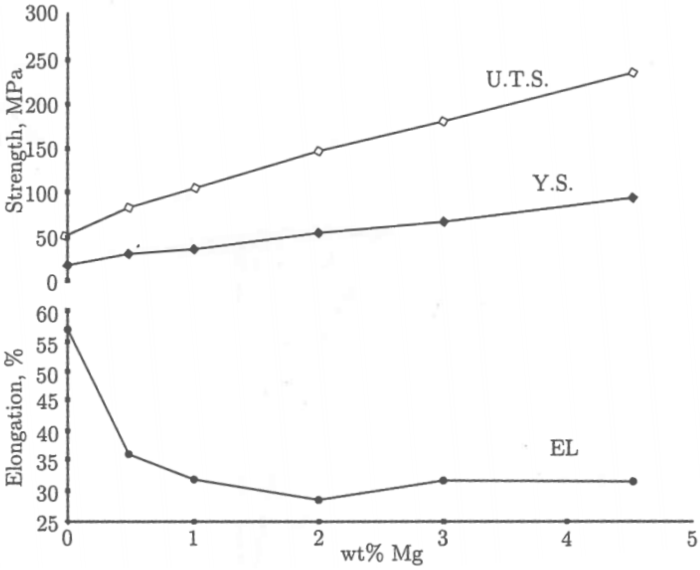

Figure 2.4: Effect on tensile properties from magnesium in Al-Mg alloys. Obtained from [31].

2.1.3 Oxidation of Al-Mg alloys

Al-Mg alloys are know to oxidize, forming a protective oxide layer on the surface, which improves corrosion resistance in marine environments [32]. Additions of magnesium has shown to be problematic for processing of the alloy, due to more alloy pick-up compared with commercially pure aluminium, as well as problems within machining, adhesion and ageing of applied organic films such as paints and adhesives. Magnesium is depleted from the bulk material at elevated temperatures, rendering the material frequently poor because of the susceptibility to hydrolyse the magnesium-rich surface oxide [33].

While pure aluminium oxide (Al_2O_3) is an effective barrier against permeation of hydrogen through the oxide layer, magnesium reduces this ability [34, 35]. In aluminium alloys, low hydrogen content is desirable, as hydrogen is the sole contributor to porosity in aluminium alloys [36]. Recently, magnesium based materials have gained increased interest for their ability

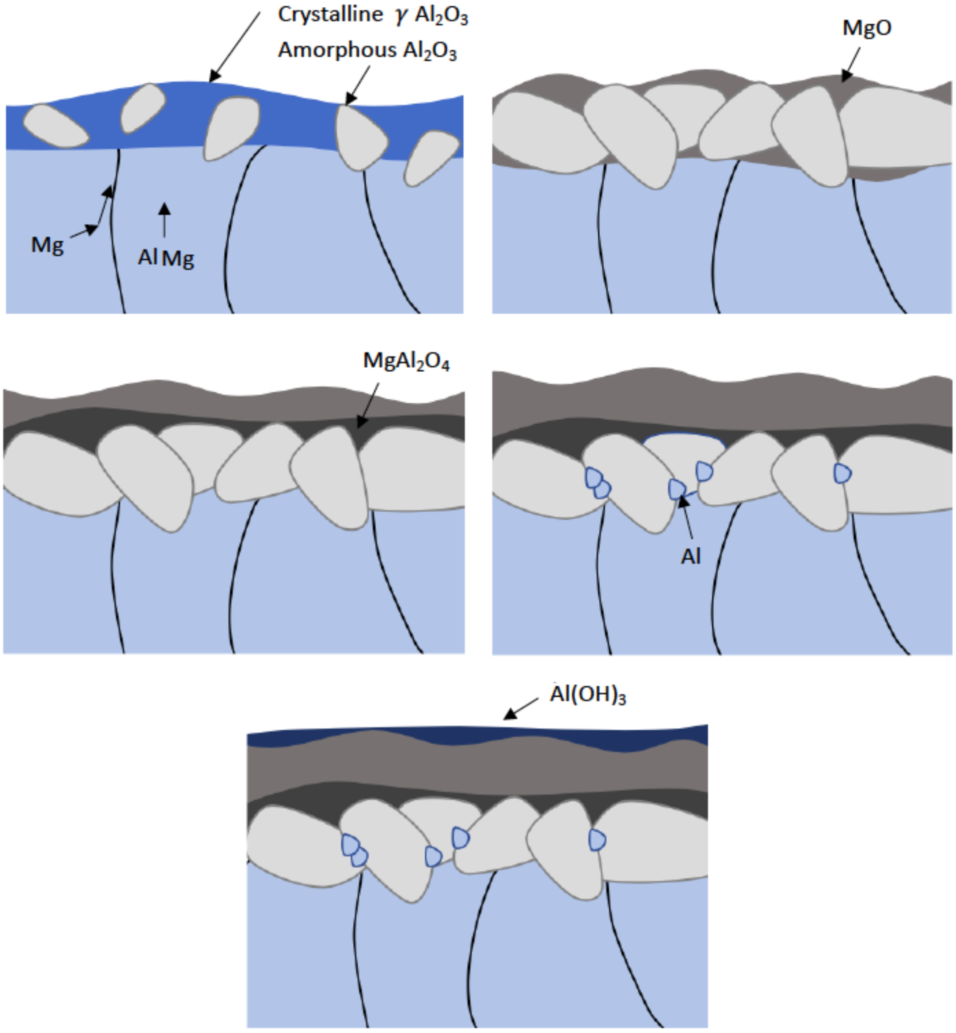

Figure 2.5: Schematic illustration of oxide formation on Al-Mg alloys. Initial γ-Al_2O_3 crystalline oxide film transforms into amorphous Al_2O_3 above 350 °C. Magnesium atoms diffuses through inter-phase boundaries to from a porous MgO layer on top of the Al_2O_3 layer. Magnesium is then oxidizes, forming the spinel structure $MgAl_2O_4$. In humid environments, a top oxide layer of $Al(OH_3)$ will form.

to store hydrogen. Incorporation of magnesium into the alloy increases the hydrogen solubility of the alloy [37].

Common to all aluminium alloys is the initial formation of a amorphous surface oxide layer of Al_2O_3. The oxide film growth is determined by the diffusion of aluminium through the oxide film, as the oxide film itself is impermeable to oxygen, yielding a parabolic variation with time [38]. When the Al-Mg alloy reaches temperatures above 400 °C during processing or heat-treatment, magnesium undergoes outward diffusion into the Al_2O_3 surface layer. This happens as the activation energy required for magnesium diffusion in aluminium is lower than for aluminium itself through both the metal as well as through the Al_2O_3 layer [39]. The initial Al_2O_3 oxide film transitions from a amorphous crystal structure to cubic crystalline γ growth above 350 °C, facilitating the migration of magnesium atoms through the inter-phase boundaries between the amorphous and cubic crystalline alumina oxide layer [40, 41]. A porous layer of MgO film forms on top of Al_2O_3 and grows until it reaches a stationary thickness.

After some time, ranging from a few minutes to several hours and dependent on composition and oxidation conditions, the MgO oxide layer tends to crack due to residual stresses. It then becomes thermodynamically preferable for magnesium to reduce the Al_2O_3 layer that blocks diffusion of magnesium to the top MgO layer. Magnesium then oxidizes by reducing Al_2O_3 to $MgAl_2O_4$. As Al-Mg alloys are stored, especially in humid environments, a hydrated aluminium oxide surface forms, due to $Al(OH)_3$ being thermodynamically preferred above $Mg(OH)_2$. These mechanisms results in lower magnesium content in the bulk of the alloy, reducing the contribution to solid solution strengthening and strain hardening [41]. The oxide layers of a Al-Mg alloy are illustrated in Figure 2.5.

Several methods for inhibition of oxidation has been proposed, e.g. by adding sodium, beryllium, adding CO_2 or N_2 to the atmosphere, or by fast melting [42]. Smith *et al.* [43] reported that 5% CO_2 to air suppressed the onset of oxidation for Al-Mg alloys. CO_2 was shown to adsorb onto the MgO surface, slowing transport of oxygen to the melt.

2.2 Composite materials

A composite material is a material made by combining two or more different materials with significantly different properties. When combined, the material exhibits characteristics from the individual phases, often a ductile matrix phase and a hard dispersed phase. The individual components remain separate and distinct within the composite material, differentiating composites from mixtures and solid solutions [44, 45]. Composite materials are usually classified on the basis of the physical or chemical nature of the matrix or reinforcement phase, illustrated in Figure 2.6 [45].

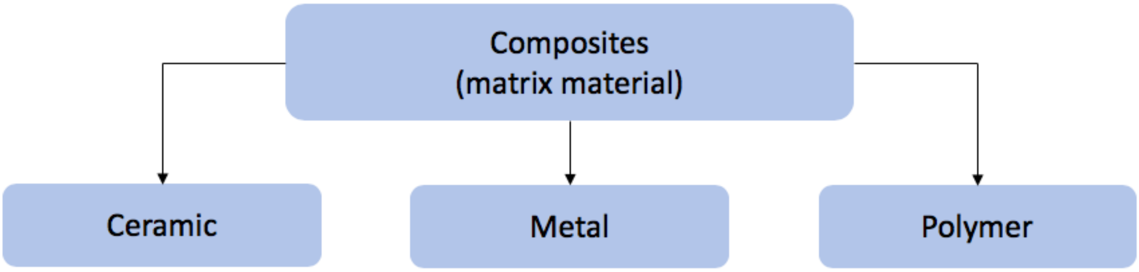

Figure 2.6: Classification of composites based on matrix material.

A ceramic matrix composite is typically brittle and hard. Few slip systems are available, compared to metal matrices. Non-uniform properties are characteristic for ceramic matrix materials, yielding low tensile strength and low thermal and mechanical shock resistance. Ceramic matrix materials are often used for refractory and thermal insulation applications [44].

Polymers are structurally complex, cheap and easily manufactured. Advantages are insulating properties, as thermal and electronic conductivity are poor. Polymers are more resistant to chemicals than most metals. Main drawbacks are low strength and low operating temperature [44].

Metal matrix composites will be discussed in greater detail in the following subsection.

2.2.1 Metal Matrix composites

Metal matrix composites (MMC) are classified as materials in which a continuous metallic phase is combined with a reinforcement phase to enhance the material properties [46].

Metal matrix composites have a wide range of applications, and can be more easily customized than ceramic and polymer matrix composites. Plastic deformation and strengthening mechanisms are advantages of these composites. Metals contain several crystal imperfections such as: point defects (zero dimensional), line defects (uni-dimensional, planar or interfacial (bi-dimensional and volume defects (tri-dimensional). These are defects which can be exploited to enhance strength of the composite. Of largest interest are line defects, often referred to as *dislocations*. It is the presence of dislocations that makes it possible for the metal to plastic deform during high stresses. Grain boundaries are planer defects and is of great importance for mechanical behavior of the material. Volumetric defects are e.g. inclusions, cracks or porosity [44].

MMCs are typically classified on the basis of the reinforcement phase, as described by Figure 2.7. Particle and discontinuous fiber reinforcement phases are considered especially promising, due to low cost and the possibility of isotropic material properties.

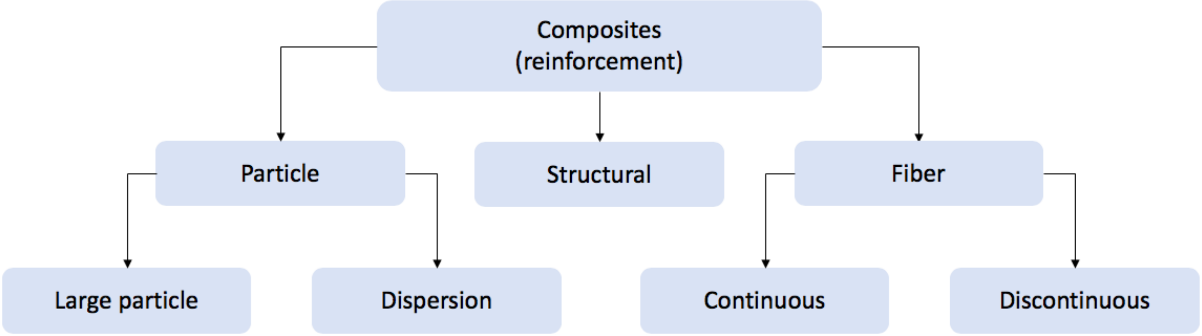

Figure 2.7: Classification of composites based on reinforcement phase.

The first known use of MMCs stretches all the way back to ancient civilizations 9000 years ago. Copper awls found in archaeological excavations in Turkey revealed laminated layers of non-metallic inclusions between layers of copper. Several ancient swords and daggers from Chinese dynasties have been examined in recent years, showing lamination of different metals [47].

Most research in the early days of modern MMCs were carried out by USA and the Soviet Union, mainly related to space and military applications. Important applications in the 1970s and 1980s were graphite reinforced aluminum for use in the antenna of NASA's *Hubble Space Telescope* and Sip/Al composites for electronic packaging in communication satellites. Both the American *Space Shuttle* and the Soviet version *Buran*, as well as the *F-22 Raptor* fighter jet were built with using several MMC components [48]. During the 1980s and 1990s, the automotive industry started incorporating MCCs in several critical parts, driven by Asian manufacturers such as *Toyota*, *Subaru* and *Honda* [3, 49].

The early 2000s saw a increased interest in welding of MMCs. A significant portion of research on MMCs were carried out towards magnesium, aluminium and titanium matrix composites. Main uses of magnesium matrix composites are lightweight brake systems for automotive and aerospace applications, as well as engine parts, gears-boxes and compressors [48]. Application of nanotechnology for enhancement of mechanical and thermal properties gained considerable interest towards the end of the first decade. Introduction of ceramic nanoparticles for strength and stiffness enhancement in aluminium alloys has seen a tremendous spike in interest lately [50].

2.2.2 Aluminium matrix composites

In recent years, demand for aluminium alloys for industrial applications in automotive, aerospace, agriculture and mineral processing industries has increased rapidly owing to their light weight and high performance [51].

Stringent air pollution regulations and a growing focus on environmentally friendly products and services has led to increasing demand for ever-lighter and stronger materials to lower fuel consumption and increase efficiency in many industries [3, 52].

Aluminium matrix composites (AMCs) are promising candidates for strength enhancement combined with reduced weight and increased stiffness. The most used reinforcement phase for use in AMCs are ceramic particles, such as: Al_2O_3, SiC, TiC, TiO_2, B_4C, AlN [45]. The strength of AMCs depends upon several factors such as: composition, grain size, microstructure, strengthening mechanisms and the manufacturing process [53]. Particle reinforcement impart strength to the matrix material even at high temperatures, whereas other strengthening mechanisms (e.g. precipitation hardening) rapidly lose their effectiveness [54].

Industrial applications of AMCs are constantly emerging, a few worth mentioning are [55]: wings, fuselage, supporting structures and engines for the aerospace industry. Pistons, engine blocks, brake rotors, brake discs and shafts for the automotive industry. Increased strength and stiffness of supporting structures in building materials. Good corrosion resistance, high efficient conduction and weight reduction in power transmission lines.

The strength contribution from particle additions to the aluminium alloy is discussed in the subsequent section.

2.3 Strengthening mechanisms

Strengthening of materials is directly related to the materials inherent dislocation mobility. The amount of plastic deformation a material exhibits under external loads depend on the ability of dislocations to move, thus rendering the material harder, stronger and less ductile [56]. Understanding the strengthening mechanisms are not only important for fabrication of high performance aluminium matrix composites, but also important for producing high quality products. The following sections provides a brief overview of different strengthening mechanisms that have been thoroughly researched in the past decades.

A comparison of the various strengthening contributions presented below, is given for TiC in Figure 2.8 and Figure 2.9.

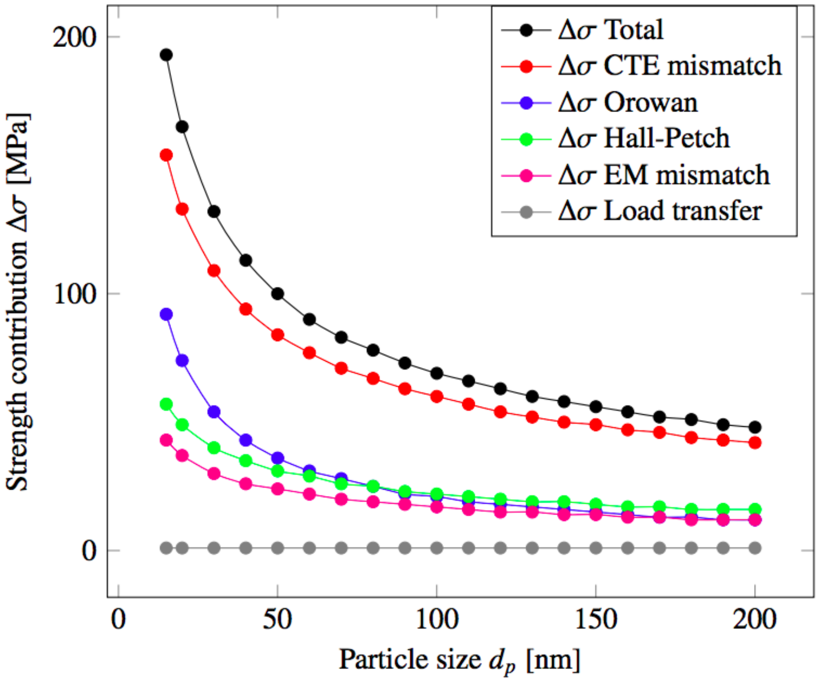

Figure 2.8: Strengthening contribution from TiC nanoparticles in a aluminium matrix at different particle diameters. The volume fraction of TiC nanoparticles are 1%. Figure obtained from [57].

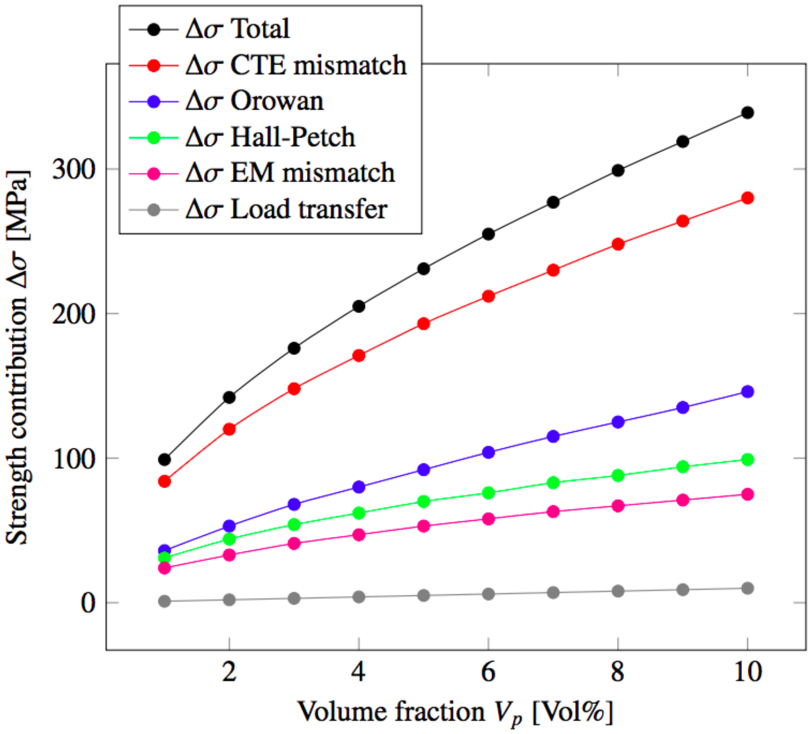

Figure 2.9: Strengthening contribution from TiC nanoparticles in a aluminium matrix at different volume fractions. The particle diameter of TiC nanoparticles are 20 nm. Figure obtained from [57].

2.3.1 Hall-Petch strengthening

Grains in a polycrystalline material will normally have different crystallographic orientations, acting as barriers to dislocation motion. Increasing crystallographic misorientation increases the difficulty for dislocation motion. Reduction of grain size further hinders dislocation motion due to more frequently change of slip system because of higher grain boundary ratio in the material. Dislocation will not always traverse grain boundaries, but rather pile up around the grain boundaries, introducing discontinuity of slip planes between grains. The combined effect results in a strengthened material, where the yield strength, σ_Y varies with grain size according to Equation (2.3.1)

$$\sigma_Y = \sigma_0 + k\frac{1}{\sqrt{d}} \tag{2.3.1}$$

where σ_0 is the lattice friction stress, k is the material specific Hall-Petch coefficient and d is the average grain size. A model to precisely predict the resulting grain size in a material is not found. The effect of *Zener pinning* of nanoparticles is used as a good approximation. Nanoparticles act to prevent the motion of boundaries by exerting a pinning pressure which exerts a drag force hindering motion and sets a upper limit for the grain size according to Equation (2.3.2)

$$d_Z = \frac{4\alpha d_p}{3V_p} \tag{2.3.2}$$

where d_Z is the grain size, d_p is the average nanoparticle diameter, V_p is the volume fraction of nanoparticles, and α is a proportionality constant. From the Zener pinning equation, it is observed that small particles contribute to smaller grain size. The use of nanoparticles to increase the contribution to the strength has been shown to yield promising results [58].

2.3.2 Orowan strengthening

The effect of Orowan strengthening is considered one of the primary strengthening mechanisms in nanoparticle reinforced aluminium matrix composites [4]. In Orowan strengthening, impenetrable particles in the matrix interrupt dislocation migration and thus plastic deformation via interaction with dislocations, which results in increased matrix strength [59]. The Orowan strengthening equation consists of two parameters, namely the interparticle mean free path for dislocation motion and the matrix distortion parameter [59].

In order to prevent dislocation movement, it has been found that small particle spacing yields promising results, due to closer packing. Dislocation movement is hindered by the nanoparticles, they therefore bend around the particles, creating *Orowan dislocation loops* around the nanoparticles. It has been found that a dispersion of nanoparticles in metals can significantly increase creep resistance, even for only a small volume of fractions below 1%, due to the necessary Orowan bowing to bypass the particles [46]. This paricle interaction increases the strength according to eq. (2.3.3)

$$\Delta\sigma_{Orowan} = \frac{0.81MGb\ln(\frac{d_p}{b})}{2\pi\sqrt{1-\nu}d_p(\frac{1}{2}\sqrt{\frac{3\pi}{2V_p}}-1)} \tag{2.3.3}$$

where M is the Taylor factor, G is the matrix shear modulus, b is the Burger's vector and v is the Poisson's ratio.

2.3.3 Coefficient of thermal expansion (CTE) mismatch strengthening

The matrix phase and the reinforcement phase usually have different coefficients of thermal expansion (CTE). Upon cooling, this mismatch results in plastic strain being induced around the nanoparticles in the composite, which leads to increased dislocation density around the particle ambient temperature. The strength contribution from mismatch between aluminum and nanoparticle CTE changes according to Equation (2.3.4) [60].

$$\Delta\sigma_{CTE} = \kappa Gb\frac{12\Delta T\Delta C{V_p}^{1/2}}{bd_p} \tag{2.3.4}$$

where κ is a dislocation strengthening coefficient, G is the shear modulus, b is the Burger's vector, ΔT is the difference in melting and operation temperature and ΔC is the difference in coefficient of thermal expansion between the ceramic and aluminium.

2.3.4 Load transfer effect

The load transfer from the soft aluminium matrix to the stiff and hard nanoparticles under applied external load, contributes to the strengthening of the overall composite. Equiaxed nanoparticles strengthens the composite according to Equation (2.3.5) [61].

$$\Delta\sigma_{LT} = 0.5V_p\sigma_m \tag{2.3.5}$$

where V_p is the volume fraction reinforcement particles, and σ_m is the yield strength of the aluminium base material.

2.3.5 Elastic modulus mismatch (EM strengthening)

The difference in elastic modulus between the nanoparticles and the aluminium base matrix will contribute to strengthening. Plastic derformation of the composite will introduce dislocations around the nanoparicles and increase strenght, due to hindrance of dislocastion sliding. The strength contribution varies according to Equation (2.3.6) [62].

$$\Delta\sigma_{EM} = Gb\lambda\sqrt{\frac{6V_p}{bd_p}\epsilon} \tag{2.3.6}$$

where ϵ is uniform strain deformation and λ is a dislocation strengthening coefficient.

2.3.6 Total strength contribution

Summing each individual strength contribution gives the total strength contribution from all strengthening mechanisms. It has been found that summing the root of the squares of each contribution shows the best estimation [63]. Total strength contribution is given by Equation (2.3.7)

$$\Delta\sigma = \sqrt{\sum \Delta\sigma_i^2} \tag{2.3.7}$$

where $\Delta\sigma_i$ is each individual contribution.

2.4 Strengthening by ceramic nanoparticles

Introduction of ceramic nanoparticles as grain refiners and hardening phases in aluminium is a promising and remarkable technique to enhance strength. Even a small volume fraction of nanoparticles ($<2\%$) can increase strength without affecting ductility. Too large volume fraction could result in reduction in strength due to agglomeration, clustering and micropores [64]. It is believed that an additional increase of 300 MPa is achievable. The grain refining potential of a certain nanoparticle depends on several factors, such as: (i) edge-to-edge matching, (ii) density and wettability and (iii) the strengthening mechanisms discussed briefly in Section 2,3,

The concept of strengthening, as well as elimination of cracking in aluminium alloys by addition of nanoparticles has already been demonstrated by several researchers. Fattahi *et al.* [63] found retardation of grain growth and increased number of nucleation sites in AA4043, demonstrating enhanced strength and hardness compared to unreinforced aluminium. Sokoluk *et al.* [65] observed improved resistance to cracking in AA7075 after addition of TiC-particles, due to grain refinement and changed grain morphology. The following sections will briefly discuss criterion's for the selection of suitable ceramic nanoparticles.

2.4.1 Edge-to-edge match

The edge-to-edge matching model developed by Zhang *et al.* [66] is used to describe the interfacial crystallographic characteristics between two phases, and has shown valuable in the search for grain refining nanoparticles in Al-based alloys [67]. The main point of looking at edge-to-edge matching is to find the nanoparticles that have the least difference in lattice parameters and thus fit best with the lattice structure of aluminum. The more planes that have low inequality, the more crystal systems can be nucleated by solidification. Zhang *et al.*[66] advocate lattice plane misfit less than 6% and lattice direction misfit less than 10% for heterogeneous nucleation of aluminium from a ceramic nanoparticle. To determine the misfit between particle lattice and aluminium lattice, following data is considered: (i) Crystal structure (BCC, FCC, HCP etc.), (ii) lattice parameters and (iii) close-packed planes and direction.

2.4.2 Heterogeneous nucleation

It is well understood how metals and alloys solidify under heterogeneous nucleation, often with coarse columnar grain structure, unless carefully controlled [68]. Inhomogeneties in the melt solution act as nucleation points, contributing to particle growth and grain formation. The nuclei grows to solid crystals until the phase transformation is complete [68].

A good understanding of the nucleation process is valuable in ensuring that the material achieves the desired properties. Strength in the metal is strongly related to the Hall-Petch relationship, where small grain size is preferred. Small grain size can be promoted by the use of inoculants by increasing the amount of inhomogenities in the melt before heterogeneous nucleation is initiated. When a large number of small grains starts to grow simultaneously, they will eventually be confined by each other, forming a fine grain structure analog to macrograph (b) shown in Figure 2.11 [68].

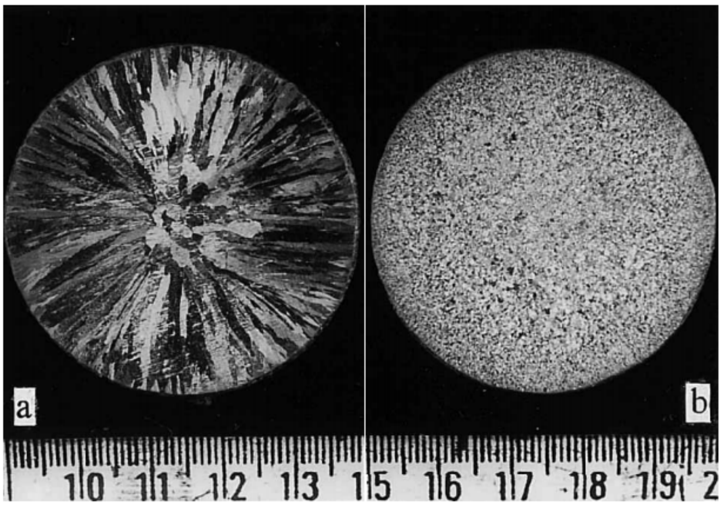

Figure 2.10: Macrograph of (a) commercial pure al without grain refining addition and (b) commercial pure al with 0,2% volume fraction Al – 5 Ti – 1 B master alloy (0´01%Ti) showing coarse columnar grains and fine equiaxed grains. Obtained from [68].

To describe heterogeneous nucleation theoretically, the solidification of the nucleus is described as a spherical cap and is governed by the affinity of the solid solute for the foreign substrate (e.g. metallic, polymeric or ceramic). Both the liquid and the solid phases wet the flat surface, as both phases spread out and cover the surface. The *Spherical-cap* model is typically described in terms of the three-phase contact angle, as illustrated in Figure 2.11 [56].

The three interfacial energies is represented as vectors which describe the two-phase boundaries, σ_{sl}, σ_{cl} and σ_{sc}. The contact angle Θ is defined by the surface tension force balance

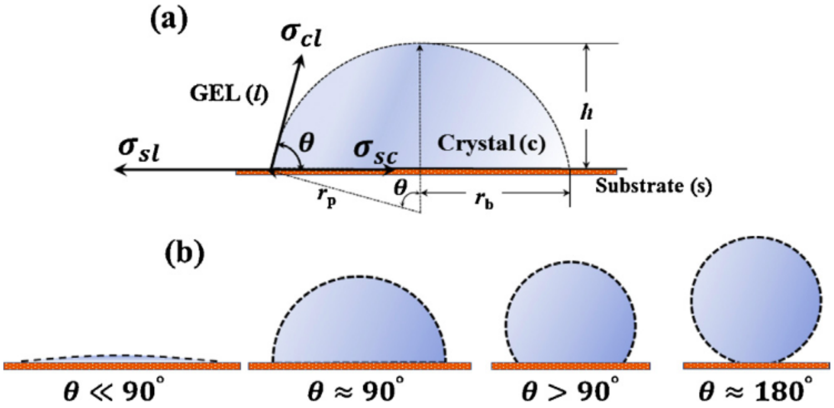

Figure 2.11: Three-phase contact angle for nuclei formation on a flat substrate. (a) Initial spherical cap geometry of nuclei; (b) geometries for different contact angles ($\Theta \ll 90^\circ$, $\Theta = 90^\circ$, $\Theta > 90^\circ$, $\Theta = 180^\circ$). Obtained from [69].

according to Equation (2.4.1)

$$\Theta = \arccos \frac{\sigma_{sl} - \sigma_{cl}}{\sigma_{sc}} \tag{2.4.1}$$

The critical radius, r^* required for a new-phase inclusion to grow is determined by the volume free energy, ΔG_v, according to Equation (2.4.2).

$$r^* = -\frac{2\sigma_{cl}}{\Delta G_v} \tag{2.4.2}$$

As long as the radius of the nucleus is below the critical value, r^*, the nucleus will be unstable and re-dissolve into the melt. The energy barrier for heterogeneous nucleation is given by Equation (2.4.3).

$$\Delta G^*_{het} = \frac{16\pi\sigma^3_{cl}}{3\Delta G^2_v} S(\theta) = \Delta G^*_{hom} \cdot S(\Theta) \tag{2.4.3}$$

It can be observed from the above equation that the energy barrier for heterogeneous nucleation, ΔG^*_{het}, is a function of the homogeneous nucleation,ΔG^*_{hom} and the contact angle, Θ. The energy barrier will therefore always be equal or less for heterogeneous nucleation in a solution or melt. When the contact angle is below 90° the wettability of a solid particle is considered to be high. High wettability prevents agglomeration in the melt [70]. The nucleation rate, $\dot{N}$, is described according to Equation (2.4.4)

$$\dot{N} = C\Big[exp(\frac{-\Delta G^*_{het}}{kT})exp(-\frac{Q_d}{kT})\Big] \tag{2.4.4}$$

where C is a constant for number of atoms on the surface of the nucleus and number of solid nuclei formed, k is the Boltzmann constant, T is the temperature and Q_d is the activation energy for diffusion. It can be observed from the above equation that low contact angle, Θ, decreases the required energy for nucleation. Accordingly, the nucleation rate increases with decreasing contact angle.

When introducing nanoparticles for grain refinement and strengthening purposes it is detrimental if the nanoparticles cluster together, minimizing total surface area. *Sessile drop* tests often performed to determine wetting properties of different phases. Avraham and Kaplan [71] has shown that ceramic particles have instantaneous full wetting with aluminium, gradually reduced with time and increasing temperature. For casting purposes this could be problematic, as the wettability decreases during solidification. For welding in additive manufacturing, the time before solidification is minimal, which should lead to low degree of agglomeration.

2.5 Screw Extrusion

Screw extrusion is a continuous plastic deformation manufacturing process, using an Archimedes screw to manufacture extruded profiles from feedstock material in a one step process. Screw extrusion differs from conventional extrusion, as material is fed as granules, pellets or shavings instead of billets. Screw extruders have different configurations related to how many flights the screw in the extruder has. The most commonly used are single-flight and double-flight, but there are also multiple-flight extruders. It is not uncommon to have multiple screws in the extruder, often widely used in the polymer industry [72]. Extruded profiles are produced by feedstock material being fed into the system at the rear of the screw, where the flights transport the material forward in the screw chamber where it is compacted and pressed through the nozzle in the front of the screw chamber, as illustrated in Figure 2.12 [56].

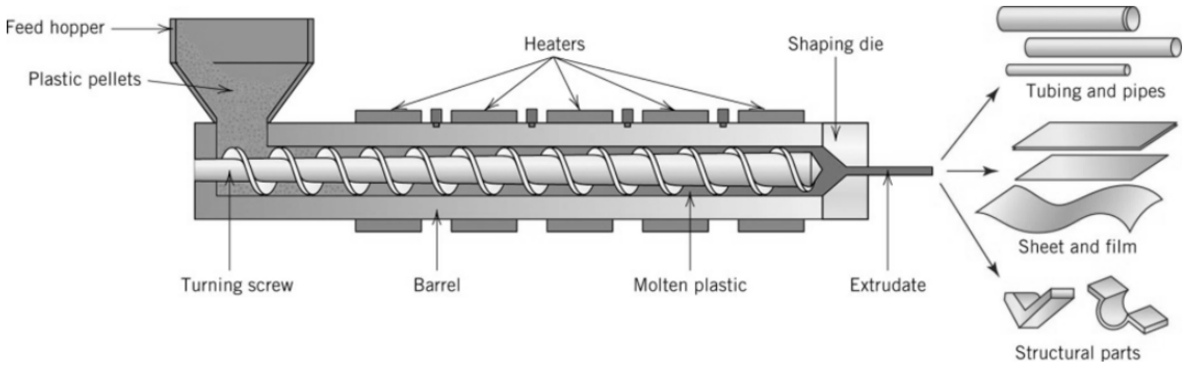

Figure 2.12: Cross-sectional illustration of a industrial polymer screw extruder. Obtained from [56].

2.5.1 Metal Continuous Screw Extrusion

High viscosity extrusion, in particular for metals such as aluminium an its alloys has been described and patented by Werenskiold *et al.* [7]. Metal continuous screw extrusion (MCSE) is a novel solid-state production method for processing of light metal alloys developed at *NTNU - Norwegian University of Science and Technology*, in close collaboration with the Norwegian aluminium producer *Norsk Hydro*. A conceptual illustration of the metal continuous screw extruder is shown in Figure 2.13.

Following assembly of the MCSE, pre-heating of the steel-casing surrounding the screw is performed with an induction coil both before and during extrusion to ensure low viscosity and prevent cracking from thermal stresses. Feedstock material is added to the extruder at the rear end of the screw, as shown by subfigure 3 in the above illustration. Friction between the screw chamber walls and feedstock material pushes the feedstock material forward into the screw channel. As more feedstock material is transported into the screw channel, the extrusion

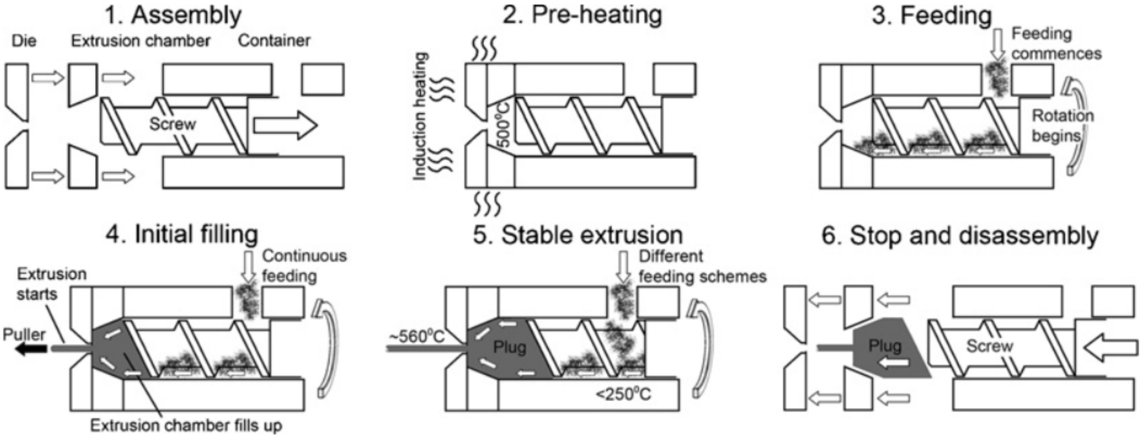

Figure 2.13: Illustration of experimental setup for metal continuous screw extrusion (MCSE). Obtained from [73].

chamber begins to fill up. Pressure in the extrusion chamber will gradually build up as more material is transported in, compacting the material. High temperature and pressure, as well as large strain from the screw will eventually consolidate the material and push it out through the nozzle in the front of the extrusion chamber. The metal will continue to be extruded as long as feedstock material is added to the feed opening in the rear of the screw.

During extrusion, good temperature management is required in order to avoid sticking of metal in the rear screw chamber, as temperatures above 280 °C close to the feed opening are reported to cause sticking and thus excessive load on the screw motor. Internal air cooling is utilized for temperature control, as well as controlling the feed rate of material into the screw chamber. Temperature is monitored by several thermocouple wires embedded in the MCSE during operation.

MCSE has proven promising in terms of aluminum alloy recycling, as liquid recycling involves considerable amounts of energy and metal losses [74]. It is estimated that 41% of all aluminium in the global material stream becomes scrap, never becoming a usable component [75]. Losses depend highly upon forming processes, furnace technology, and melt treatment. Oxidation losses that occur during smelting is non-recoverable, as the desired material properties is lost. Duflou *et al.* [76] assessed environmental impacts associated with ‘melt-less’ scrap recycling and found the screw extrusion route to have the least environmental impact, as shown by Figure 2.14. Mitigation of material losses combined with reduced energy consumption are the major contributors to the significant reduction obtained.

In recent years, a lot of research has been going into MCSE and its potential, including doctoral dissertations by Skorpen [6] and Widerøe [73]. Skorpen has further developed work done by Widerøe and Welo [9] on flow mechanics and accumulated strain during processing [77]. Langelandsvik *et al.* [8] reported promising results indicating that AA1370 aluminium alloy wires manufactured by MCSE outperformed similar alloys when comparing tensile strength and electrical conductivity. MCSE was utilized by Ragnvaldsen [12] for production of an aluminium matrix composite consisting of AA5183 aluminium alloy and titanium carbide nanoparticles (TiC), forming the basis feedstock extrudate for additive manufacturing in this thesis.

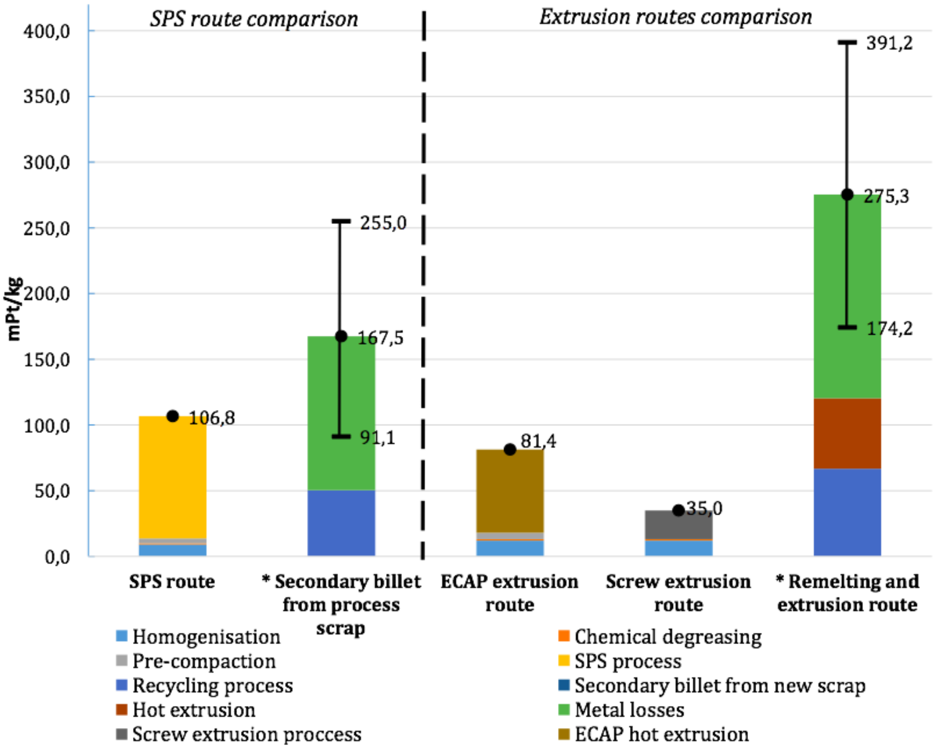

Figure 2.14: Environmental impact of aluminium scrap recycling processes. Environmental impact is measured by the dimensionless energy consumption unit millipoints [mPt] per kg material. Obtained from [76].

2.6 Additive manufacturing

In this section, an outline of additive manufacturing and some available additive manufacturing technologies for metals is given.

American Society for Testing and Materials (ASTM) has defined additive manufacturing (AM) as *"a process of joining materials to make objects from 3D model data, usually layer upon layer, as opposed to subtractive manufacturing methodologies."* In the recent decades, additive manufacturing has seen a rapid development in several industries, especially within aerospace, automotive and marine applications. The technology was previously known as *rapid prototyping* and *layered manufacturing*. The intention is that production of complex components can be manufactured directly from computer-aided design (CAD) files, rather than today's subtractive manufacturing, where raw material is removed layerally until the desired component geometry is produced [78].

The opportunities created by AM are substantial, enabling technological innovations in many industries world-wide. Advantages of AM are numerous. Product designs can be changes without sunk costs in manufacturing. Functionally integrated designs can be produced in one step, such as internal cooling channels for the *Lockheed Martin F-35 Lightning II* fighter jets. AM for components in iterative design processes can be rapidly available at relatively low costs. Another major advantage of AM is the opportunity to produce complex components locally. Local production of critical spare parts are seen as a very promising future of AM, potentially enabling major cost savings for low-volume replacements in industries such as: offshore oil & gas, manufacturing industries and future space exploration [79, 80].

Although AM may feel like earl-stage experimental technology in many cases, AM is extensively used for aerospace applications in present time. *Boeing* reported that 70 000 AM parts are flying through their commercial and defence programs, as the manufacturing industry have become increasingly focused on the so-called *buy-to-fly ratio* (BTF) of components, especially within aviation and aerospace. BTF is the ratio between the weight of initial raw material to be machined and the weight of the finished component. The capability to apply material only where it is needed for structural applications also results in little to no scrap. This is how additive manufacturing can offer a much more favorable buy-to-fly ratio, by using only what is necessary to create the part, as shown in Figure 2.15 Buy-to-fly ratios for machined aircraft components can be as high as 15–20. AM is proposed to reduce the scrap ratio by one order of magnitude, emphasising not only the benefit of cost reductions, but equally important the reduction of supply chain emissions.

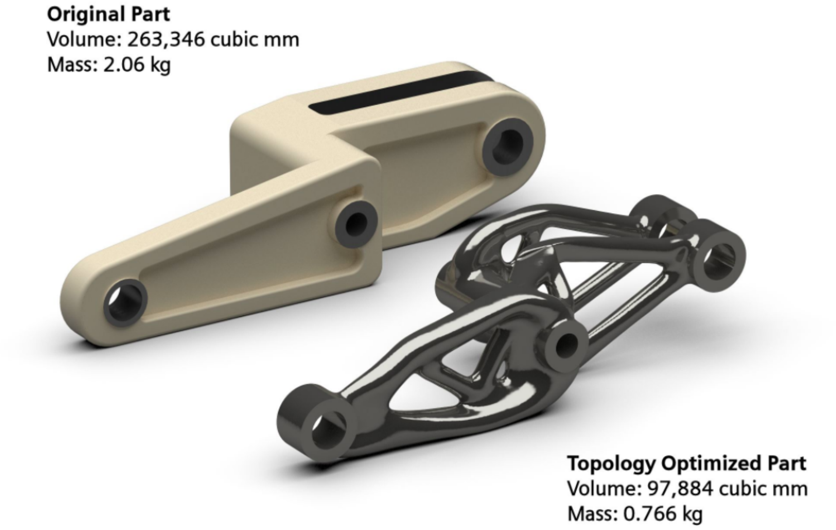

Figure 2.15: Weight and volume savings by topological optimization using additive manufacturing. Obtained from [81].

2.6.1 Additive manufacturing technologies

Several technologies for additive manufacturing have been developed, classified either by the specific technology used, Figure 2.16, or the state of the raw material as shown in Figure 2.17. Powder-based additive manufacturing of metals can be used to fabricate small components with highly complex geometries and dimensional accuracy. In general, the build volumes of these units are less than $30\,\mathrm{dm}^3$, as the build chamber restricts component size. A electron or laser beam delivers high energy to a bed of metal powder, where the energy source successively melt or sinter the powder into preferred shape. Additional powder is supplied by raking more powder over to the powder bed, this process is repeated to create a three dimensional component [14]. The downside of powder-based systems is the low deposition rate, rendering the technology unsuitable for large scale manufacturing.

Powder feed systems for metal additive manufacturing supports not only small component fabrication, but also larger volumes, exceeding 1 m^3. Powder is fed through a nozzle onto the build surface, where a laser melts the powder into desired shape. The build is made by repeating

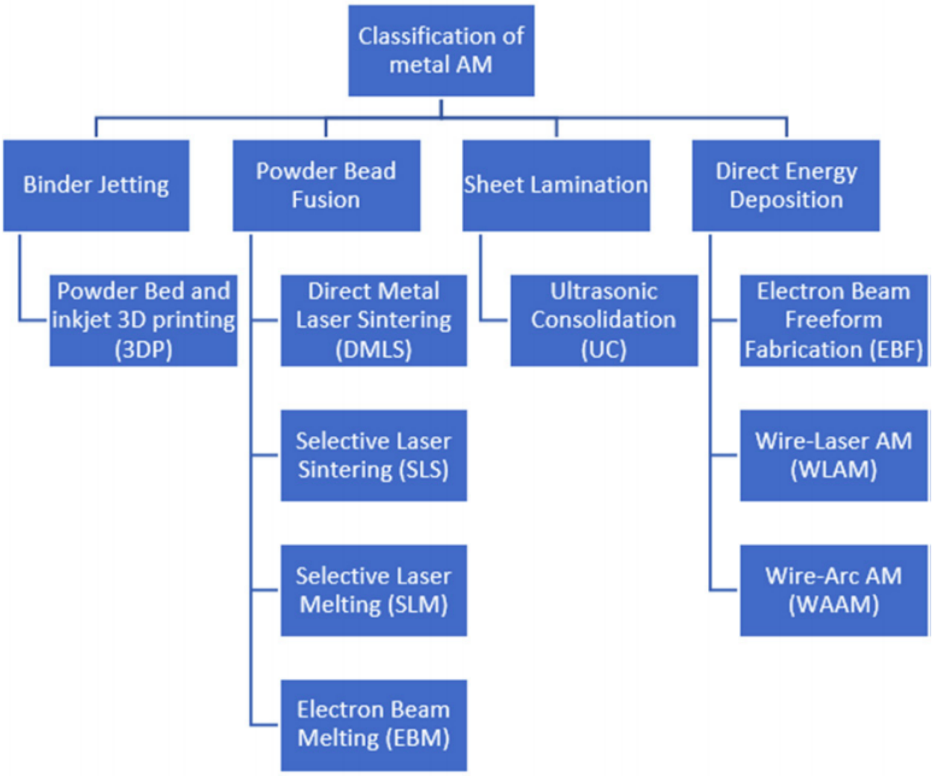

Figure 2.16: Classification of additive manufacturing of metals according to the specific manufacturing technology used. Obtained from [78].

the process, layer-by-layer. The powder feed systems are more suitable for large-scale builds than powder bed systems, with deposition rate in the range 0.1–0.2 kgh^{-1}. One of the major advantages of this system is the ability to refurbish or reconstruct damaged components, making the system particularly useful for maintainance [14].

Wire-based systems also known as *shaped metal deposition* (SMD) has been recognized as the most suitable technology for large-scale production [14]. Several methods for wire-based deposition are utilized, classified depending on the energy source used: electron beam, laser beam and electrical arc. Laser is mainly used for precision-builds, as the energy efficiency is as low as 2–5%. A electron beam requires high vacuum and have higher efficiency (15–20%), suitable for aerospace builds [82, 83]. As this project focuses on WAAM, this technology will be discussed in greater detail in the following section.

2.6.2 Wire and arc additive manufacturing (WAAM)

In wire and arc additive manufacturing (WAAM), a wire is used as the feed material in a direct feed process which uses an electric arc as the heat source and a robot-controlled motion system for deposition. This manufacturing method is recognized as the most efficient way to produce large metal components [84]. The prospects of WAAM are promising within many manufacturing industries, as other AM technologies only supports small-scale production.

Compared with the inferior efficiencies of both laser and electron beams, arc welding can achieve energy efficiency up to 90% [85, 86]. There are several different technologies available for deposition in WAAM, as many have been developed over the years. Most common are the use of either *gas metal arc welding* (GMAW), *gas tungsten arc welding* (GTAW), or *plasma arc*

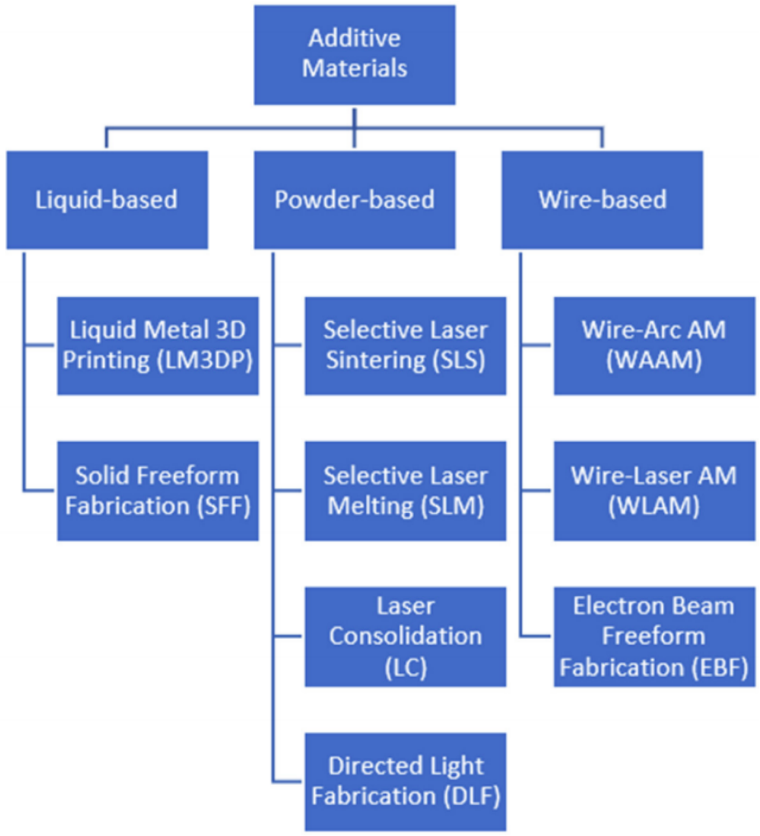

Figure 2.17: Classification of additive manufacturing of metals according to the state of raw materials that is used. Obtained from [78].

welding (PAW) [15]. The three different welding processes are illustrated in Figure 2.20.

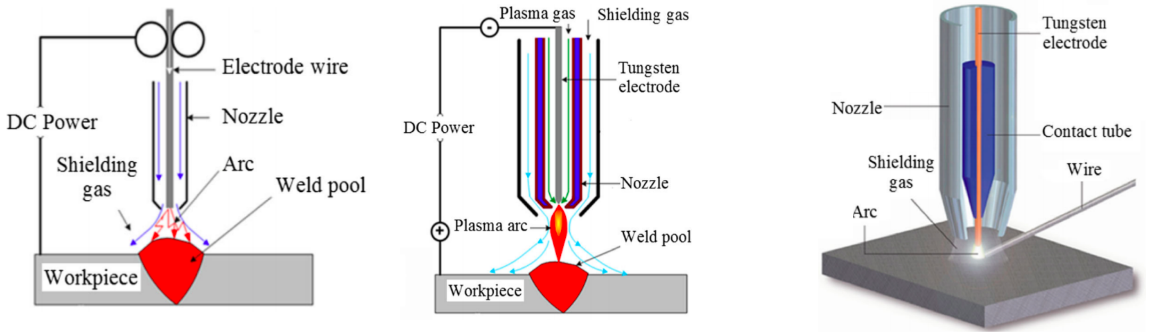

Figure 2.20: Schematic of the three most used welding technologies for WAAM. From the left, GMAW, PAW and GTAW. Obtained and modified [87].

GMAW is used interchangeably with the term *metal inert gas* (MIG) welding to describe the welding process in which an electric arc forms between a metal electrode and the workpiece metal. In GMAW the electrode is consumable, differentiating from GTAW/PAW which uses an inert electrode. GMAW has become the prevailing welding technology, as the welding wire is fed co-axially with the welding torch, simplifying the setup [15].

There are three modes of metal transfer mainly used in GMAW; *globular*, *spray* or *short-circuiting*. Globular metal transfer is characterized by transfer of metal droplets from the feed wire. Detachment of drops happens through either gravity or short-circuiting, resulting in large drops that are hard to control. The method is not much used in AM, because of its tendency to produce high heat, combined with poor weld surface and spatter. Spray metal transfer is done by feeding the electrode wire axially in front of the arc, creating tiny droplets of molten metal. The tiny droplets is then sprayed onto the substrate. This type of metal transfer results in high heat input, large weld pools, no spatter and high quality welds. Short-circuit metal transfer happens through which the metal wire tip is brought in with the substrate metal, a high current is then passed to melt the tip of the wire. A droplet of molten metal forms, and is pulled of the wire to the substrate by surface tension. As soon as the droplet transfer is complete, the arc is ignited again. This process is repeated 20–200 times each second, resulting in deposition of many small droplets of molten metal. This type of metal transfer provides low heat input, good control of deposition, as well as little spatter and good weld quality [88].

Several modifications has been developed to the discussed metal transfer modes [89]. A specialized versions of short-circuiting metal transfer is the *Cold Metal Transfer* (CMT) method, discussed in the following section.

2.6.3 Cold Metal Transfer (CMT)

As an extension of GMAW, the Austrian company *Fronius* developed a new welding process called *cold metal transfer* (CMT) [89]. CMT differentiates to conventional short-circuiting GMAW in how the molten metal droplets are cut from the feed wire. The CMT mode does not pass a high short-circuiting current through the feed metal wire tip. Instead, when the molten metal droplet touches the substrate, the feed wire is quickly retracted by a built-in motor, such that the droplet is cut without adding heat through current. The forward and backward movement can have a frequency up to 150 Hz during welding. The current drops to near-zero, before re-igniting the arc for deposition of next droplet [89]. The transition of current during the CMT process is illustrated in Figure 2.21.

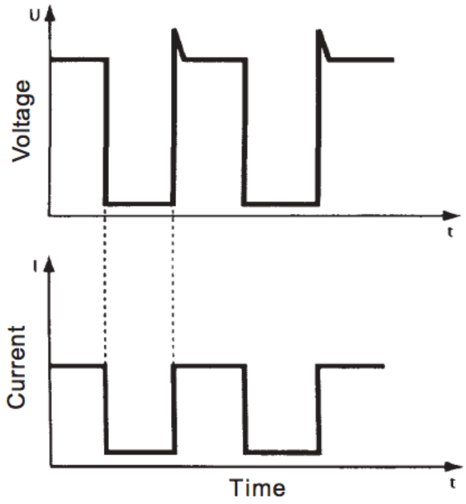

Figure 2.21: Transition of current and voltage during cold metal transfer (CMT). Current and voltage drops to nearly zero during short-circuit droplet detachment. Obtained from [90].

The main reason making CMT highly favourable for WAAM is the reduced heat input. Combined with other advantages as small deformation, high welding speed and low operation cost, the WAAM-CMT technology has shown to be very suitable for low melting point metals, such as aluminium alloys [91].

2.7 Additive manufacturing of aluminum alloys

In this section, behaviour and characteristics of aluminium alloys relevant for additive manufacturing will be discussed

Since CMT is a relatively new technology, there are limited studies focusing CMT welding of aluminum alloys. Of special interest is the 5xxx aluminum alloys, as they are used extensively in the shipbuilding industry, due to their high corrosion resistance and moderate strength. Ding et al. [87] has pointed out several challenges for components manufactured by WAAM: (i) residual stresses and distortions from welding heat input, (ii) unsatisfactory surface finish and (iii) necessity of careful process parameter tuning. Cong et al. [92] showed that one of the major challenges for WAAM components of Al-6Cu is porosity. Porosity was found by Cong et al. [93] to change depending on several factors, such as: (i) process arc mode, (ii) cleaning of wire, support plate, shielding gas cleanliness and (iii) cracking from re-heating of previous deposition layer.

Factors affecting properties of WAAM aluminium alloys will be discussed in detail in the following sections to provide a sufficient understanding.

2.7.1 Solidification of aluminium alloys

Solidification of aluminium alloys proceeds through a series of mechanisms, which can be used to control properties [94]. This section will give a brief discussion of solidification mechanisms. Aluminium solidification differentiates from most ferrous alloys in that there are no phase solid-state transformations during solidification, which means that the microstructure is solely dependent on the solidification course [27]. This sections will give a brief discussion of solidification mechanisms.

Two key parameters that influences the solidification microstructure are the growth rate (R) and the temperature gradient (G). In addition extensive research in the past has shown that various processing parameters, such as cooling rate, solidification rate, and temperature gradient across the solid/liquid interface (undercooling, ΔT) heavily affects the resulting microstructure in aluminium alloys. In both wrought and cast alloys, the preferred microstructure arrangement for engineering applications is uniform fine equiaxed grains, which yield isotropic mechanical properties [94].

Solidification of weld metal take place in a bounded region called the *mushy zone* (solid/liquid interface), which trails the moving weld pool, bounded by the dashed vertical lines in Figure 2.22. The right vertical line from the figure is equivalent to the liquidus temperature, while the left vertical line is defined as the lowest melting eutectic temperature. Generally, solidification in the mushy zone always starts with a single nuclei forming in the melt. The nuclei grows into spherical crystals, which at some point becomes unstable and forms a dendritic structure. Dendrites will continue to grow freely in the melt and impinge other dendrites. The positions of impingement are what becomes the grain boundaries in the microstructure. In most alloys, dendrites will remain visible after solidification due to microsegregation, that is - interdendritic composition differences [94]. For a more detailed description of the general nucleation process, topics such as *heterogeneous nucleation* and the *spherical cap model* should be reviewed.

Morphology of the solidifying grains depends upon the extent of undercooling. Small undercooling (ΔT) promotes cellular grains, whereas large undercooling promotes equiaxed dendritic grains. Figure 2.22 shows how nucleation of equiaxed grains occurs within the mushy zone. The heat flow is fundamental to grain growth, and is classified as either *constrained* or *unconstrained*. In constrained growth, the heat flow is opposite to the grain growth direction. Columnar solidification is constrained, that is - the rate of which isotherms advances in the melt constrains the growth at a specific velocity. In unconstrained equiaxed grain growth, the heat flows from the crystal into the melt, resulting in radial growth, until they impinge upon other dendrites [94].

Wrought alloys with low solute contents has been extensively researched to gain a thorough understating of the *columnar-to-equiaxed transition* (CET) [95, 96, 97]. As sketched in Figure 2.22, the equiaxed region is growing in the liquid in front of the columnar region. According to heterogeneous nucleation theory, the initial nuclei can only survive if the liquid is super-cooled. The solid/liquid interface of the columnar grains contribute to supercooling by *partitioning*, that is - altering the liquid composition at the columnar front, and thus lowering the local liquidus temperature. It is the temperature gradient which determines how far the supercooled region extends from the columnar front [98].

Considering an Al-Mg 5xxx-series alloy, from the phase diagram it can be seen from the phase diagram in Figure 2.3 that Al-Mg (4.5% Mg) solidifies into the α-area as dendrites containing approximately 2% Mg. A concentration gradient forms, as magnesium diffuses from the dendrite into the liquid. The diffusion layer that forms locally in front of the dendrites, causes a undercooling as the liquidus temperature is lowered in this region.

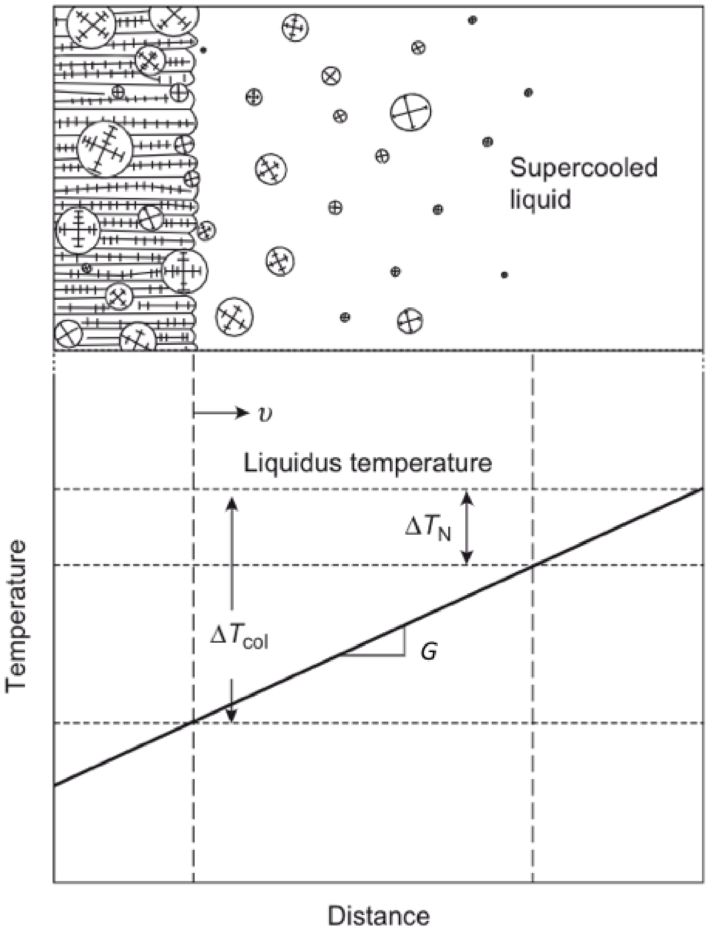

Figure 2.22: A schematic view of solidification. The mushy zone is bound by the two dashed vertical lines, showing a columnar-to-equiaxed transition. The columnar solid/liquid interface moves with velocity, v, with a temperature gradient G throughout the solidifying region. ΔT_N is the supercooling for heterogeneous nucleation on substrates in the liquid, while ΔT_{col} is the supercooling (relative to the liquidus of the bulk liquid) for advance of the columnar front. Obtained from [99]

A simple description of the solidification process is given by the *Scheil model*, which predicts solute concentration as a function of the solid fraction according to Equation (2.7.1).

$$C_s^* = kC_0(1 - f_s)^{(k-1)} \tag{2.7.1}$$

where C_s^* is the solute concentration enclosing a weight fraction of solid f_s, C_o is the initial average composition, and k is the equilibrium solute redistribution coefficient derived from the phase diagram of the alloy. The redistribution coefficient varies for different alloying elements. For alloying elements having a small coefficient, large solute segregation occurs during solidification (e.g. Cu, k = 0.17). For elements exhibiting larger coefficients, solute segregation decreases (e.g. Mg, k = 0.51) [100].

During solidification, primary equilibrium phase is first formed, at a different composition from the bulk liquid. The liquidius temperature will then change, due to solute enrichment in the liquid close to the solidifying interface. Unstable conditions arise at the interface, resulting in breakdown of the interface between solid and liquid. Solidification behaviour of two different aluminium alloys are illustrated in Figure 2.23, showing how large temperature range during solidification traps eutectic liquid in-between the solidified dendritic structure. Volumetric shrinkage and thermal contraction can induce hot tearing due to the poor structural stability [101].

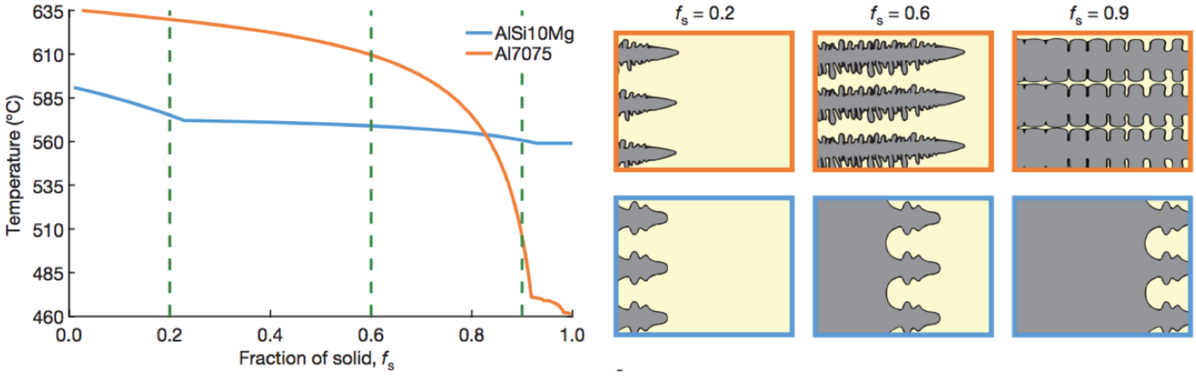

Figure 2.23: Left: Solidification curves for Al7075 (orange) and $AlSi_{10}Mg$ (blue). Right: Schematic representation of solidification at three different solid fractions, indicating how solidification over a large temperature range leads to channels of interdendritic fluid (orange). A narrow temperature range indicates that channels are filled, and solidified (blue). Obtained from [101].

In additive manufacturing, a moving pool of molten metal leaves behind a very unique solidification pattern depending on the temperature gradients near the solidifying metal [102]. Moving heat sources such as an electric arc strongly influences material properties, as a fusion zone, a heat affected zone and microstructural gradients are created. Figure 2.24 illustrates how the columnar grains grows epitaxially along the largest temperature gradient during welding.

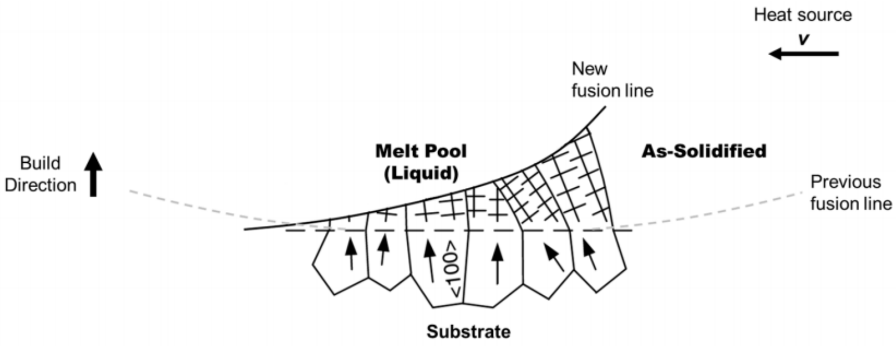

Figure 2.24: Illustration of epitaxial grain growth during welding. Molten metal solidifies as the heat source moves away. The arrows show easiest growth direction of grains. Obtained from [103].

Wei et al. [104] found that a scanning speed of 2.0 mm/s during welding produced only columnar grains, whereas a transition from curved columnar to equiaxed morphologies occurred at the higher scanning speeds of 8.0 mm/s and 11.5 mm/s, with higher equiaxed grain fraction at higher speed. Schempp et al. [105] demonstrated that increasing alloy content allow growth of small, equiaxed grains, particularly in the weld center.

2.7.2 Porosity in additive manufactured aluminium components

The amount of porosity in additive manufactured aluminium components has been one of the major obstacles hindering large-scale commercialization [106, 107, 108]. Micropores are detrimental to the mechanical properties, as they create strain concentration, resulting in lower load-bearing capacity and higher susceptibility to fracture. Fatigue, strength and toughness is negatively affected by increased pore density [109]. Mayer et al. [110] has shown that micropores larger than $50\,\mu\mathrm{m}$ functions as propagation sites for cracking. A thorough understanding of pore formation is essential to mitigate growth, and increase the density of aluminum in additive manufactured components.

Talbot [111] reported that hydrogen dissolved in liquid phase remains in the FCC structure during casting, as a solid solution. As the aluminium alloy solidifies, the equilibrium hydrogen partial pressure increases, leading to the heterogeneous nucleation of hydrogen porosities. Every alloying element used to tailor properties in aluminium alloys, will also affect the hydrogen solubility. Fe, Cu and Si are reported to decrease the solubility of hydrogen in the liquid, whereas Mg and Li are reported increase the solubility [112]. Boeira [113] reported the equilibrium solubility of hydrogen as $0.650\,\mathrm{mL}$ per $100\,\mathrm{g}$ in molten pure aluminium and $0.034\,\mathrm{mL}$ per $100\,\mathrm{g}$ in solid pure aluminium. The hydrogen solubility is approximately 20 times larger in molten aluminium, than in solid aluminium. Hydrogen is thus segregated as gas pores during solidification. By contrast, steel have the same hydrogen solubility both in liquid and solid phase [109].

The average radius r_{ave} of a pore increases with time, t, according to Equation (2.7.2),

$$r_{ave}^3 - r_0^3 = kt \tag{2.7.2}$$

where r_0 is the mean radius at t = 0, k is the growth coefficient proportional to the diffusion coefficient D and total interfacial free energy, γ. The diffusion coefficient is determined from the Arrhenius equation, defined by Equation (2.7.3),

$$D = D_0 e^{\dfrac{-E_A}{RT}} \tag{2.7.3}$$

where is D_0 a pre-exponential factor, E_A the activation energy, R the gas constant and T the temperature [114]. The diffusion constant increases exponentially with temperature, meaning that pore radius also increases with temperature. A prominent growth mechanism is therefore *Oswald ripening* - growth of large pores at the expense of small pores, as hydrogen diffuses away from smaller pores [107].

Pore formation in an as-deposited WAAM build is found due to several different mechanisms. Individual micropores are formed due to precipitation of supersaturated hydrogen, which nucleates at grain boundaries, second phases and inclusions in the alloy. Chain-like cavities forms due to solidification shrinkage or the lack off channel-filling between dendrites, as described and visualized in Figure 2.23 [107]. The feedstock wire and substrate is susceptible to surface contamination, such as grease, moisture and other hydrocarbons. If contaminants are absorbed into the melt pool, susceptibility to porosity increases. Good cleaning procedures for both feedstock wire and substrate is essential to mitigate porosity in the build.

Oliveira et al. [115] reported that pore formation in aluminium alloys has close relationship with welding parameters during additive manufacturing, as well as dendrite growth and grain morphology. Cong et al. [92] found that lowering of heat input results in less porosity, by using advanced pulse CMT. Gu *et al.* [116] eliminated micropores by inter-layer rolling, achieving 99.9% density of WAAM aluminium.

Chapter 3

Experimental

This section will give a description of raw materials, equipment and methods used in the present work. A flow chart illustrating the experimental procedure is given in Figure 3.1.

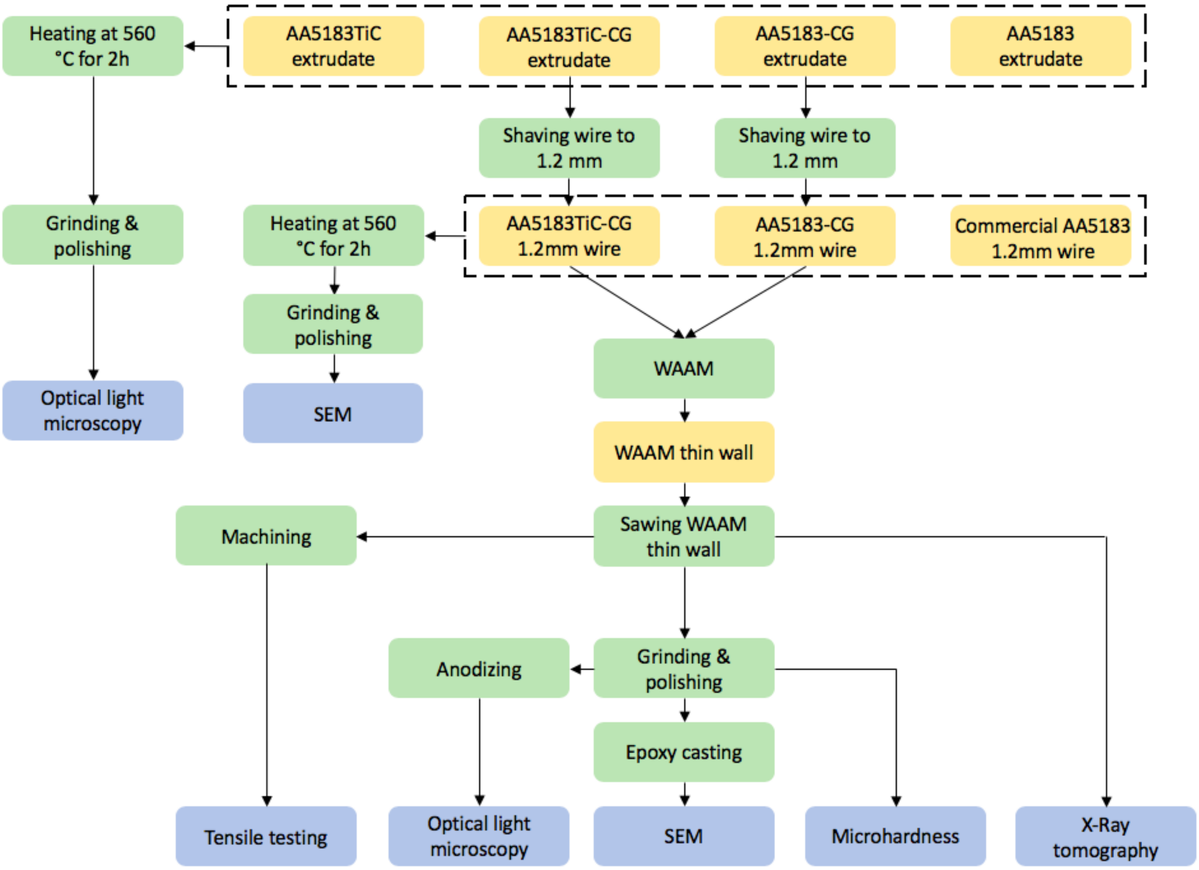

Figure 3.1: Preparation of extrudate for WAAM from preliminary work by Ragnvaldsen [12]. Wire arc additive manufacturing (WAAM) using shaved feedstock wires, then sample preparations for post-production characterizations and testing.

3.1 Extrudate material

The material supplied for this present work was extruded using metal continuous screw extrusion (MCSE) in preliminary work by Ragnvaldsen [12]. The feedstock used for MCSE was a commercial AA5183 aluminium alloy delivered as welding wire by *Safra*. Elemental analysis of the as-provided AA5813 wire is shown in Table 3.1.

Table 3.1: Elemental composition of aluminium alloy AA5183 welding wire provided by *Safra*. Analysis done by optical emission spark analysis [12].

Element	Content [wt%]
Al	Balance
Mg	4.65
Fe	0.12
Ti	0.11
Cu	0.01
Mn	0.66
Si	0.15
Zn	0.01
Cr	0.09

The titanium carbide (TiC) nanoparticles for coating of the AA5183 wire was supplied by *US Research Nanomaterials Inc.* and had an average particle diameter of $50\,\mathrm{nm}$. Before TiC coating, both wires were reported thoroughly cleansed thermally and chemically. Both wires were extruded using a double flight screw setup and CO_2 cover gas (CG). Processing temperatures during extrusion was held stable using a copper induction coil ranging between 2-6 kWh. Temperatures during extrusion of AA5183TiC-CG and AA5183-CG is shown in Figure 3.2 and Figure 3.3, respectively.

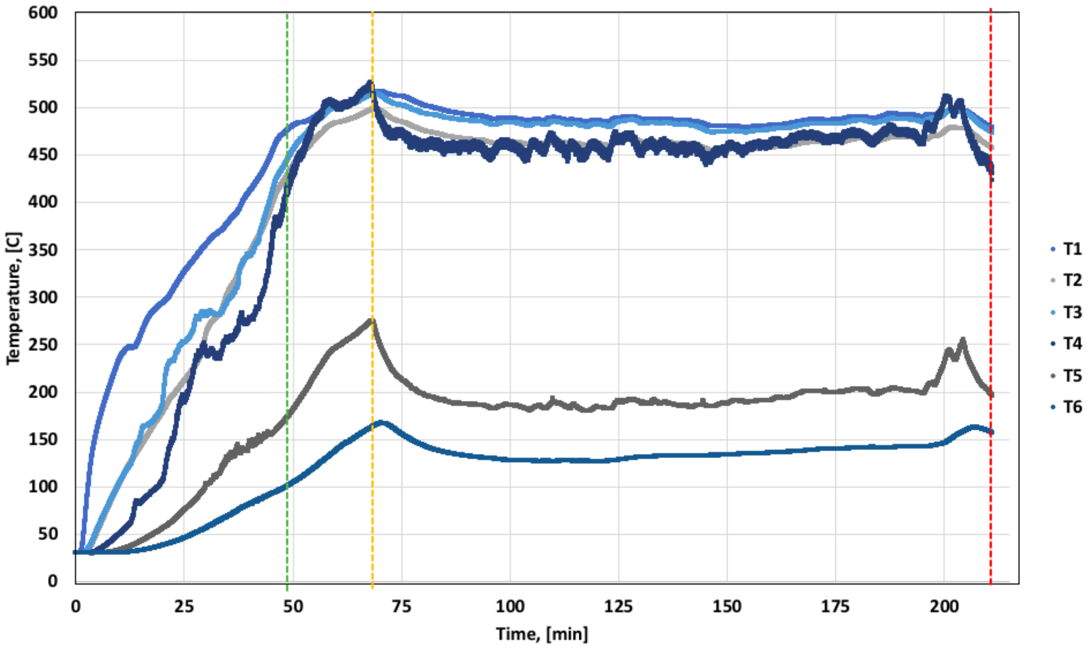

Figure 3.2: Temperature through screw extrusion of AA5183TiC-CG with CO_2 cover gas. Dashed green line indicates extrusion start, orange dashed line indicates air-cooling start and red dashed line indicates screw extrusion stop. Position of temperature measurements are: T1 (die), T2/T3 (left/right side extrusion chamber), T4 (front screw channel), T5 (back screw channel) and T6 (screw stem). Temperature data was collected by Ragnvaldsen [12] in his preliminary work on processing of AA5183TiC-CG.

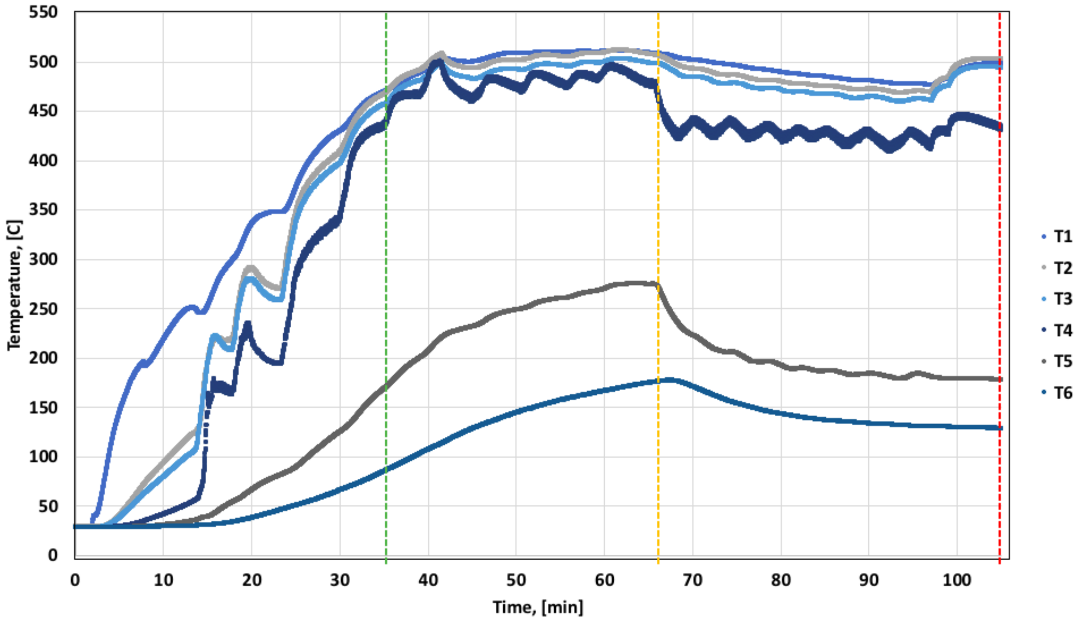

Figure 3.3: Temperature through screw extrusion of AA5183-CG with CO_2 cover gas. Dashed green line indicates extrusion start, orange dashed line indicates air-cooling start and red dashed line indicates screw extrusion stop. Position of temperature measurements are: T1 (die), T2/T3 (left/right side extrusion chamber), T4 (front screw channel), T5 (back screw channel) and T6 (screw stem). Temperature data was collected by Ragnvaldsen [12] in his preliminary work on processing of AA5183-CG.

3.2 Drawing and shaving of extrudate

The as-extruded wires had a diameter of 10 mm and had to be drawn and shaved down to a diameter of 1.2 mm in order to be used for wire arc additive manufacturing (WAAM).

The extruded AA5183TiC-CG and AA5183-CG wires were sent for drawing and shaving at *Technische Universität Bergakademie Freiberg* in Germany. Firstly, the extrudates were rolled to a thickness of 6.7 mm through 8 passes at a temperature of 400 °C. Secondly, the wires were drawn in seventeen separate steps with a 15 min 350 °C heat treatment both before and in between each step until a diameter of 1.6 mm was acquired. Lastly, the drawn wire was shaved in three separate steps to a wire diameter of 1.2 mm, providing a smooth surface finish without cracks and scratches that may contribute to porosity during WAAM.

3.3 Heat treatment of extrudate and welding wire

Four different as-extruded 10 mm profiles were subject to heat treatment in a *Nabertherm N17/HR* at 560 °C for 2h in inert argon atmosphere. AA5183 and AA5183TiC screw extruded without using CO_2 cover gas, as well as AA5183-CG and AA5183TiC-CG screw extruded with CO_2 cover gas. Figure 3.4 shows the different extrudates.

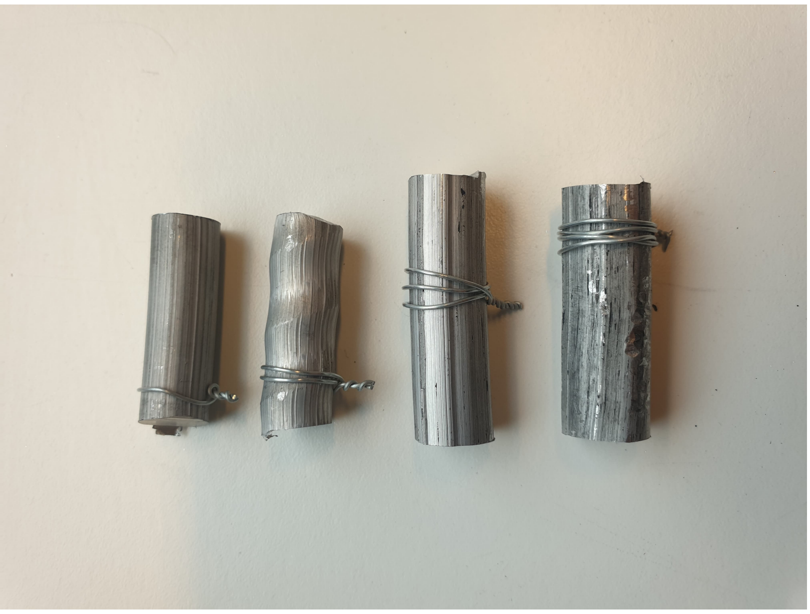

Figure 3.4: From left the first sample is AA5183-CG, second sample AA5183, third sample AA5183TiC-CG and fourth sample AA5183TiC. The steel wires were used to indicate sample number. Extrudates produced by Ragnvaldsen [12].

After heat treatment, each extrudate profile sample was subject to cross-sectional sawing, then a polishing procedure as outlined in Table 3.3. Samples were imaged with a *Samsung S9* for assessment of heat treatment.

In addition, 1.2 mm drawn an shaved extrudate wires were subject to the same exact heat treatment procedure as the as-extruded profiles above. These were AA5183-CG and AA5183TiC-CG wires, as well as a commercially supplied AA5183 welding wire from *Safra*. The heat treated wires were cast in *Epofix* epoxy-resin. Air was removed using a *Struers Citovac* vacuum chamber before resin was set to harden overnight. Corresponding non-heat treated wires were also cast for later comparison. Samples were imaged in a scanning electron microscope according to details given in Section 3.5.1

3.4 Wire arc additive manufacturing

Additive manufacturing of an aluminium alloy WAAM thin wall was done, using an *ABB LRC* power source developed by *Fronius* in CMT-mode. 99.9% argon was used as shielding gas during WAAM deposition. A *ABB IRB2400* robotic arm programmed by the software *RobotStudio* was utilized for WAAM, and is shown in Figure 3.5. Feedstock wire were $1.2\,\mathrm{mm}$ diameter AA5183-CG and AA5183TiC-CG. A cleaned and polished AA6082 plate was used as a base plate for the deposition of the WAAM WAAM thin wall.

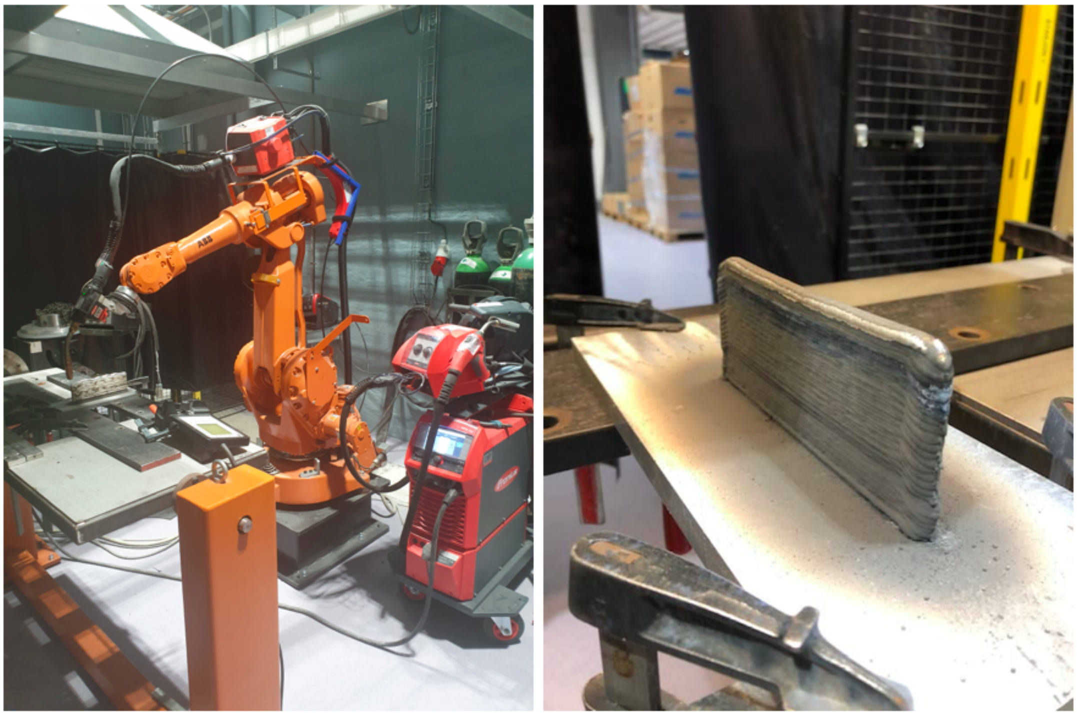

Figure 3.5: Experimental setup of *ABB IRB2400* robotic arm for WAAM to the left, and as-manufactured WAAM thin wall to the right.

The welding parameters for the WAAM-build is given in Table 3.2. The first layer was deposited using MIG-Pulse mode to ensure sufficient adhesion of the first layer to the AA6082 supporting plate. The succeeding layers were deposited using CMT-mode. The wall was built by alternating deposition direction, to ensure good geometric accuracy. A wait time of 180 seconds between each layer was utilized to provide heat dissipation to the base plate. The AA5183-CG wire was used for the first third of the WAAM thin wall, and AA5183TiC-CG wire for the remainder.

3.5 Sample preparation

The as-built WAAM thin wall was subjected testing and characterization, in order to assess properties of the manufactured component. A detailed description of each sample preparation

Table 3.2: Welding parameters for WAAM of AA5183-CG and AA5183TiC-CG, utilizing ABB LRC power source.

Parameters	**AA5183**				
Layer	1	2	3-4	5	6-end
Weld method, [-]	MIG-P	CMT	CMT	CMT	CMT
Current, [A]	190	135	95	90	85
Step height, [mm]	2.2	2.2	2.2	2.2	2.2
Wait time, [s]	180	180	160	180	180
Voltage, [V]	22.3	15	13.1	12.3	11.9
Travel speed, [mm/s]	8	8	8	8	8
Wire feed speed, [m/min]	11.2	9.0	7.6	6.2	5.8
Thermal efficiency coefficient, [-]	0.8	0.8	0.8	0.8	0.8
Heat input, [J/mm]	424	203	124	111	101

process is given in the following subsections.

Samples for testing and characterization were prepared according to marked sections shown in Figure 3.6. In addition, sample preparation of the heat treated AA5183-CG and AA5183TiC-CG wires, as well as a commercially supplied AA5183 welding wire from *Safra* was carried out. Non-heat treated corresponding parallels was also prepared.

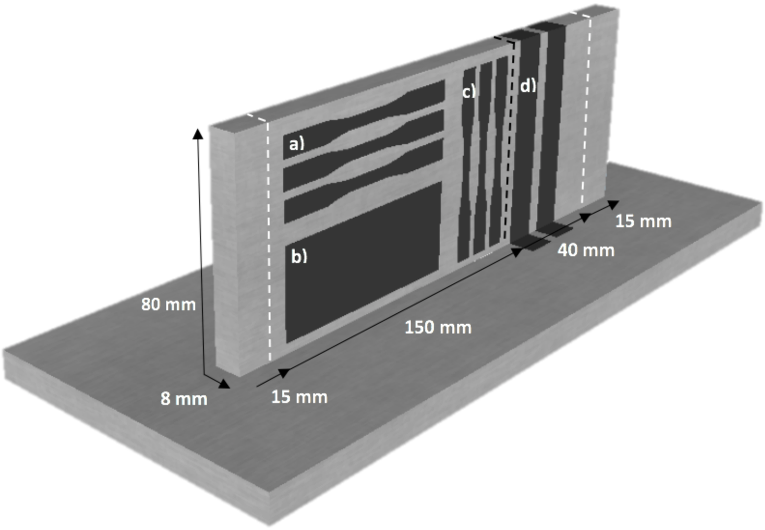

Figure 3.6: Illustration of correpsonding sample sections of WAAM thin wall. (a) Tensile specimen (x), (b) metallography, (c) tensile specimen (y), (d) microhardness, microCT and metallographic specimen.

3.5.1 Microscopy images

For observation of microstructure in both optical light microscopy and scanning electron microscopy, all samples underwent the step-wise polishing procedure tabulated in Table 3.3.

Table 3.3: Step-wise polishing procedure. Samples were examined in microscope between each step to ensure sufficient grinding or polishing before performing the next step.

Step	Surface	Suspension/Lubricant
1	SiC FEPA #320	Water
2	SiC FEPA #800	Water
3	MD-mol 6 µm	Diapro Mol
4	MD-mol 3 µm	Diapro Mol
5	MD-NAP 1 µm	NAP-B
6	MD-Chem	OP-S NonDry

The polishing was done manually by hand for the first two steps, using *TegraPol-31*. The remaining steps were carried out using a *Struers* combined polisher (*TegraPol-31*) and load supplier (*TegraForce-5*), until the surface of each sample had no visible scratches. The WAAM thin wall samples were anodized to enhance the visibility of the microstructure. *Barkers reagent* was used as the electrolyte solution, consisting of 400 mL distilled water and 10 mL fluoroboric acid (48 wt% HBF_4). A voltage of 20 V was applied for 90 seconds to produce the anodizing oxide film on the sample surface. Samples were immediately rinsed in tap water and ethanol after anodizing.

For characterization of the anodized microstructure, images were taken using a *Zeiss AXIO* inverted microscope with polarized light and a sub-lambda plate inserted in the column. Pictures were collected and analyzed using the software Zen Core. To reveal the microstructure of large wall sections in one image, stitching was done using the open-source image processing tool *Fiji ImageJ* [117, 118].

Characterization in scanning electron microscopy required electrical conductivity from the metallic sample surface to the backside of the epoxy specimen, in order to avoid electrons contributing to charging effects during imaging. Aluminium foil was used to ensure sufficient electrical contact with the backside of the sample. Before imaging, samples were kept overnight in a heating cabinet at 65 °C for degassing.

Images were taken using a *Zeiss Supra 55-VP* low vacuum field emission scanning electron microscope. Samples were analysed for elemental composition using an equipped instrument for dispersive X-ray spectroscopy (EDS), combined with an *EDAX EDS* unit and *EDAX Team software*

3.5.2 Micro X-Ray computational tomography

For characterization of porosity in the WAAM thin wall, micro X-ray computational tomography (micro-CT) was performed on a section of the wall, indicated by Figure 3.6. Mapping of porosity in the sample specimen was performed using a *Nikon XT H225ST NC Scanner*, yielding a true three dimensional mapping of the internal pore structure of the sample.

Scanning was performed at a voltage of 135 kV, and 195 uA applied current. 900 scan slices was aquired through scanning, which was stacked and post-processed using the open-source image processing tool *Fiji ImageJ* [117, 118]. Pore distribution data was post-processed using *MATLAB*.

3.5.3 Tensile testing

Samples for tensile testing was machined by *SINTEF Mechanical Workshop*, from two different orientations in the WAAM thin wall. Three tensile specimens from the longitudinal direction, and three tensile specimens from the transversal direction, as indicated by the illustration in Figure 3.6. The dimensions of all tensile specimens were the same, and are given in Figure 3.7. The machined tensile specimens is shown in Figure 3.8, according to the corresponding direction in the WAAM thin wall. Tension tests of the six samples were performed in a hydraulic *MTS 810* universal testing machine at a constant strain rate of $2\,\mathrm{mm\,min^{-1}}$ (corresponding to $30\,\mathrm{\mu m\,s^{-1}}$). A 25 mm extensiometer was used. Data was collected using the software *MTS Testworks*. The acquired tensile data was post-processed using *MATLAB*.

3.5.4 Microhardness

Vickers microhardness $(HV_{0.1})$ was measured on a cross-sectional wall sample using *Leica VHMOT* for hardness measurements. The WAAM thin wall sample was polished following the procedure outlined in Table 3.3, to ensure an even and smooth surface.

Measurements was performed on the front section of the WAAM thin wall, corresponding to section b) in Figure 3.6. A force of $100\,\mathrm{g}$ and a dwell time of 10 seconds was used for measurements. Distance between each indent were $350\,\mathrm{\mu m}$, ensuring that measurements were not affected by previous indents in accordance to the *ISO6507-1:2018* standard. 15 indentations were performed on the sample surface. The acquired microhardness data was post-processed using *MATLAB*.

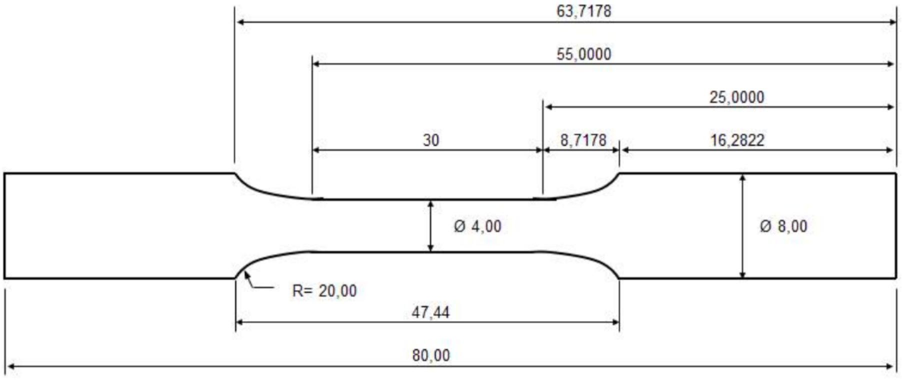

Figure 3.7: Dimensions used for machining of tensile specimens used for tensile tests.

Figure 3.8: Tensile specimens machined according to dimensions in Figure 3.7. Tensile specimens to the left corresponds to the longitudinal samples (a), and the tensile specimens to the right corresponds to (c) shown in shown in Figure 3.6.

3.6 Additional work on AA6082 aluminum alloy

A flow chart illustrating additional experimental work on AA6082 is given in Figure 7.1. A more detailed description will be given in section A in appendices.

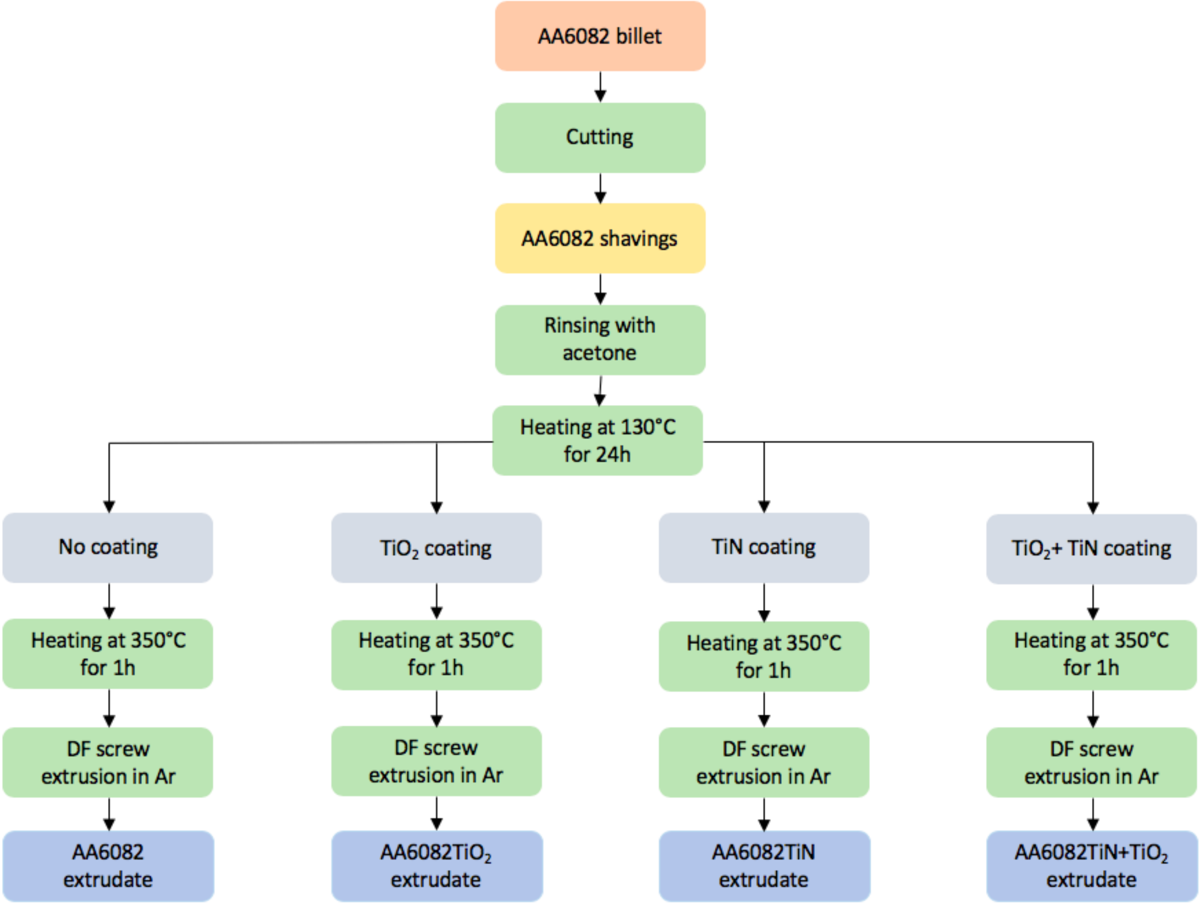

Figure 3.9: Flow chart illustrating experimental work on nanoparticle introduction in AA6082 aluminium alloys.

Chapter 4

Results

This section will give a description of the results obtained from wire arc additive manufacturing (WAAM) of AA5183TiC-CG and AA5183-CG aluminium alloys. Results obtained from additional work on AA6082 aluminium matrix composites may be found in section A in Appendices .

4.1 Heat-treatment of feedstock material

In this section, investigation of feedstock material for WAAM will be presented. Specifically, MCSE extrudate 10 mm profiles and welding wire investigations.

4.1.1 MCSE extrudate 10 mm profiles

Figure 4.1: Image shows transversal and longitudinal cross-sections of metal continuous screw extruded (MCSE) 10 mm extrudate profiles. The extrudates were held at 560 °C for 2h in inert argon atmosphere. Leftmost, AA5183-CG, then AA5183, AA5183TiC-CG and AA5183TIC. Profiles extruded using CO_2 cover gas are labeled ”CG”. The samples are approximately 1-2 cm in length.

Results from heat treatment of AA5183-CG, AA5183, AA5183TIC-CG and AA5183TIC as-extruded MCSE 10 mm profiles at 560 °C for 2h in inert argon atmosphere are shown in Figure 4.1. For comparison with pre-heat-treatment extrudate 10 mm profiles, the reader is encouraged to visit preliminary work by Ragnvaldsen [12].

From Figure 4.1 the AA5183-CG and AA5183 extrudates appears to exhibit the worst condition post-heat-treatment, as visible by severe cracking in both the longitudinal and transverse direction. Seen from the transversal cross-section, cracking is observed to be circular. AA5183TiC-CG showed no signs of cracking, while AA5183TIC shows some minor cracking close to the extrudate surface. It may be noted that both AA5183-CG and AA5183 extrudate samples were taken from the initial extrudate during extrusion, whereas AA5183TiC-CG and AA5183TiC samples were taken from mid-process extrudate, which may have been more stable in terms of processing condition. Comparison of MCSE extrudate profiles indicate a significant reduction in cracking due to the introduction of cover gas during processing.

4.1.2 Welding wire 1.2 mm

Scanning electron microscopy images of non-heat-treated and heat-treated 1.2 mm drawn and shaved AA5183TiC-CG wires are presented in this section. Commercially supplied AA5183 welding wire and AA5183-CG welding wire are included in section C in the appendices.

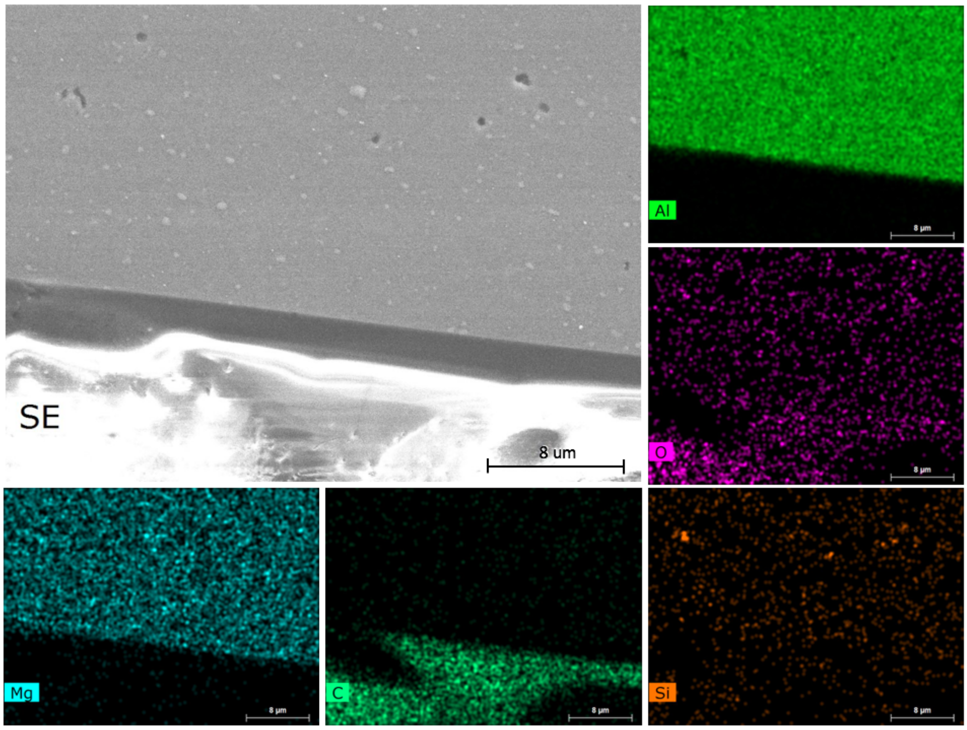

Figure 4.2: Scanning electron microscopy by secondary electron imaging of non-heat-treated AA5183TiC-CG welding wire. The white noise in the images is due to charging effects in the SEM. Elemental EDS mapping is shown in colored images.

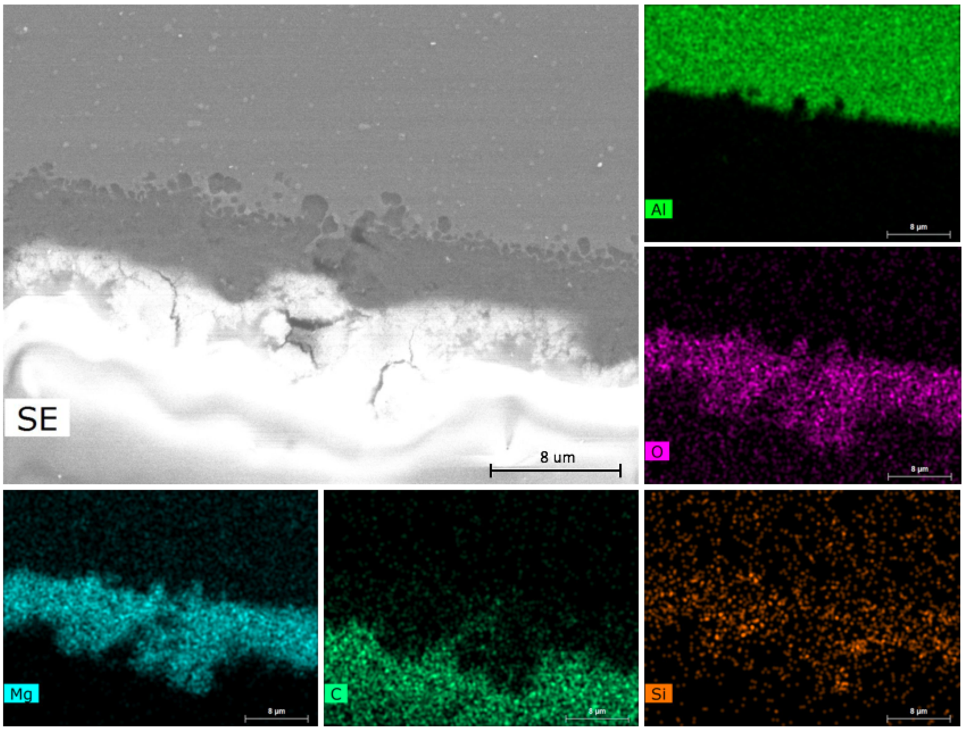

Figure 4.3: Scanning electron microscopy by secondary electron imaging of heat treated AA5183TiC-CG welding wire. Heat treated at 560 °C for 2h in inert argon atmosphere. The white noise in the images is due to charging effects in the SEM. Surface oxide layer is indicated by elemental EDS mapping shown in colored images.

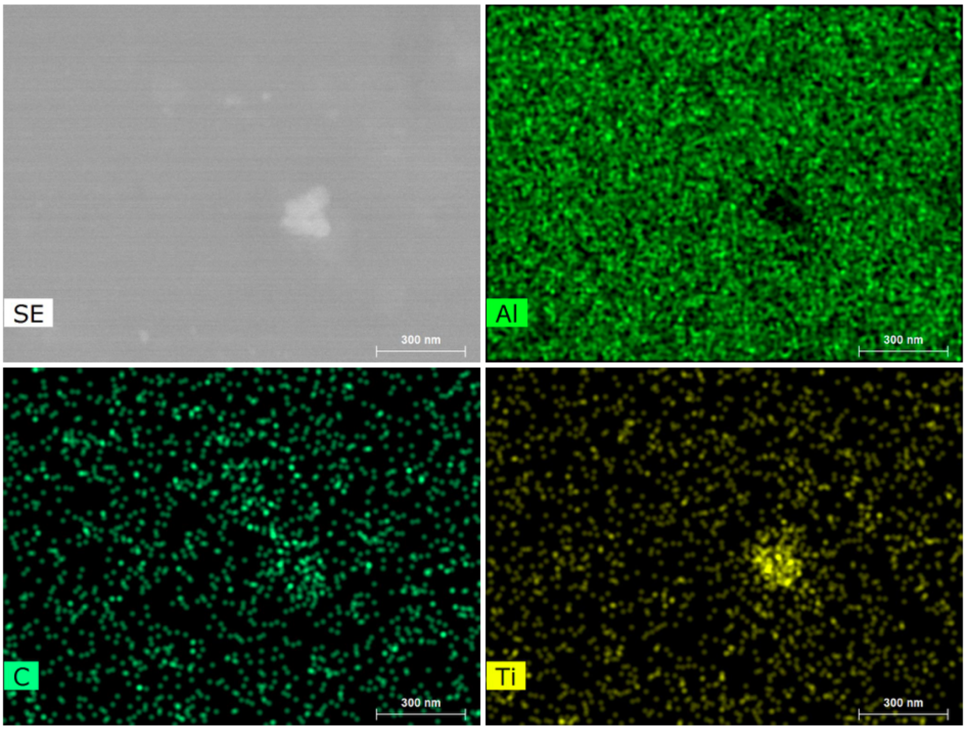

Figure 4.4: Scanning electron microscopy by secondary electron imaging of AA5183TiC-CG welding wire. a TiC nanoparticle is indicated by elemental EDS mapping is shown in colored images.

Figure 4.2 shows the non-heat-treated AA5183TiC-CG welding wire. The wire showed no indication of magnesium-rich surface oxides through EDS mapping. The aluminium and magnesium signal appears to overlap fairly well. Some silicon is detected, due to SiO_2 polishing particles filling voids in the material surface. The carbon signal indicates hardened epoxy resin, for mounting of the sample in SEM.

A TiC nanoparticle was detected in the AA5183TiC-CG wire described above, shown in Figure 4.4. EDS mapping showed a faint carbon signal and clear titanium signal, as well as absence of aluminium in the corresponding area, indicating the grey phase being TiC.

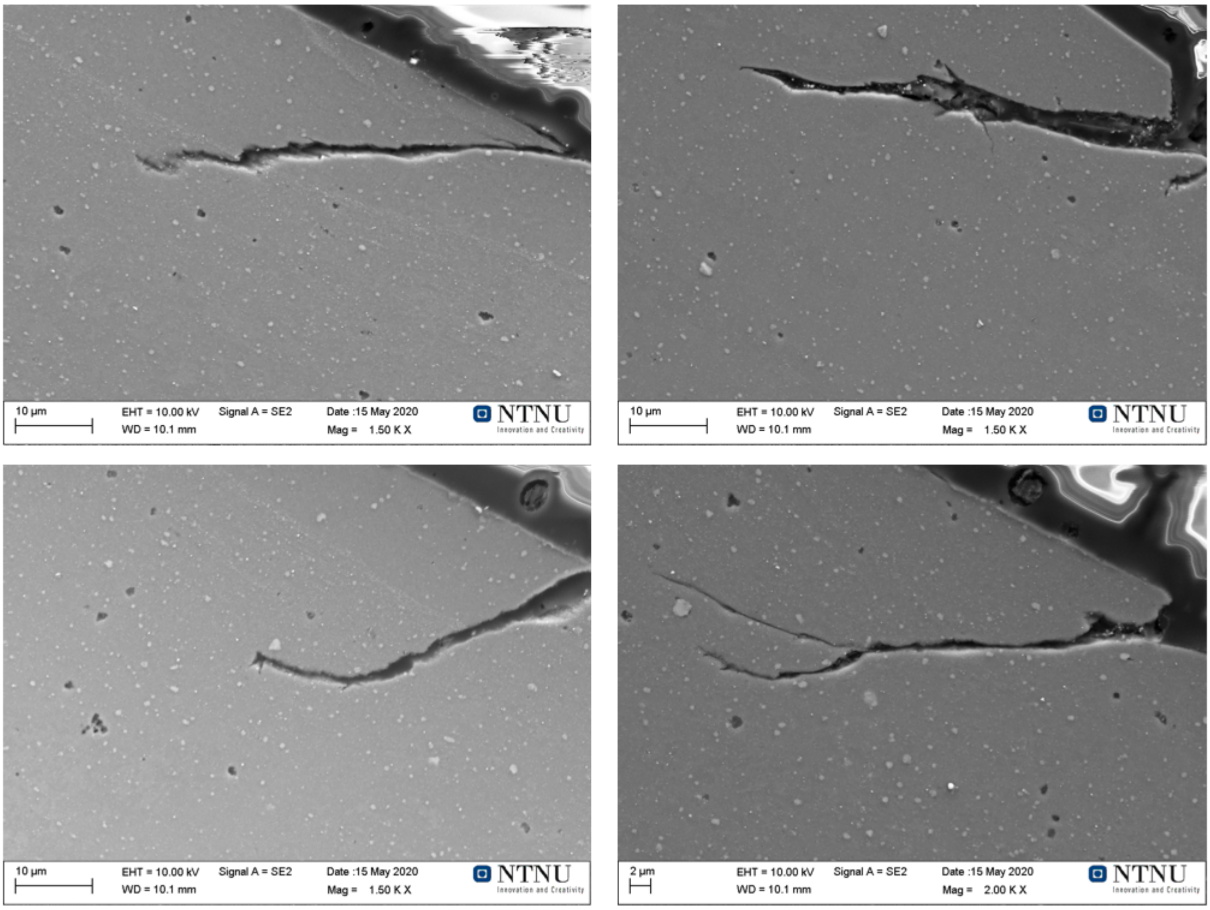

Figure 4.5: Scanning electron microscopy by secondary electron imaging of the AA5183TiC-CG 1.2 mm welding wire. Observed crack lengths were between 20-50 μm.

Figure 4.3 shows heat-treated AA5183TiC-CG welding wire. The heat-treatment of 560 °C for 2h in inert argon atmosphere resulted in a significant oxide formation at the wire surface. Elemental EDS mapping shows a distinct region of magnesium-rich oxides, spanning several micrometers deep in the material. Severe cracking is also observed in the oxide surface.

From examination of the AA5183TiC-CG welding wire, it was observed severe cracking along the wire surface, as shown by Figure 4.5. Cracks were typically observed ranging 20-50 μm in length. The other welding wires showed no signs of cracking along the surface.

4.2 Macroscopic appearance of WAAM thin wall

The additive manufactured WAAM thin wall is shown in Figure 4.6. Visual examination of the thin wall surface indicated no irregularities in the wall structure. The as-built WAAM thin wall measured 223x8x84 mm^3, with only small variations in deposition width. At the edges of the wall, a distinct area different from the rest of the structure can be observed due to different flow characteristic during weld onset. Minor signs of surface porosity was observed between deposition layers.

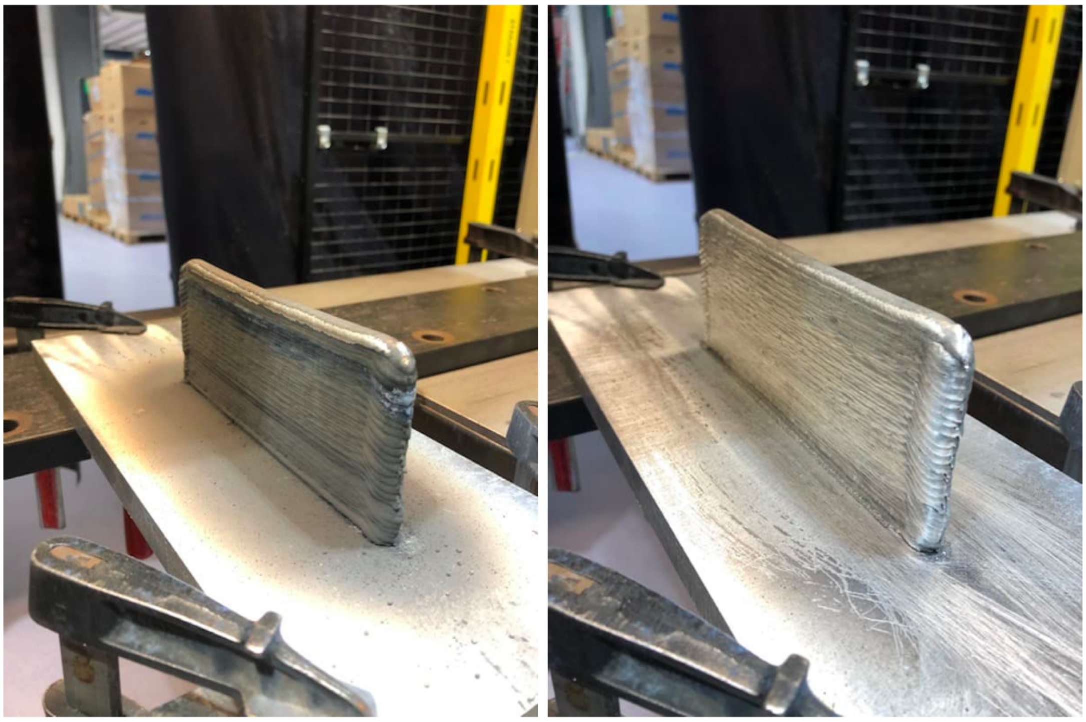

Figure 4.6: As-built WAAM thin wall deposited on a AA6082-T6 base plate. Left image is before cleaning welding soot, right image after cleaning of welding soot.

4.3 Microstructure

In this section, results from microstructure characterization of WAAM thin wall samples are presented.

The anodized mid-section of the WAAM thin wall imaged by optical light microscopy is shown in Figure 4.7. A distinct feature is the transition from long columnar grains to small equiaxed grains. The transition clearly shows the change of feedstock wire for deposition during WAAM, as the initial AA5183-CG wire was changed for a AA5183TiC-CG wire about one third through the deposition. Figure 4.7b shows a higher magnification of the columnar grain region extending away from the fusion zone at previous deposited layer. The length of the the yellow and longest grain was measured to approximately $800\,\mu\mathrm{m}$. A magnified optical light microscopy image of the transition from AA5183-CG wire to AA5183TiC-CG wire is shown in Figure 4.7c, highlighting the abrupt change in both morphology and grain size. Observations of the microstructure near the transition from AA5183-CG to AA5183TiC-CG wire, shows evidence of higher homogeneity for the AA5183TiC-CG section of the WAAM thin wall, although the porosity is far greater. Porosity will be addressed in a subsequent section.

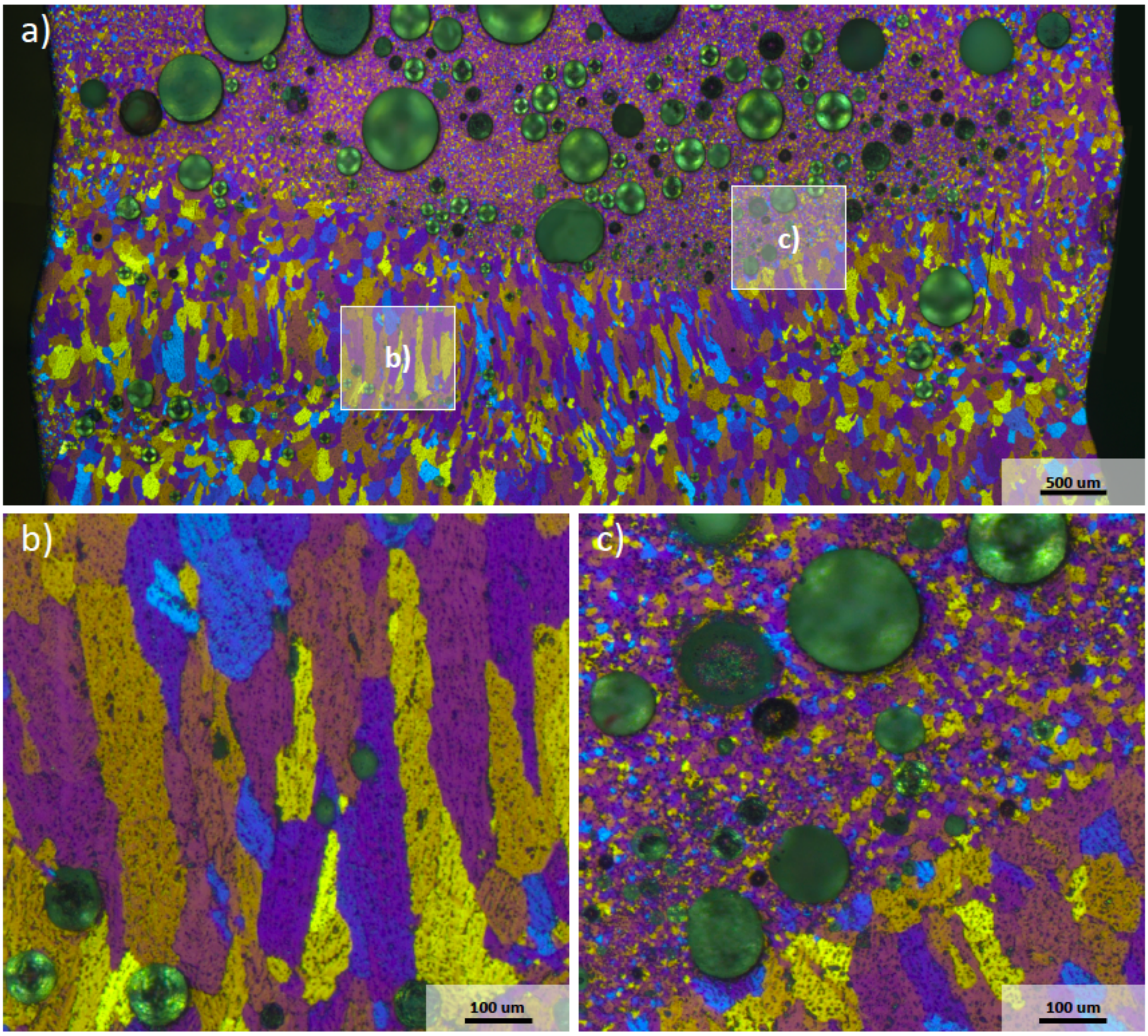

Figure 4.7: Anodized cross-section of the additive manufactured thin wall imaged through optical light microscopy, showing the transition between the AA5183-CG and AA5183TiC-CG deposition layers. (a) full-width of wall, (b) columnar grain structure and (c) transition from large columnar grains to small equiaxed grain structure at the fusion zone.

Significant grain size reduction was observed in the AA5183TiC-CG section, where TiC nanoparticles were introduced to form an aluminium matrix composite (AMC). The average grain size was estimated in both the AA5183-CG layers and AA5183TiC-CG layers. For the initial AA5183-CG layers without TiC-nanoparticles, the average grain size was estimated to $64 \pm 7\,\mu\text{m}$. For the AA5183TiC-CG layers, average grain size was estimated to $9 \pm 2\,\mu\text{m}$. Figure 4.10 demonstrates the grain size difference between AA5183-CG and AA5183TiC-CG layers.

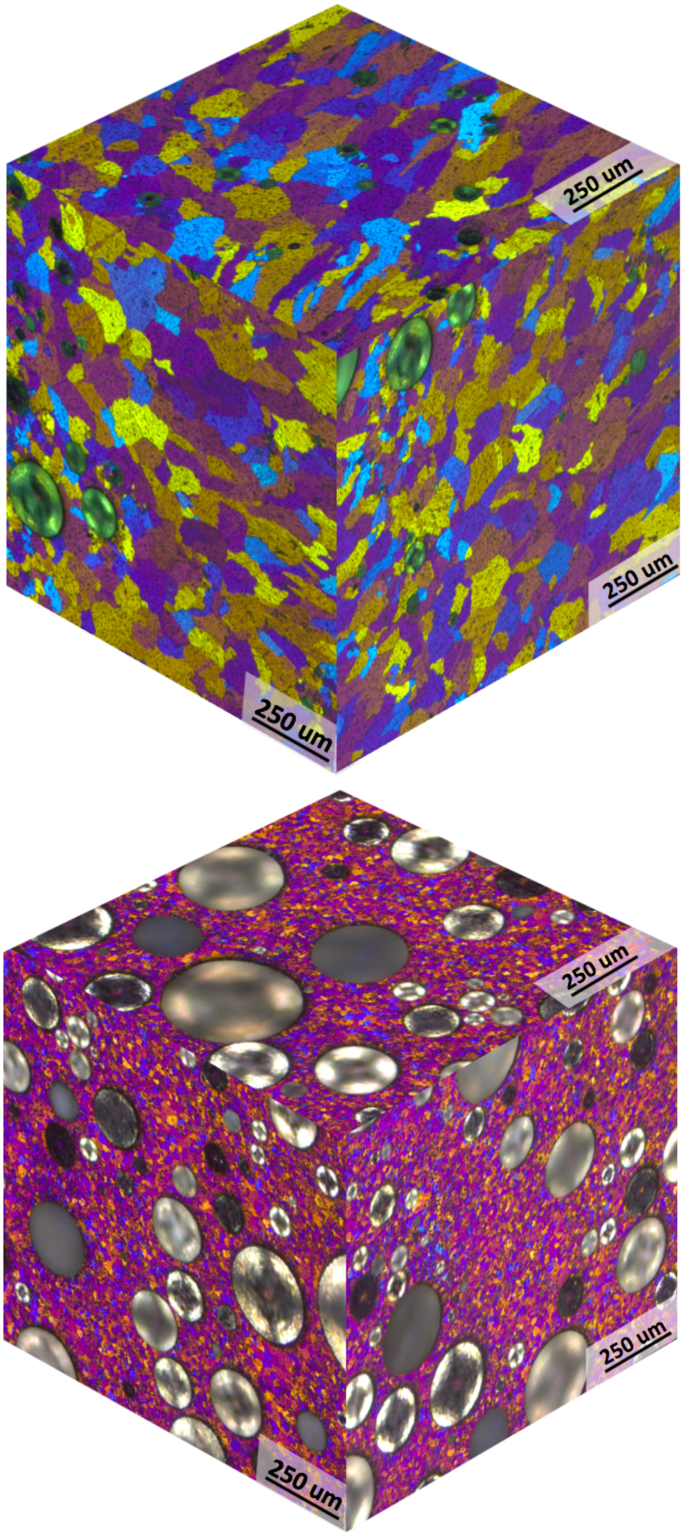

Figure 4.10: Anodized microstructure of AA5183-CG WAAM thin wall section (*upper*), and AA5183TiC-CG WAAM thin wall section (*lower*) imaged through optical light microscopy. Significant grain size reduction was observed. Scale bars are 250 µm.

4.4 Distribution of titanium in the aluminium matrix composite

In this section, distribution of titanium in the WAAM thin wall be presented. Observations were done using scanning electron microscopy (SEM) and EDS mapping for analysis of elemental distribution in the material.

SEM and EDS mapping were performed to examine the titanium distribution in the AA5183TiC-CG section of the WAAM thin wall. Figure 4.11 shows a SEM-image of the AA5183TiC-CG section, together with EDS-signals mapping out the presence of several elements in and around the grains. It appeared that titanium were marbling the grain boundaries, with a low presence within the grains, as visible both as the white signal in the SEM image, as well as yellow signal from EDS. Magnesium segregation to the grain boundaries is visible by EDS mapping. It is believed that voids in the surface are filled with SiO_2 polishing particles from the sample preparation procedure, showing up in the O and Si-signal in EDS. The bright carbon signal is likely due to organic contamination of the sample during preparation or handling. Large white phases in the secondary electron image is believed to be a Mn and Fe-rich phase, confirmed by the EDS signals.

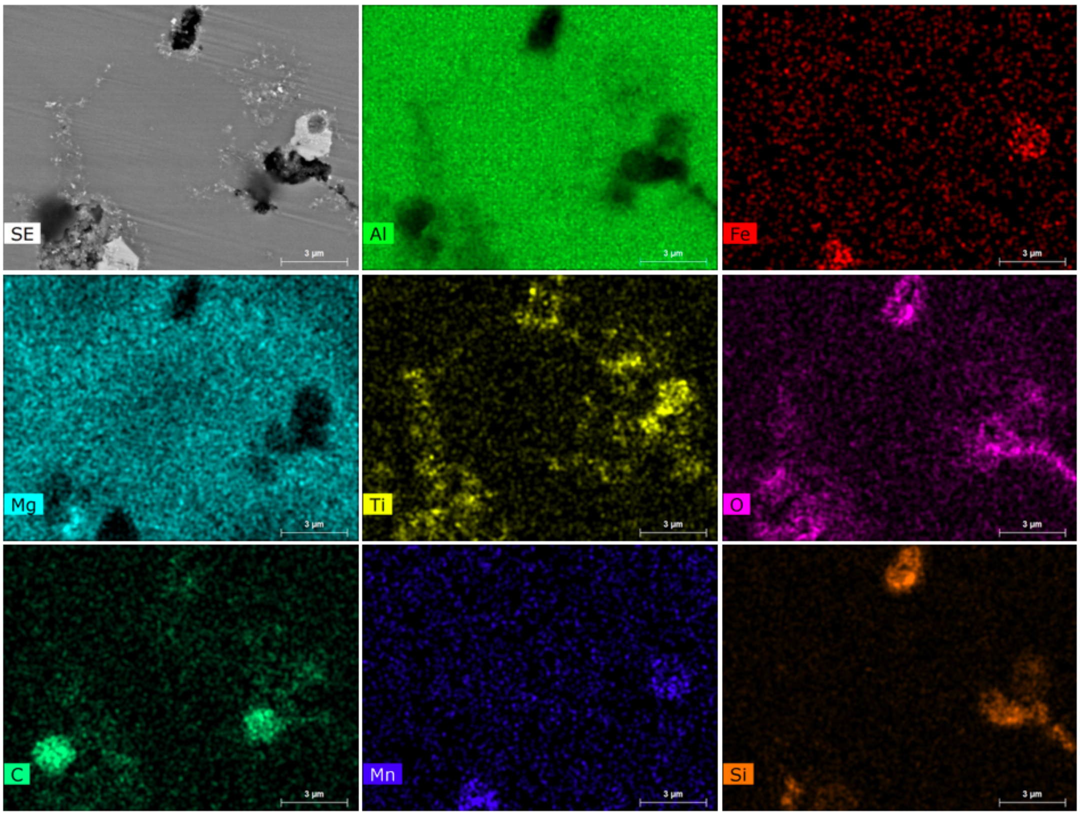

Figure 4.11: Scanning electron microscopy by secondary electron imaging of grain boundaries in the AA5183TiC-CG section of the WAAM thin wall. The grain boundary was found to be marbled with TiC nanoparticles observed by EDS mapping. Elemental distribution was mapped for several elements by EDS. SiO_2 polishing particles from sample preparation procedure is believed to contribute heavily to O and Si signals A magnified image of the white box is found in Figure 4.12, for closer examination of TiC nanoparticles.

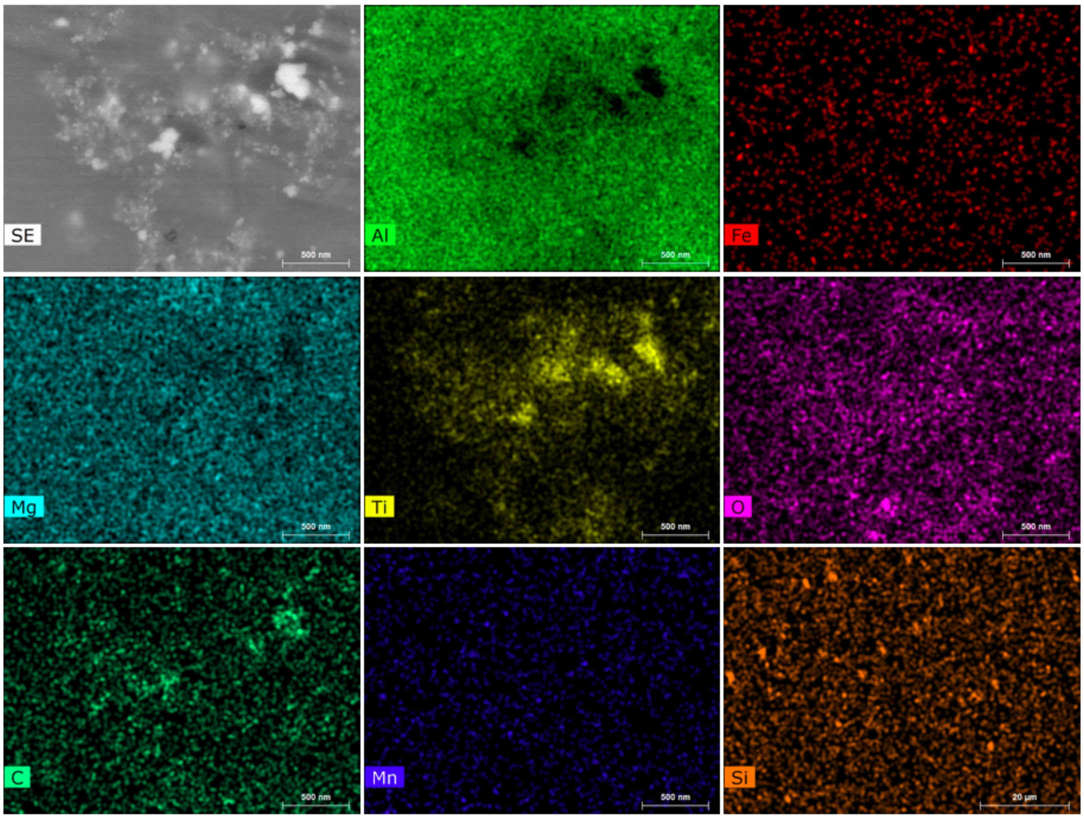

Figure 4.12: Scanning electron microscopy by secondary electron imaging of TiC nanoparticles in the AA5183TiC-CG section of the WAAM thin wall. The presence of TiC nanoparticles is indicated using EDS, with significant signals for both Ti and C.

Figure 4.13 shows the cross-section of a pore, capturing a fraction of the total pore volume. Multiple TiC nanoparticle clusters are visible, as they reside at the grain boundaries. A higher magnification image of the white dashed box in Figure 4.13 is shown in Figure 4.14. TiC nanoparticles are observed to agglomerate in large clusters, 100-300 nm in diameter. Single TiC nanoparticles is distinguishable from the scanning electron microscopy image.

Figure 4.15 shows a cross-section of the WAAM thin wall imaged by scanning electron microscopy, and analysed using EDS mapping. The microstructure revealed several locations of titanium rich intermetallic compounds. From EDS mapping, it is assumed that the grey phases are Al_3Ti. The intermetallic Al_3Ti phase is found mainly at grain boundaries. Elemental EDS mapping shown in the figure, shows a significant Ti-signal. Segregation of magnesium to the grain boundaries is also observable in the aluminium matrix composite through EDS mapping. A magnified image of the Al_3Ti intermetallic is shown in Figure 4.16, together with EDS mapping of aluminium. magnesium and titanium. The morphology of the phase seems to be highly ordered, likely due to preferred growth directions in the crystal structure. It seems that multiple phases grow separately until impingement onto each other. The formation of an intermetallic phase points towards chemical reactions between TiC nanoparticles and the aluminium matrix during manufacturing.

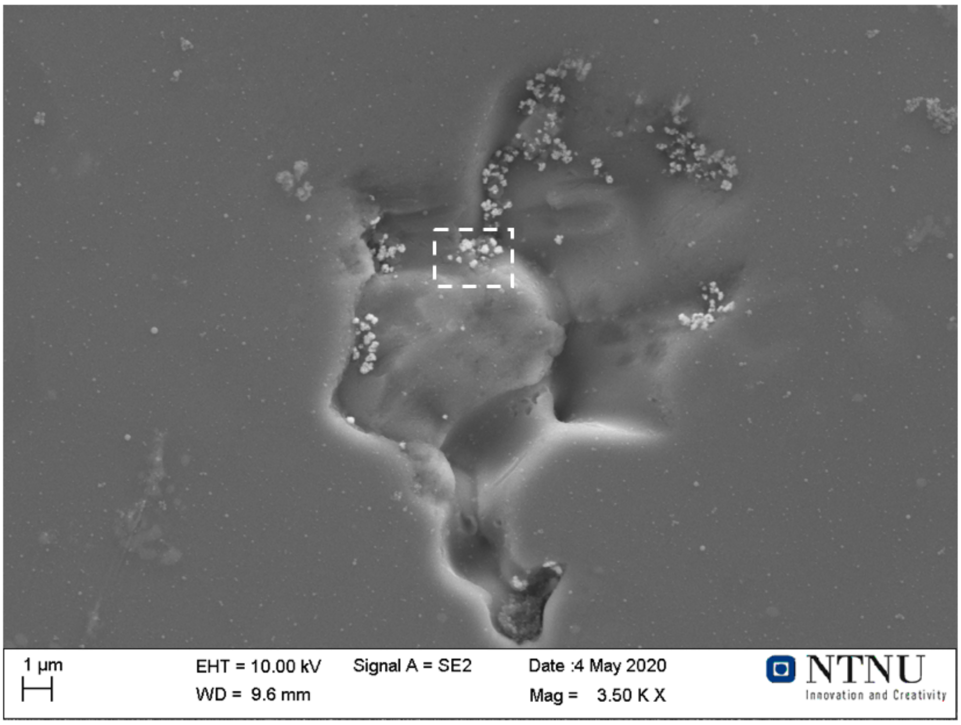

Figure 4.13: Scanning electron microscopy by secondary electron imaging of the AA5183TiC-CG section of the WAAM thin wall. White particles are TiC nanoparticles, mainly observed at grain boundaries. The inserted white box is examined at higher magnification in Figure 4.14.

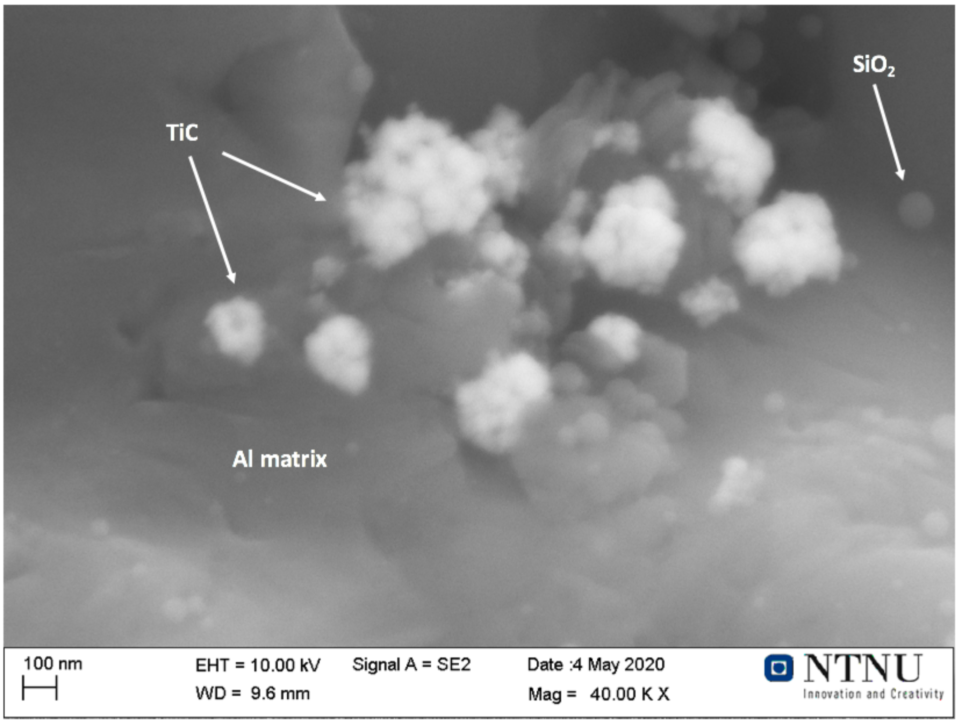

Figure 4.14: Scanning electron microscopy by secondary electron imaging shows the AA5183TiC-CG section of the WAAM thin wall. Arrows identify compounds. White particles are TiC, spherical gray particles are SiO_2 continamination from polishing sample preparations.

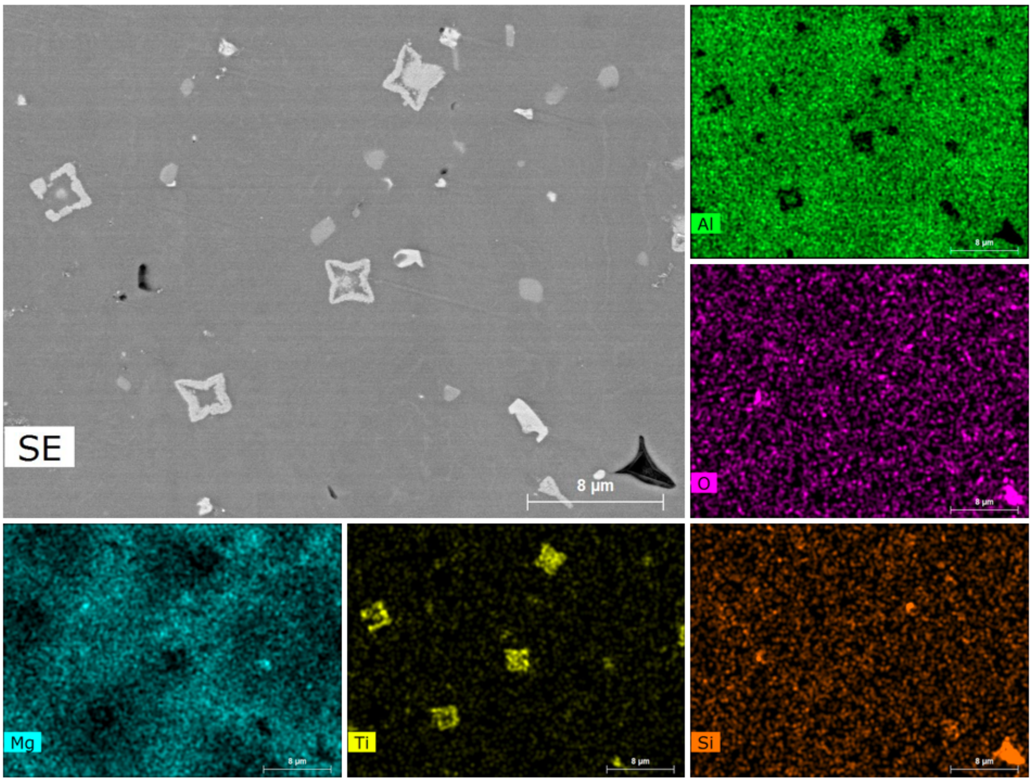

Figure 4.15: Scanning electron microscopy by secondary electron imaging shows the AA5183TiC-CG section of the WAAM thin wall. Grey phases indicate Al_3ti intermetallic compound, identified using EDS.

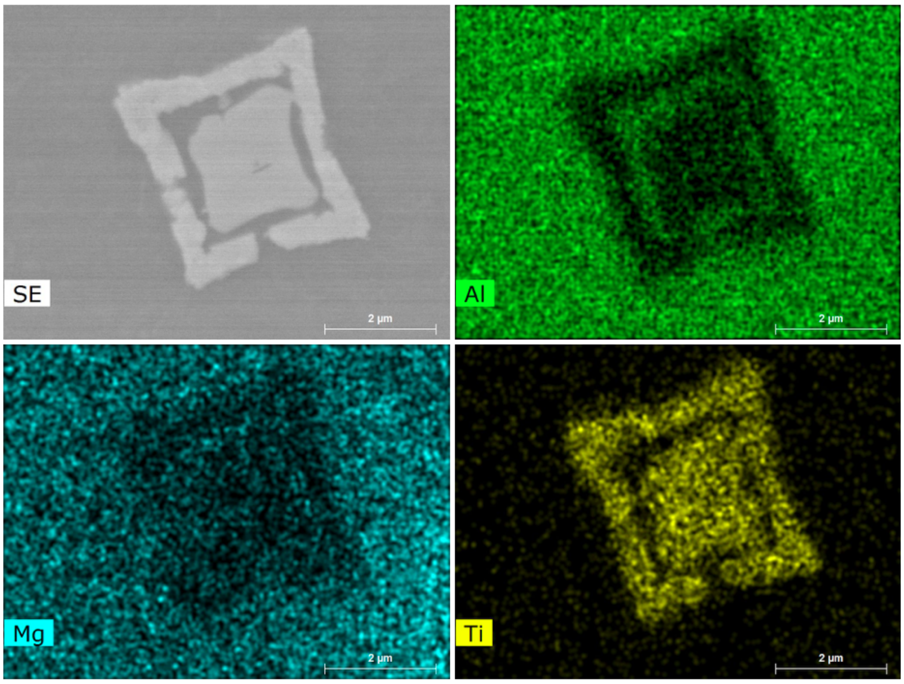

Figure 4.16: Scanning electron microscopy by secondary electron imaging shows the AA5183TiC-CG section of the WAAM thin wall.Al_3ti intermetallic compounds was found to reside at grain boundaries, appearing with a highly ordered crystal structure.

4.5 Porosity

In this section, porosity characteristics obtained of the WAAM thin wall using *Scanning electron microscopy* (SEM), *Energy-dispersive X-ray spectroscopy* (EDS) and *Micro X-Ray computational tomography* (micro-CT) are presented.

A full mapping of porosity in the WAAM thin wall was obtained using micro-CT, as presented in Figure 4.17.

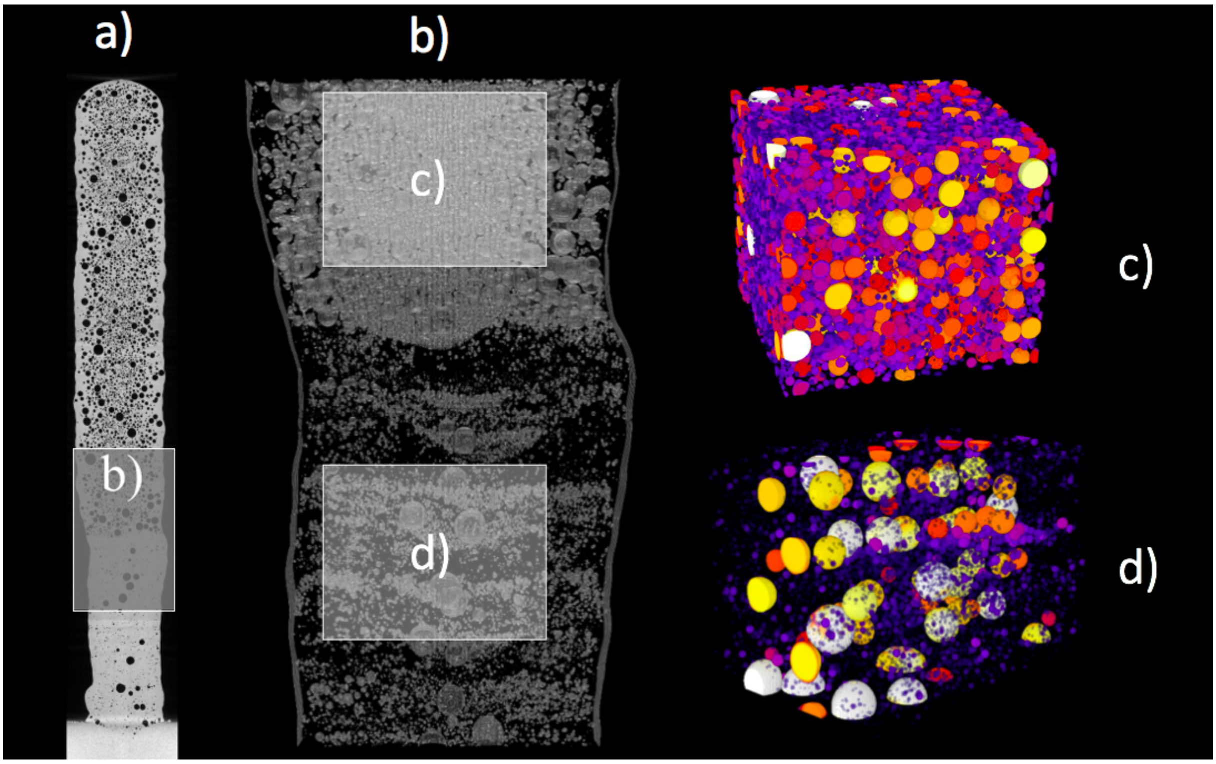

Figure 4.17: Two and three-dimensional mapping of porosity in the WAAM thin wall obtained through *Micro X-Ray computational tomography* (micro-CT). a) shows the full cross-section of the WAAM thin wall in the longitudinal direction. Porosity in the WAAM thin wall are visible in black, being superimposed and projected onto the 2D-plane. The boxed section b) indicates the transition from AA5183-CG welding wire to AA5183TiC-CG welding wire, shown in higher magnification. Pores are here visible in grey, as the metal matrix is subtracted for this mapping technique. Box c) and d) show mappings of porosity in a 60x60x60 mm area of the AA5183TiC-CG section and 60x80x60 mm area of the AAA5183-CG section, respectively. The color gradient in c) and d) indicates pore diameter, as small pores are colored blue and large pores are colored bright white. All data processing was done in *Fiji ImageJ* and *BoneJ* plug-in software [117][118].

Figure 4.17a shows the full cross section of the WAAM thin wall obtained through micro-CT-scanning. From micro-CT scans, extreme porosity of the AA5183TiC-CG WAAM thin wall section is discovered. A relatively uniform distribution of the pores are observed for the AA5183TiC-CG section. Examination of the AA5183-CG section revealed far lower porosity, compared to AA5183TiC-CG.

Figure 4.17b shows that porosity of the AA5183-CG section is concentrated layerally in regions corresponding to transition between individual deposition layers during WAAM. The large difference in porosity between the two welding wires reveals a definitive transition region in the WAAM thin wall, as welding wires were changed during manufacturing.

Figure 4.17c and Figure 4.17d show a 60x60x60 mm three-dimensional mapping of pores for two corresponding areas in the WAAM thin wall, AA5183-CG and AA5183TiC-CG respectively. The colorization of the pore volume corresponds to the pore diameter for easier comparison. Pore volume in the upper AA5183TiC-CG section of the WAAM thin wall was estimated to 25 vol%.

Figure 4.18 shows a logarithmic plot of pore diameter in the two different sections of the WAAM thin wall. Due to low spatial resolution using micro-CT, only pores above 20 µm/pixel in diameter are considered. From the plot, it is observed that the AA5183TiC-CG WAAM thin wall section have a considerable larger pore content than the unreinforced AA5183-CG.

The pore array index indicates the number of pores in a selected area of 600x600x100 pixels from the micro-CT scan. A large pore array index translates to a large number of pores in the selected area. The largest pore diameter in each section is indexed as pore number one, with the next largest pore diameter being pore number two. This method is used for indexing all pores down to a diameter equalling the spatial resolution limit.

Examination of the logarithmic plot reveals several pores in the AA5183TiC-CG section exceeding 1000 µm in diameter. For the AA5183-CG section, the largest pores are measured in the range of 100-150 µm, which is one-tenth the diameter of TiC nanoparticle reinforced AA5183.

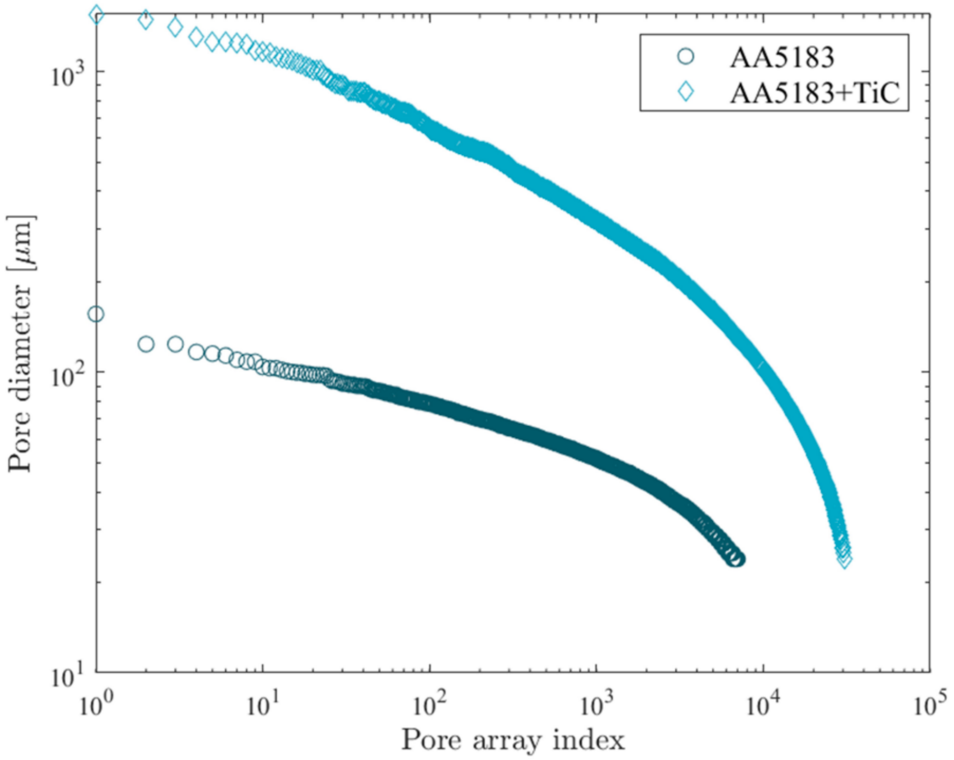

Figure 4.18: Logarithmic plot of pore diameter for the two different sections of the WAAM thin wall. Pores are sorted from largest to smallest diameter for two corresponding regions in each wall section. The measured volume was 600x600x100 pixels. One index point represents one pore. The AA5183-TiC region exhibits far greater pore density compared to the AA5183 region. Data processing was done in *Fiji ImageJ* using *BoneJ* plug-in software, then plotted using *MATLAB* [117][118].

The addition of TiC nanoparticles to the AA5183 aluminium alloy during MCSE increased pore diameter post-WAAM significantly. Average pore diameter in the AA5183TiC-CG section of the WAAM thin wall was found to be $102\,\mu\mathrm{m}$, whereas the AA5183-CG section was found to exhibit average pore diameter of $42\,\mu\mathrm{m}$. A 143% increase in average pore diameter with TiC nanoparticle reinforcement.

Examination of individual pores in the WAAM thin wall were carried out using SEM, enabling better observations of the pore morphology and features in the interior pore volume.

Figure 4.19 shows a typical pore observed in the AA5183TiC-CG section of the WAAM thin wall, exhibiting an almost perfect spherical appearance. The interior grain structure is distinctly visible within the pore volume, with well-defined grain boundaries. Pore diameter is measured to approximately $165\,\mu\mathrm{m}$.

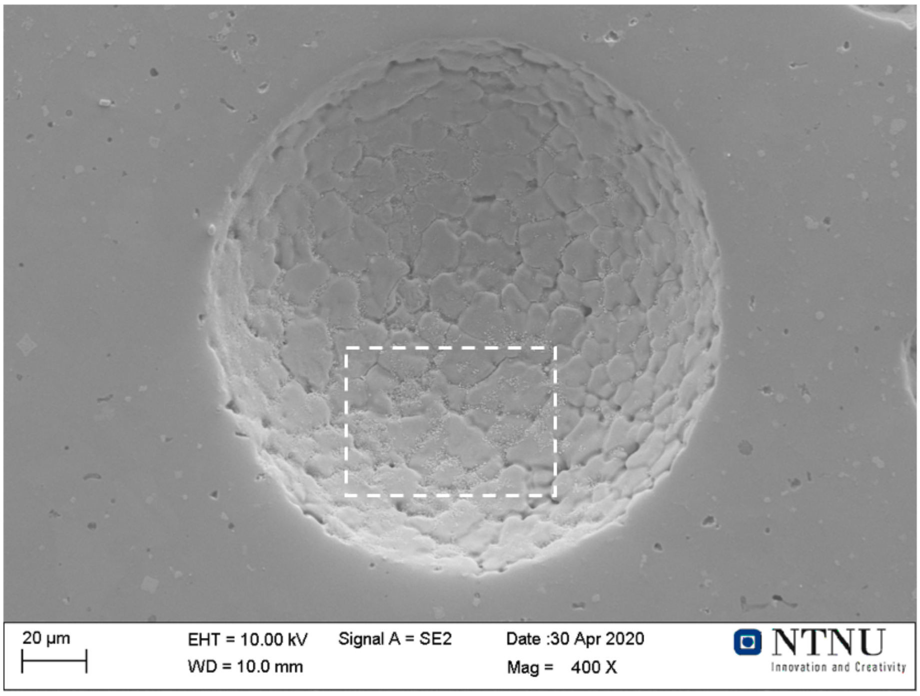

Figure 4.19: Scanning electron microscopy by secondary electron imaging shows a mid-sized highly spherical pore in the AA5183TiC-CG section of WAAM thin wall. Grain boundaries are revealed in the pore interior volume. Higher magnification image of the white dashed box is shown in Figure 4.20.

A higher magnification image of the white dashed box is shown in Figure 4.20, with the appearance of some sort of clustering at the grain boundaries. Individual α-phase aluminium grains are easily distinguishable at this magnification.

Figure 4.21 shows a high magnification image of a single α-phase aluminium grain in the pore interior volume. The grain measures approximately $10\,\mu\mathrm{m}$ in length from the top to bottom. The white particles seen at the grain boundaries were confirmed by EDS to be agglomerated TiC nanoparticles, as shown at higher magnification in Figure 4.14.

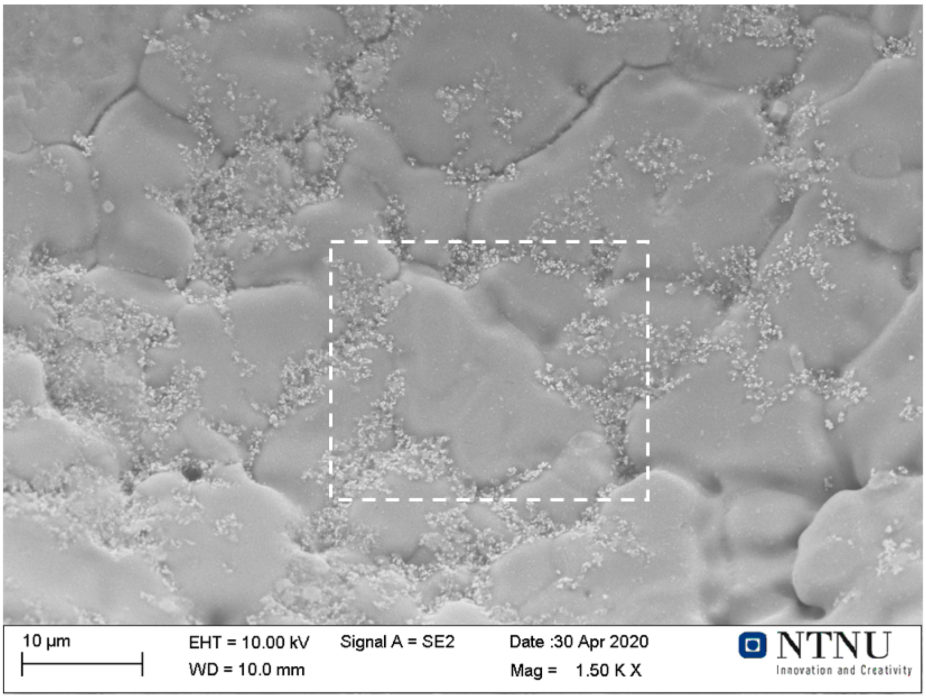

Figure 4.20: Scanning electron microscopy by secondary electron imaging shows the the AA5183TiC-CG section of WAAM thin wall. Magnified image of the pore interior volume in the white dashed box in Figure 4.19. Higher magnification image of the White dashed box is seen in Figure 4.21.

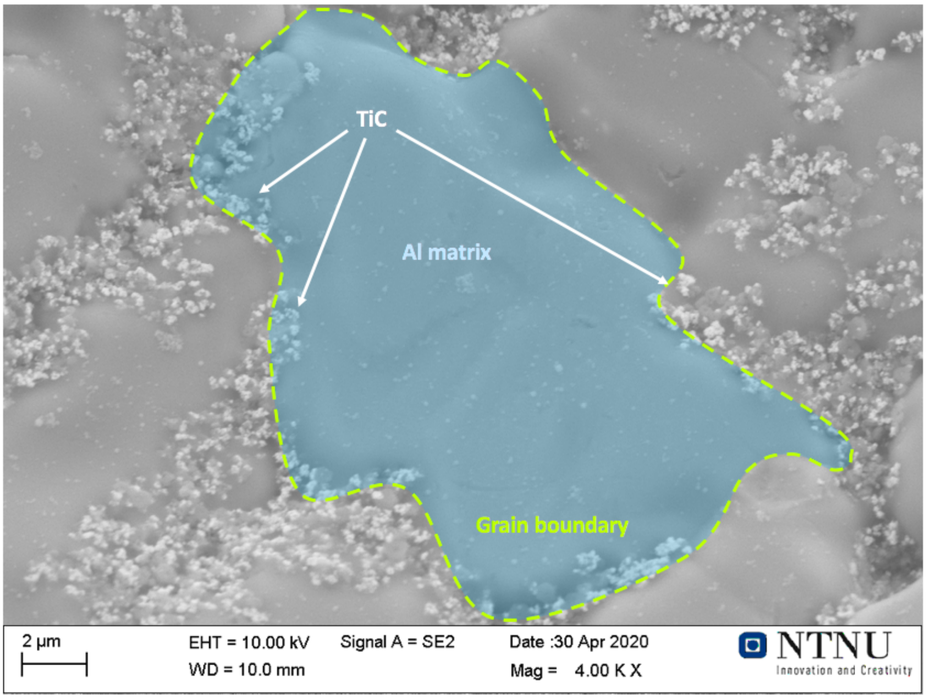

Figure 4.21: Scanning electron microscopy by secondary electron imaging shows the AA5183TiC-CG section of WAAM thin wall. Magnified image of pore interior volume in white dashed box in Figure 4.20. White particles were examined by EDS, indicating TiC nanoparticle agglomeration. Blue indicates grain interior, whereas grain boundary in dashed green.

To obtain a detailed examination of phases formed inside the pore interior during WAAM, EDS mapping was carried out in an area of grain boundary agglomerated phases. The examination is shown in Figure 4.22. It appears that pores exhibit large oxide formation in the pore interior. The magnified SEM secondary electron image of the pore interior revealed ordered crystal structures pinned at the grain boundaries. Oxygen and magnesium enrichment in the pore interior during WAAM is assumed to form spinel group oxide mineral $MgAl_2O_4$, indicated by EDS mapping showing highly ordered crystal structures. The Ti-signal indicate agglomeration of TiC at the grain boundaries. Some silicon-rich phases is indicated, as well as a manganese and iron-rich phase.

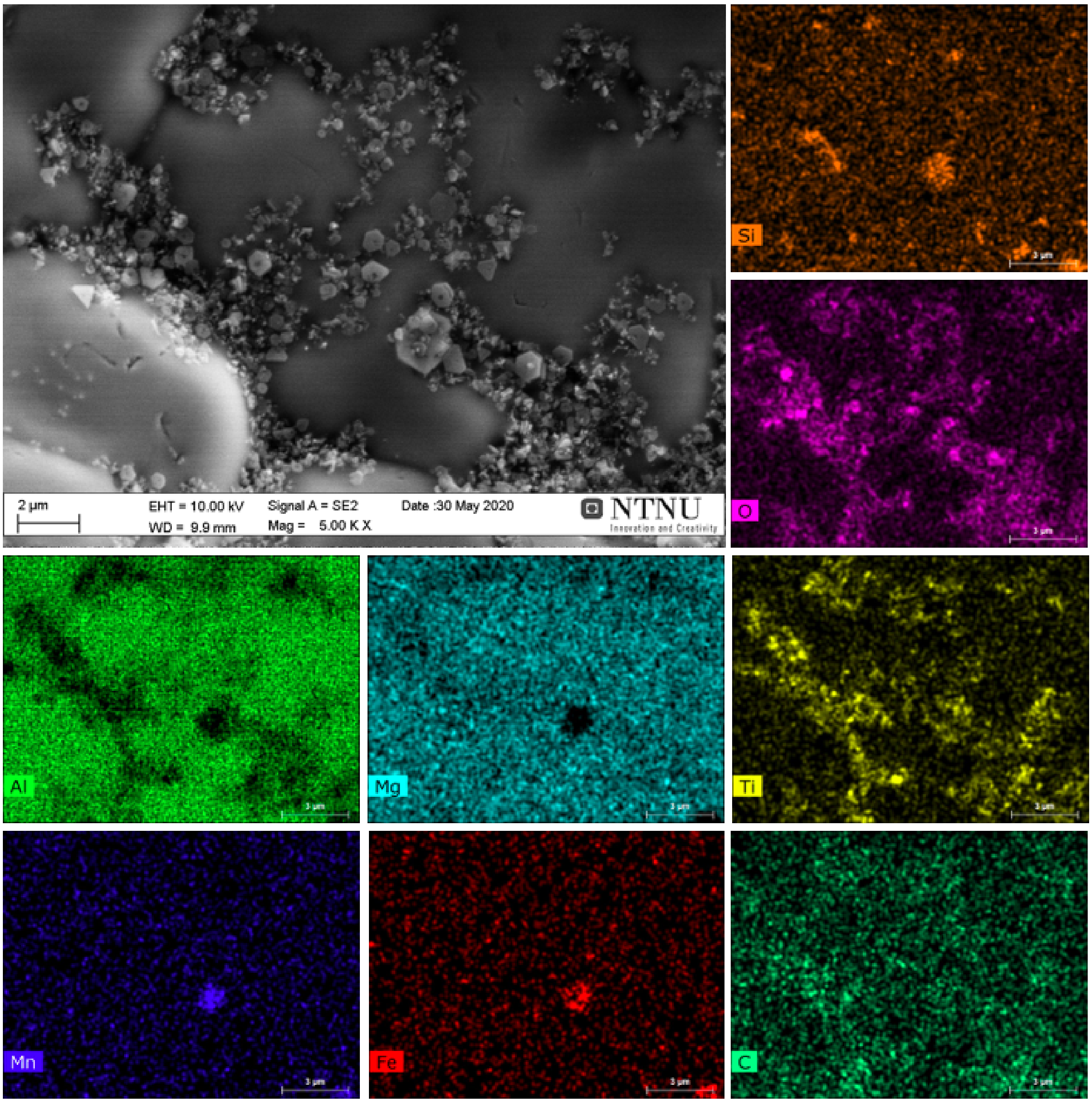

Figure 4.22: Scanning electron microscopy by secondary electron imaging shows the AA5183TiC-CG section of WAAM thin wall. The magnified image shows the interior of a relatively large pore. From EDS mapping, hexagonal spinel group oxide mineral $MgAl_2O_4$ is assumed to form due to magnesium enrichment during WAAM. Grain boundaries shows titanium signal, indicating agglomeration of TiC nanoparticles. Silicon-containing phases, as well as manganese and iron-rich phases are indicated from EDS.

Apart from spherical shaped pores, a considerable amount of irregular pores were observed between individual grains, likely as a results of shrinkage effects and insufficient back-filling of dendrite channels during solidification.

Figure 4.23 shows irregular shaped pores in the AA5183TiC-CG section of the WAAM thin wall. EDS point signals found in section B in Appendices shows oxygen-rich phases in the vicinity of the pores. EDS mapping shown in Figure 4.11 may be consulted in terms of the irregular pores in the top section of the SEM secondary electron image. The irregular pore seems to exhibit phases rich in titanium, silicon and oxygen. Absence of aluminium and magnesium is clearly observed. Most irregular pores were found with diameters in the range 1-5 $\mu\mathrm{m}$. Gray phases observed in Figure 4.23 were indicated to be intermetallic Al_3Ti, as confirmed in earlier sections. A higher magnification image of the white dashed box in Figure 4.23 is shown in Figure 4.24. The grey spherical particles are indicated to be SiO_2, contamination from sample preparation polishing. White phases are oxygen-rich phases. The phase within the white dashed encapsulation was indicated to be manganese-rich.

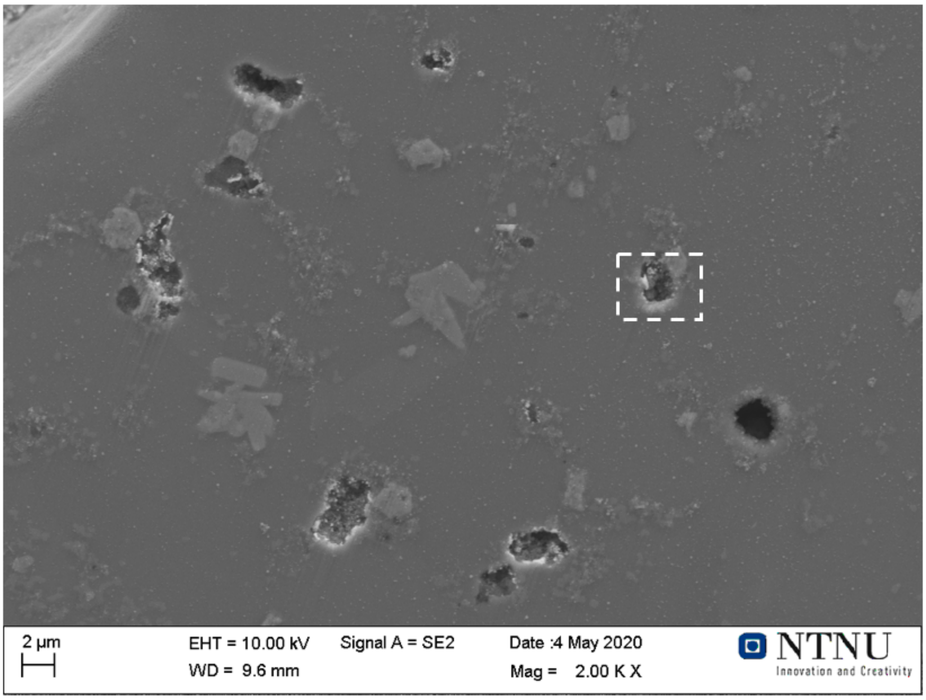

Figure 4.23: Scanning electron microscopy by secondary electron imaging shows irregular pores in the cross-section of WAAM thin wall. The imaged section is AA5183TiC-CG. Pores with low sphericity appears in-between grains at the grain boundaries, found to contain high amounts of oxides through EDS point mapping is seen in section B in the appendices. The grey phases were indicated to be intermetallic Al_3Ti. Higher magnification image of the white dashed box is seen in Figure 4.24.

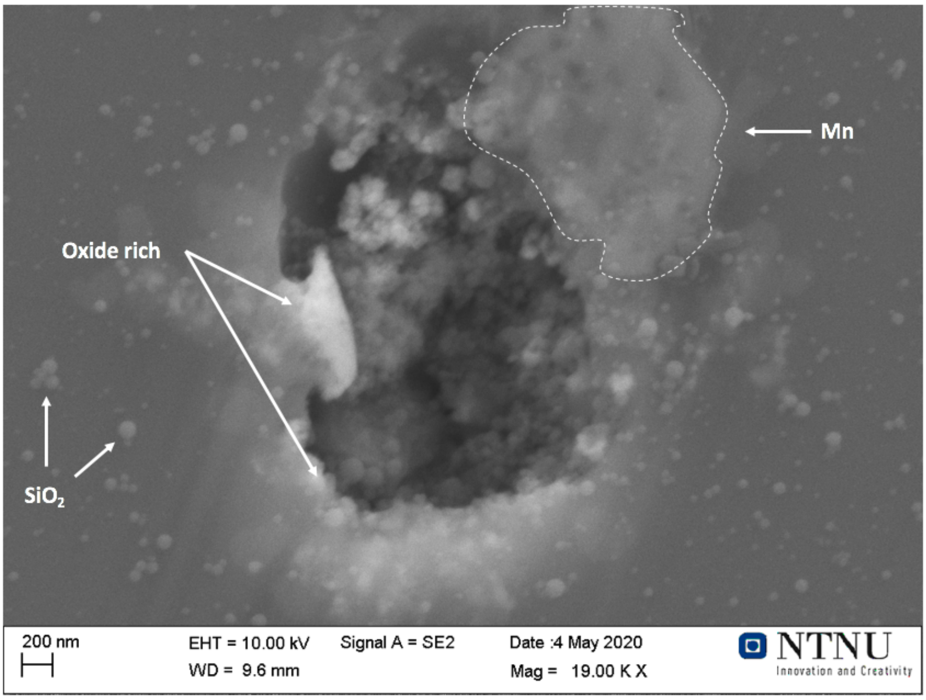

Figure 4.24: Scanning electron microscopy by secondary electron imaging shows irregular pores in the cross-section of WAAM thin wall. The imaged section is AA5183TiC-CG. EDS point mapping (section B in the Appendices) indicated contamination from SiO_2 polishing particles, as shown by white arrows. A manganese-rich phase was initiated at the pore-grain interface. Bright areas at the pore-grain interface were found to contain large amount of oxygen.

4.6 Microhardness

In this section, microhardness measurements of the cross-sectional WAAM thin wall sample will be presented.

Microhardness measurements were taken for only the AA5183TiC section. 15 indents confirmed a average microhardness of $88 \pm 5\ HV_{0,1}$. Some of the indents are believed to decrease the overall measured microhardness, as the porosity of the AA5183-TiC results in hidden pores marginally beneath the surface of indents.

4.7 Tensile properties

In this section, the tensile properties of the WAAM thin wall is presented.

Six cross-sectional samples of the WAAM thin wall were tested, three parallel to the deposition direction, and three perpendicular to the deposition direction. The resulting engineering stress-strain curves are presented in Figure 4.25.

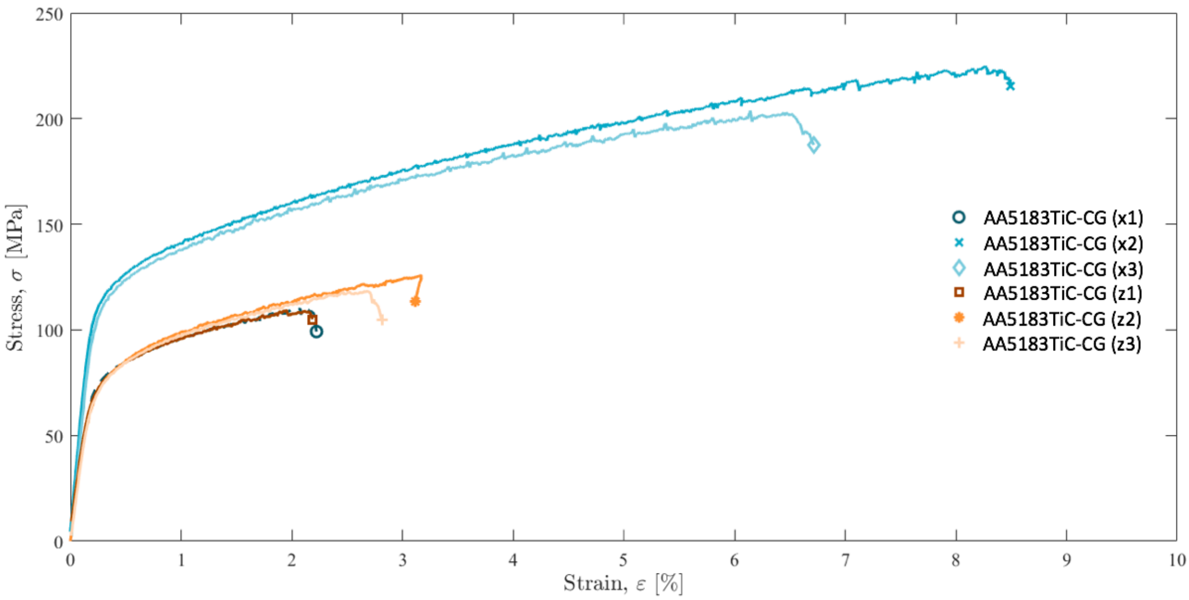

Figure 4.25: Stress-strain curves from tensile tests of cross-sectional WAAM thin wall sample. Tests performed on samples parallel to welding direction is denoted x, and perpendicular samples denoted z. A constant strain rate of $2\,\mathrm{mm\,min}^{-1}$was applied.

Ultimate tensile stress, σ_{UTS}, is the the highest measured nominal strength value for each curve. The plotted engineering stress, σ in the figure is used to calculate the yield strength, σ_Y. The value is calculated using the 0.2% strain off-set. The strain, ϵ, at fracture is the elongation, EL, of each sample. The values for tensile specimens are presented in Table 4.1.

Table 4.1: Yield strength, σ_Y, ultimate tensile strength, σ_{UTS}, and elongation, EL, of cross-sectional WAAM thin wall samples. Parallel with welding direction denoted x, perpendicular denoted y. A constant strain rate of $2\,\mathrm{mm\,min}^{-1}$was applied. Measurements done using an 25 mm extensiometer.

Sample	σ_Y [MPa]	σ_{UTS} [MPa]	EL [%]
x1	82.8	109.8	2.2
x2	126.5	224,7	8.5
x3	121.7	203.8	7.0
z1	82.2	109.4	2.2
z2	82.2	126.1	3.2
z3	81.9	118.3	2.8

From Figure 4.25 and Table 4.1 it can be observed that the parallel samples (x1) and (x2), show greater elongation than the other samples, with the parallel sample (x3) showing lowest ultimate tensile strength, σ_{UTS}. The observed weakness in (x1) is likely due to large porosity in the sample rod. The yield strength is noticeably larger for (x2) and (x3), compared to (x1). Due to the early fracture of (x1), both (x2) and (x3) show far greater elongation. The tensile samples in the perpendicular deposition direction shows inferior ultimate tensile strength, σ_{UTS}, to the parallel samples. Extreme porosity renders the characterization of tensile properties highly uncertain, and yields no significant results for proper comparison. The low ductility is likely attributed to both grain structure and inter-layer porosity.

Chapter 5

Discussion

5.1 Heat-treatment of feedstock material

In this section, heat-treatment of the AA5183 feedstock material will be discussed. An assessment of both MCSE 10 mm extrudate profiles and the drawn and shaved 1.2 mm WAAM welding wires will be given.

5.1.1 MCSE 10 mm extrudate profiles

Examination of the heat-treated MCSE 10 mm extrudate profiles from Figure 4.1, revealed severe cracking of AA5183-CG, AA5183 and AA5183TiC. AA5183TiC-CG appeared to show no signs of cracking. For AA5183-CG and AA5183, it was observed cracking circular shaped cracks in the transversal cross-section of the extrudate samples. It is assumed that cracking occurs as result of insufficient mixing during MCSE, creating a lamellar structure containing oxide-rich regions. The oxide content in the extrudates are thought to originate from the feedstock preparation prior to MCSE. The cut AA5183 welding wire supplied by *Safra* is believed to hold a substantial amount of surface oxides, which were subsequently mixed in the extrusion process. During post-extrusion heat treatment at 560 °C for 2h, molecular hydrogen development occurs, leading to trapped hydrogen forcing crack formation in the lamellar zone of the material.

The increased temperature during heat-treatment causes the hydrogen mobility to increase, leading to redistribution of hydrogen through formation of molecular hydrogen. Molecular hydrogen is unable to reside at interstitial sites in the aluminium lattice, which leads to expansion of already existing micro-cavities in the material. It should be noted again, that AA5183-CG and AA5183 extrudate samples were taken from the initial extrudate profile, as AA5183TiC-CG and AA5183TiC were taken from extrudate profiles produced during more stable processing conditions. Regardless, the heat-treatment results indicates that the use of CO_2 cover gas during MCSE results in lower oxide containing and denser extrudates.These observations are corroborated in previous MCSE research by Berulfsen [11] and Stedje [10]. The compaction and mixing issues in MCSE are carefully described by Skorpen [6]

5.1.2 Welding wire 1.2 mm

From results presented in Figure 4.2 and Figure 4.3, there was no significant observation of increased porosity in the welding wire after heat-treatment. By comparison of the two figures showing EDS mapping of the each wire, it was observed that a oxide surface layer formed at elevated temperatures. The oxide layer formation is assumed to form due to increased magnesium diffusion through the aluminum matrix at high temperatures. The oxide layer is believed to contain mainly MgO and $MgAl_2O_4$, according to litterature presented in Section 2.1.3.

The amount of surface oxides will not reach equivalent thickness as heat-treatment experiments during WAAM, as high temperature only lasts for milliseconds. Some surface oxide formation is nevertheless expected.

Agglomerated TiC nanoparticle clusters were observed to be uniformly distributed in the welding wires manufactured by MCSE. Although the particles were clustered, distance between clusters were in the micrometer range. From Figure 4.4, the grey agglomerated TiC nanoparticle cluster is observable in the upper left image. EDS mapping showed presence of both titanium and carbon, strongly indicating TiC particles.

From Figure 4.5, cracking of the AA5183TiC-CG welding wire was confirmed. The cracking may be a result of blistering on the surface of the extrudate 10 mm profiles, as hydrogen expands cavities during screw extrusion. When the blistered welding wire is drawn and shaved, blisters may open up, exposing the cavity on the surface of the wire. A welding wire with cracks can possibly carry unwanted organic grease as well as trapped hydrogen. Additionally, the increased surface area favours larger surface oxide formation when in contact with the ambient atmosphere. The state of the AA5183TiC-CG wire was not optimal for WAAM.

5.2 Macroscopic appearance of WAAM thin wall

In this section, a brief discussion on the macroscopic appearance of the WAAM thin wall be given.

As observed from Figure 4.6, the as-built WAAM thin wall manufactured from AA5183TiC-CG and AA5183-CG welding wire, showed no irregularities after deposition. Although the first layer was deposited using the MIG-P welding method for sufficiently good adhesion to the AA6082 base plate, porosity in the first deposition layer indicated brittle material properties, rendering the WAAM thin wall poorly attached to the AA6082 base plate. The poor attachment may be caused by insufficient oxide and grease cleaning of the AA6082 base plate, in combination with high heat input and thus excessive pore formation.

In addition to the MIG-P arc mode used for the adhesion layer, CMT was used for the remaining layers in the WAAM thin wall. By switching from MIP-P to CMT, heat input was gradually reduced from 424 J/mm to 101 J/mm , as the wire feed speed decreased from 11.2 m/min for the first layer, to 5.8 m/min for the upper layers, as tabulated in Table 3.2. Large gas bubbles were observed to escape the molten metal during deposition, may caused by stirring of the melt pool. Porosity were also observed between deposition layers in the as-built WAAM thin wall. A more thorough discussion of porosity will be given i Section 5.4.

Minor deflection of the AA6082 base plate was observed post-WAAM, likely caused by the residual stresses built up from the non-symmetric heat distribution during deposition. Some research has gone into the effect of pre-heating the base plate, as it is believed to reduce residual stresses [119]. Pre-heating is assumed to minimize heat conduction during deposition and hence heat loss, resulting in smaller temperature gradients. Xiong *et al.* [120] reported that pre-heating affected the temperature gradient with varying pre-heating temperatures, as shown in Figure 5.1 for steel. By pre-heating at 600 °C, a 18% reduction of the temperature gradient can be achieved compared to the room tempered base plate for steel. From the figure, it can be seen that the temperature gradient continues to decrease with increased deposition height, which is assumed to minimize crack susceptibility and thermal stresses [120].

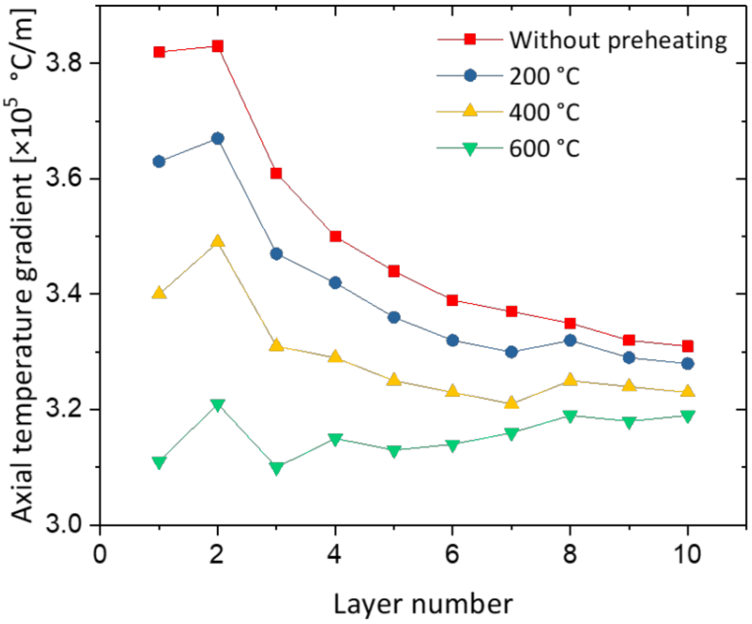

Figure 5.1: Graph showing the effect of a pre-heating step before WAAM deposition of low alloy steel $H_{08}Mn_2S$. Temperature gradient plotted against deposition layer number. Obtained from [120].

5.3 Microstructure

5.3.1 Solidification behaviour in WAAM thin wall

In this section, the microstructure of the WAAM thin wall will be evaluated and discussed in detail.

From the anodized WAAM thin wall structure shown in Figure 4.7, a clear transition region between the AA5183TiC-CG welding wire and the AA5183-CG welding wire appears to have formed. It is evident that the TiC nanoparticles contribute to a significant grain refinement effect in the AA5183TiC-CG section of the WAAM thin wall. This effect is highlighted by comparison of the three-dimensional microstructure cubes in Figure 4.10. As seen from the microstructure cubes, the grain size is reduced from a average grain size of $64 \pm 7\,\mu\mathrm{m}$ to $9 \pm 2\,\mu\mathrm{m}$.

As seen in Figure 4.7b, columnar grains extends upwards from the fusion zone between two succeeding deposition layers. The length of the columnar grains extends as far as $800\,\mu\mathrm{m}$, due to large temperature gradients within the solidifying metal. Grain growth happens mainly in the same direction as the temperature gradient field within the melt. The AA6082 base plate and previously deposited metal acts as a heat sink for newly deposited metal, pulling the heat through the structure creating temperature gradients.

Welding parameters during the WAAM deposition is believed to play a significant role on the resulting mcirostructure, as the cooling rate within the melt is dependent on both voltage and wire feed speed (WFS) during WAAM. It is believed that cooling rates of several hundred degrees per second occurs during solidification of each individual layer. Low wire feed speed favours low heat input to the material, leading to lower temperature gradients. Lower temperature gradients during solidification decreases the rate of which the solid/liquid (S/L) interface moves, and thus restricts the length of the resulting grains, as shown in Figure 2.22 [94]. Epitaxial growth during solidification, as observed only in the AA5183-CG section without TiC nanoparticle additions is believed to emerge due from a deficiency of nucleation events in the vicinity of the solid/liquid (S/L) interface. A discussion on TiC nanoparticle interaction, and the nucleation events will follow in a separate subsection.

To understand the observed columnar grain structure regions in the WAAM thin wall, a thorough theoretical explanation is given.

The columnar grain growth is related to the temperature gradient (G), growth rate of solid/liquid interface (v) and cooling rate of the melt pool. For a columnar-to-equiaxed growth transition to occur, decreasing G is preferred, combined with increasing v [97]. To promote nucleation of equiaxed grains, supercooled liquid have to exist right ahead of the solid/liquid interface, as explained by StJohn *et al.* [121] and his *Interdependence model.*

The temperature gradient and growth rate of the solid/liquid interface is determined by the amount of constitutional supercooling. The Interdependence model is convenient for estimation of grain size (d_{gs}) from factors concerning solidification and alloy chemistry shown by Equation (5.3.1). The equation can be separated in three terms, as shown in Equation (5.3.2). Factors considered are solute concentration (C_o), solute growth restriction factor (Q), solute diffusion rate (D), solute partition coefficient (k), solute concentration at interface (C_i^*), solid/liquid interface growth rate (v), heterogeneous nucleant spacing (x_{SD}) and the required supercooling to activate nucleation points in the liquid (ΔT_N).

$$d_{gs} = \frac{Dz\Delta T_N}{RQ} + \frac{4.6D}{R} \cdot \frac{C_i^* - C_0}{C_i^*(1-k)} + x_{sd} \tag{5.3.1}$$

$$d_{gs} = x_{CS} + x_{DL} + x_{SD} \tag{5.3.2}$$

The first term x_{CS}, is the grain growth distance required to achieve adequate amount of constitutional supercooling (ΔT_{CS}) required for nucleation of nearby particles ($\Delta T_N \leq \Delta T_{CS}$). The second term x_{DL}, represents the distance of the solute profile from S/L interface to where ΔT_{CS} is sufficient enough for nucleation. The third and last term is the particle spacing (x_{SD}), which is the distance from x_{DL} to a point where ΔT_{CS} becomes larger than ΔT_N and nucleates a particle.

Considering the work of StJohn *et al.* [121], it is arguable that the thermal conditions during deposition of AA5183-CG does not meet the requirements for equiaxed grain growth. Constitutional supercooling occurs once the temperature gradient is below the solute-enriched liquidus temperature lying ahead of the S/L interface. The Interdependence model is illustrated at different time intervals in Figure 5.2, showing epitaxial columnar growth transitioning into equiaxed growth [122].

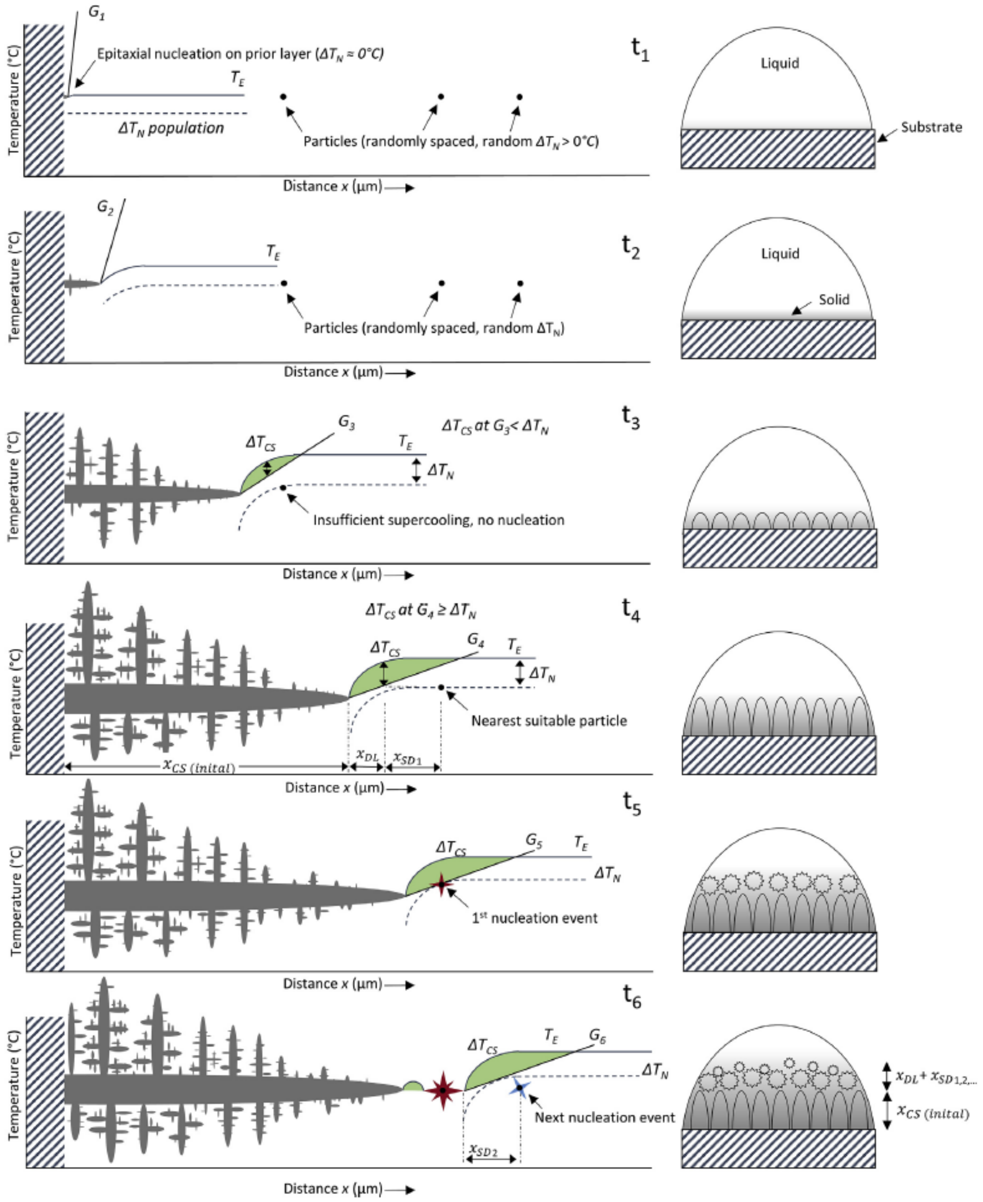

Figure 5.2: The principles of the Interdependence model, illustrating solidification during additive manufacturing at different time intervals. At t_1, growth occurs epitaxially, at a large temperature gradient G_1. Constitutional supercooling has not occurred. Solute segregation happens at t_2, after a small amount of epitaxial growth. The temperature gradient is still too large for constitutional supercooling. At t_3, a small area of constitutionally supercooled liquid exists. ΔT_{CS} could still be insufficient to provide nucleation. When $\Delta T_{CS} \geq \Delta T_N$, nucleation can occur. If there is a lack of suitable particles, as in t_4, columnar growth proceeds by a distance x_{SD} until a acceptable particle is found. At T_5, nucleation on a heterogeneous particle occurs, and the first term of Equation (5.3.1) is decreased to triggering more nucleation events. t_6 illustrates a temperature gradient sustaining continued heterogeneous nucleation, as determined by x_{SD}. Obtained from [122].

5.3.2 Effect of thermal conductivity of nanoparticle during solidification

In this section, the effect of ceramic nanoparticle additions to the aluminium alloy AA5183 will be discussed and evaluated in detail.

In order to achieve the desired strength contribution from introduction of ceramic nanoparticles into the aluminium alloy, it is of great importance that the solidification behavior is seen in context with the nanoparticle interaction during solidification. For optimal strength contribution, an even distribution of nanoparticles throughout the alloy isf desired.

From Figure 4.7 it was observed a significant grain refining effect of TiC nanoparticle addition. Figure 4.7c shows the difference in grain structure between the AA5183-CG section to the lower right, and the AA5183TiC-CG section extending upwards. Closer examination of the AA5183TiC-CG section in SEM, seen in Figure 4.11 showed that TiC nanoparticles was mainly found along the grain boundaries in the alloy. Marbling of the grain boundaries with TiC nanoparticles is unwanted, as it has been reported by several researchers that particle agglomeration along grain boundaries renders the material brittle and less ductile, making the material prone to intergranular fracture [123, 124, 125].

In order to explain why nanoparticles tend to agglomerate at grain boundaries and not reside in the grain interior, the following section discusses mechanisms related to *particle pushing* by the solid/liquid interface.

Several models have been put forward to model and explain the solid/liquid interface interaction with foreign particles in a melt [126]. The models considers the physical interactions of a particle suspended in a melt, and is compromised of several factors. Factors such as surface energy [127], drag force [128], viscosity and thermal effects [129] is considered. The critical conditions for pushing of foreign particles is found by relating the solid/liquid interface velocity to the dendrite tip growth velocity [129].

Fourier's law of heat conduction can be used to calculate the temperature field around a spherical particle, as a function of thermal conductivity ratio between particle and melt. Different thermal conductivities yields different temperature fields, as illustrated in Figure 5.3

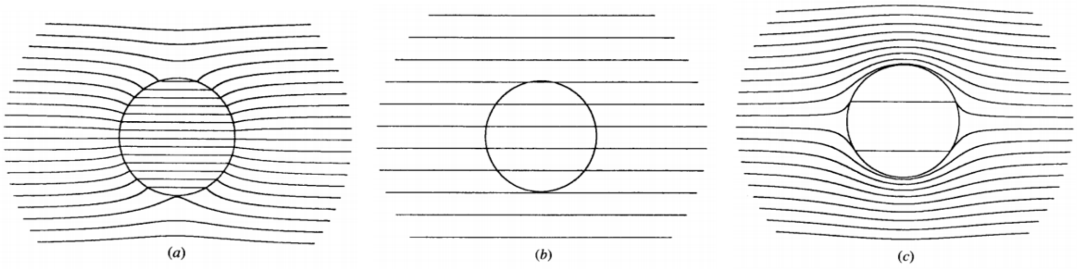

Figure 5.3: (a) isotherms for particle with lower thermal conductivity than the melt, (b) isotherms for particle with equal thermal conductivity as melt, (c) isotherms for particle with higher thermal conductivity than the melt.

If a particle have lower thermal conductivity than then surrounding melt, it will keep its heat longer, as the heat conduction is low within the particle. From Figure 5.3 it can be observed that heat travels faster through the particle having higher thermal conductivity than the melt. The temperature field surrounding the particle will warp the the solid/liquid interface as it approaches, due to the difference in thermal conductivity, as shown in Figure 5.4c.

The warping described in the figure, renders the particle with lower thermal conductivity than the surrounding melt likely to be pushed in front of the solid/liquid interface.

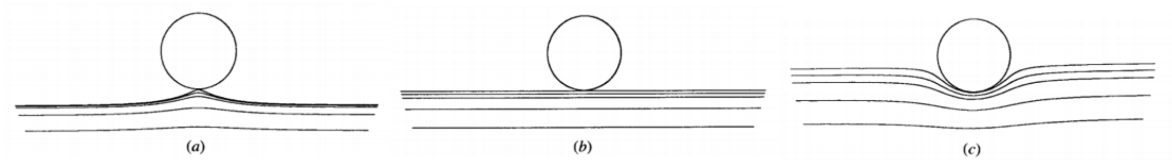

Figure 5.4: The evolution of the solid/liquid interface as it approaches the particle. Each line corresponds to a arbitrary time step during solidification. (a) thermal conductivity of particle lower than the melt, (b) thermal conductivity of particle equal to the melt (c) thermal conductivity higher for particle than the melt.

Shangguan *et al.* [130] found that the interaction between a nanoparticle and the solid/liquid interface can be described by Equation (5.3.3),

$$R_I = \frac{\alpha}{\alpha - 1} R \tag{5.3.3}$$

which relates the interfacial curvature radius, R_I, to the thermal conductivity ratio between the particle and the interface, α. R is the particle radius. When α >1 and R_I >0, a concave solid/liquid interface forms and the particle is likely to be engulfed. When α <1 and R_I <0, a convex solid/liquid interface is formed and particles are likely to be pushed ahead of the interface.

In addition to thermal conductivity, the critical velocity of the solid/liquid interface, V_{cr}, is used to determine if a particle is pushed or engulfed in a more refined fashion, according to Equation (5.3.4) [130, 131]:

$$V_{cr} = \frac{\Delta\gamma_0 \alpha_0^2}{3\eta\alpha R d} \tag{5.3.4}$$

where $\Delta\gamma_0$ = γ_{SV} +γ_{LV} $\cos\Theta$, where Θ is the contact angle, γ_{SV} and γ_{LV} are the interface energies between solid/vapor and liquid/vapor, α_0 is the atomic diameter of the matrix, η is the liquid viscosity, α is the thermal conductivity ratio between the particle and the moving interface, R is particle radius and d is the separation between particle and interface. The critical velocity described above is compared to the dendrite tip growth velocity. The particle is highly likely to be pushed onto the grain boundaries if the dendrite tip growth velocity, V_t, is lower than the critical velocity. Dendrite tip growth velocity is described by the *Lipton-Glicksman-Kurz (LGK) model* according to Equation (5.3.5) [132]:

$$V_t = \frac{DmC_L^*(k-1)}{\pi^2\tau}[Iv^{-1}(\Omega)]^2 \tag{5.3.5}$$

where D is the solute diffusion coefficient in liquid, m is the liquidus slope, C_L^* is the solute concentration in liquid at dendrite tip, k is the equilibrium partition coefficient. Ω =$(C_L^* - C_0)/C_L^*(1-k)$ is the mean total supersaturation and τ =$\sigma/\Delta S_v$ is the Gibbs-Thomson coefficient where σ is the solid–liquid interfacial energy and ΔS is the entropy of fusion per unit volume. $[Iv^{-1}(\Omega)]^2$ is the inverse function of the *Ivantsov function*, and can be approximated according to Equation (5.3.6):

$$[Iv^{-1}(\Omega)]^2] = \Omega \tag{5.3.6}$$

Substitution of Equation (5.3.6) into Equation (5.3.5) gives the approximation shown in Equation (5.3.7):

$$V_t = \frac{DmC_L^*(k-1)}{\pi^2\tau}\Omega^2 \tag{5.3.7}$$

Comparison of V_{cr} and V_t will determine if the nanoparticle is likely to be pushed or engulfed by the grain growth. Engulfment happens if $V_t > V_{cr}$, and is highly dependent on the thermal conductivity of the nanoparticle.

Based on the above theory, it appears that the thermal conductivity of the AA5183 melt in vicinity of the hot TiC nanoparticle is a lot higher than for the nanoparticle itself during cooling. It is fair to assume that the dendrite tip growth velocity has been less than the critical velocity of the solid/liquid interface during solidification in present work on AA5183TiC-CG, as illustrated in Figure 5.5.

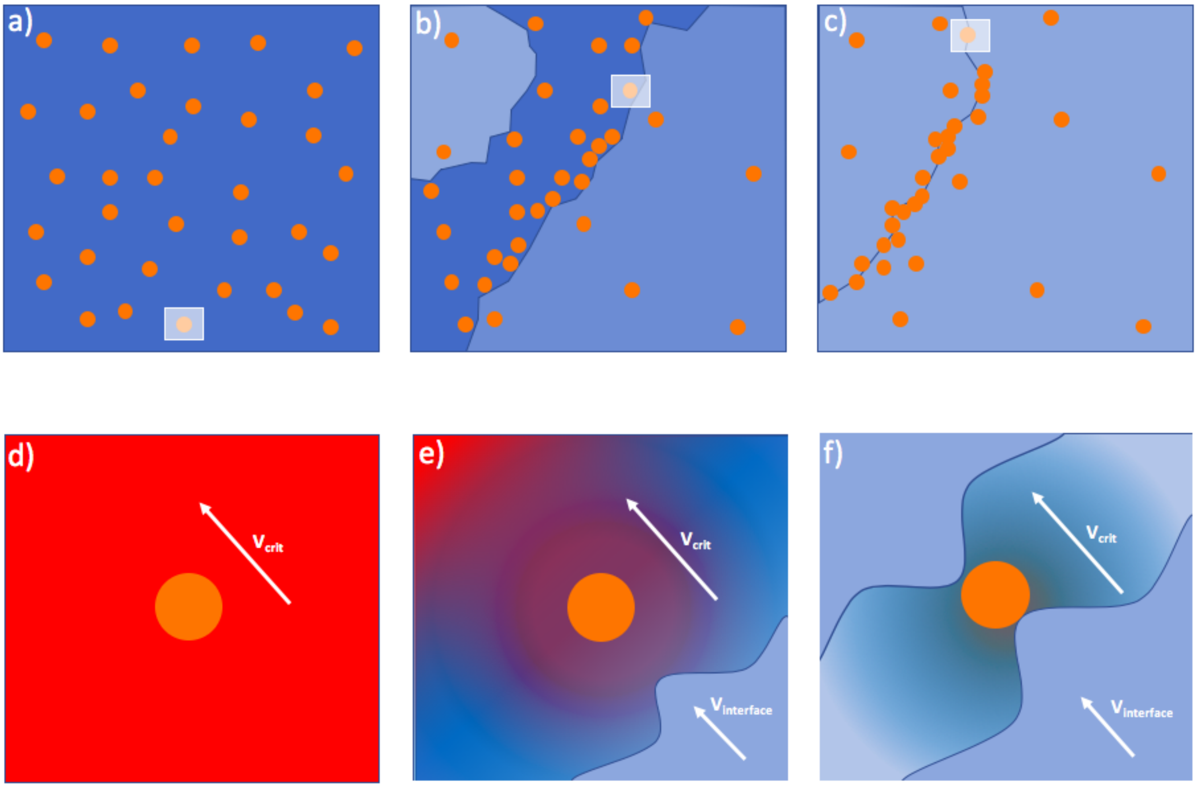

Figure 5.5: Schematic illustration of nanoparticle behavior during solidification. (a) Nanoparticles are evenly distributed in the melt. (b) Some of the nanopartciles act as nucleation points for grain growth. Nanoarticles with low thermal conductivity is pushed by the solid/liquid interface, and (c) trapped at the grain boundaries. The white boxes are magnified in the pictograms underneath, explaining the microscopic behaviour of the solid/liquid interface in relation to the temperature gradient, critical velocity of the dendrite tip growth (V_{crit}) and solid/liquid interface growth velocity ($V_{interface}$).

As seen from the illustration, TiC nanoparticles will most likely be pushed towards the grain boundary, as the surface energy between the particle and the solid/liquid interface is too strong for engulfment to take place. The lower thermal conductivity of TiC compared to molten aluminium is having a profound effect on the solidification behavior in melt, due to TiC conducting its heat slower and retaining heat longer than the surrounding melt. The scattered hot particles in the melt will keep the surroundings liquid, until the surroundings conducts away all the heat residing within the particle, effectively inhibiting particle engulfment. From Equation (5.3.4) it can be deducted that the critical velocity necessary for engulfment increases with particle diameter, as well as with large difference in thermal conductivity between particle and the surrounding melt. Addition of nanoparticles with low thermal conductivity, such as TiC therefore increases the likelihood of finding particles at the grain boundaries. For increased probability for engulfment of nanoparticles, the velocity of the dendrite tip growth should be larger than the critical velocity of the solid/liquid interface, as illustrated in Figure 5.6. This criterion is satisfied by using dense and thermal conductive nanoparticles.

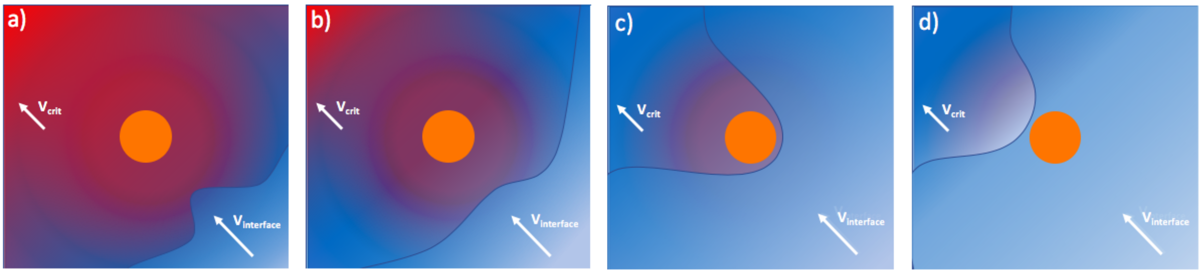

Figure 5.6: Schematic illustration of solidification behaviour and engulfment of nanoparticle in metal melt. (a) nanoparticle has low thermal conductivity, heating up the surrounding melt. (b) solid/liquid interface extracts heat from particle. (c) solid/liquid interface bends around particle, as particle continues to cool down. (d) The particle is engulfed in the grain, due to a higher velocity of the solid/liquid interface ($V_{interface}$) than the critical dendrite tip growth velocity (V_{crit}).

For further development of aluminium matrix composites, the discussed effects from this section should be considered. Li *et al.* [125] reported that TiN nanoparticles acts as a nucleus of heterogeneous nucleation, and then the already nucleated grain surface pushes other ceramic nanoparticles to the grain boundaries. Agaliotis *et al.* [133] found that manipulating the shape of the interface and its curvature, it is possible to control the interaction between the particle and the interface, promoting engulfment of particles. Boostani *et al.* [123] achieved particle engulfment by using high thermal conductive graphene sheets encapsulating SiC particles. A valuable development for future models describing the tendency of particle engulfment/pushing due to thermal conductivity differences may be to account for the inherent heat content of the particle due to particle size.

It was demonstrated in present work discussed in this section, that TiC nanoparticles ($50\,\mathrm{nm}$) does not meet the laid out criteria for particle engulfment, thus making it difficult to achieve even distribution of the particles within the AA5183 alloy. This is likely to have a negative impact on the mechanical properties. Other particles for use in aluminium matrix composites should be explored, and will be discussed in a subsequent section.

5.3.3 Nanoparticle inhibition of grain growth

In this section, the effect of nanoparticle inhibition of grain growth during solidification in a WAAM thin wall will be discussed.

Usually, the desired effect of TiC nanoparticle additions to aluminium alloys is grain refining by increasing the available nucleation events available during solidification. Another effect of the TiC nanoparticles is the inhibition of further grain growth. As nucleated α-Al nuclei grows, nanoparticles will be pushed in front of the solid/liquid interface, as indicated in Figure 4.11, which is described in the previous subsection. The build-up of nanoparticles will form av layer around the growing grain, impeding transport of solute atoms onto the growing interface, as illustrated by Figure 5.7.

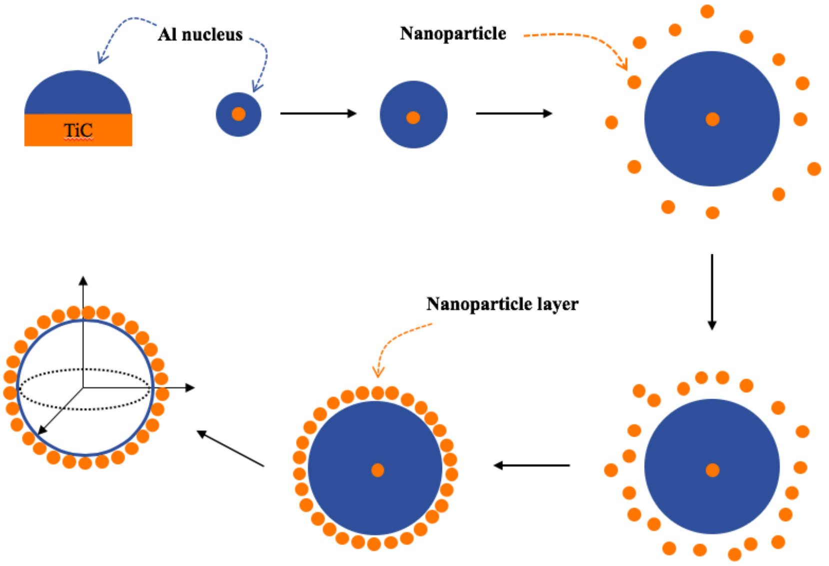

Figure 5.7: Schematic illustration of inhibition of grain growth by TiC nanoparticles. α-Al phase nucleates at TiC nanoparticles, growing equiaxially with an increasing build-up of nanoparticles at the growing interface. The nanoparticle layer will eventually restrict diffusion and inhibit further grain growth.

Wang *et al.* [134] proposed a model describing nanoparticle inhibition of grain growth, demonstrating new fundamental insight to the grain refinement mechanisms during solidification of melts with nanoparticle additions. The diffusion-hindrance increases with increasing fraction of nanoparticles, although the model may break down for very high cooling rates, such as observed during WAAM of AA5183TiC-CG, due to the local variations of solutal supersaturation in the weld pool. These variations may lead to engulfment of a fraction of the large nanoparticles or clusters, while still pushing smaller particles in front of the solid/liquid interface, slowing the growth of the grain.

Greer [135] considers the extent of particle accumulation by pushing, and suggests using a spherical model for crystallite growth to estimate the diameter achieved. Assuming that all nanoparticles in the spherical volume is pushed in front of the solid/liquid interface, the particle number is according to Equation (5.3.8):

$$N_p = V_f \frac{\Delta^3}{d^3} \tag{5.3.8}$$

where V_f is the particle fraction, Δ is the crystallite diameter and d the particle diameter. By assuming $d << \Delta$, and that the particles forms a close-packed array, the needed particle number for complete coating is according to Equation (5.3.9):

$$N_p = \frac{2\pi\Delta^2}{\sqrt{3}d^2} \tag{5.3.9}$$

Setting Equation (5.3.8) and Equation (5.3.9) equal one another, an expression for the crystallite diameter is obtained, as shown in Equation (5.3.10):

$$\Delta = \frac{2\pi d}{\sqrt{3}V_f} \tag{5.3.10}$$

When the crystallite is completely covered in a monolayer of nanoparticles, assuming V_f = 0.03 and d = 50 nm, the above equation yields a crystallite diameter of $6\,\mu\mathrm{m}$. The observed average grain size of AA5183TiC-CG was estimated to $9\,\mu\mathrm{m}$. The true growth exceeds this simplistic model, and indicates that several layers of nanoparticles is built up in front of the solid/liquid interface during solidification. The gradual buildup of TiC nanoparticles, as well as alloying element magnesium, will eventually inhibit the grain growth.

Despite the fact that grain refinement may occur due to particle pushing, it may potentially deteriorate the mechanical properties of the material, as the TiC-marbled grain boundaries could become brittle and less ductile.

5.3.4 Intermetallic Al_3Ti phase

In this section, observation and formation of intermetallic Al_3Ti phase will be discussed.

Observations by secondary electron imaging showed that TiC nanoparticle-rich regions were found at grain boundaries, as indicated by observations from Figure 4.11. Titanium was not only found in the form of nanoparticle clusters, but also as part of intermetallic phases. From EDS mapping in Figure 4.15 and Figure 4.16 it was indicated that Al_3Ti forms at or close to the grain boundaries in the AA5183TiC-section of WAAM thin wall. The crystal structure was observed to be highly ordered.

Kennedy *et al.* [5] reported that the aluminium matrix reacts with TiC particles at elevated temperatures, such that is reached during WAAM in present work. The suggested reaction is given in Equation (5.3.11):

$$13\mathrm{Al} + 3\mathrm{TiC} \rightarrow 3\mathrm{Al_3Ti} + \mathrm{Al_4C_3} \tag{5.3.11}$$

The instability of TiC nanoparticles in aluminium melt results in progressive decomposition of TiC, suggesting increased amount of intermetallic phases in the solidified alloy [136]. The assumption of an equal amount of Ti-atoms and C-atoms in the TiC crystal structure, yields approximately 4:1 weight fraction ratio of Ti-atoms compared to C-atoms. A 3 wt% addition of TiC nanoparticles is indicated by the blue box in the suggested isothermal (700 °C) section of the Al-Ti-C phase diagram proposed by Vandyyoussefi *et al.* [136], shown in Figure 5.8.

Ragnvaldsen [12] reported some issues related to TiC nanoparticle introduction during MCSE, discussing the probability for lower weight fraction of TiC nanoparticles than intended. A result of a lower proportion of TiC nanoparticles in the Al-matrix may be a offset in the suggested phase diagram, moving the blue box further left in the diagram. An important detail to keep in mind is that present work was done at rapid solidification. As TiC reacts slowly to form Al_4C_3, it is reasonable to expect a higher proportion of Al_3Ti compared to Al_4C_3 in the material at rapid solidification rates, such as during WAAM [5]. No observations of Al_4C_3 carbide phase were made in present work. The non-observation of Al_4C_3 may be explained by its dissolution according to the hydrolyzing reaction shown in Equation (5.3.12) [137]. The Al_4C_3 carbide phase may be dissolved during sample preparation, due to washing of samples in water.

$$\mathrm{Al_4C_3}(s) + 12\,\mathrm{H_2O}(l) = 4\,\mathrm{Al(OH)_3} + 3\,\mathrm{CH_4}(g) \tag{5.3.12}$$

Although TiC appears to partly decompose during WAAM, Al_3Ti is reported to contribute significantly increase stiffness and creep strength of aluminium alloys through load sharing effect between the aluminium matrix and the Al_3Ti phase [138]. The high melting point of 1350°C and relatively low density of $3.3\,\mathrm{gcm^{-3}}$ renders the Al_3Ti phase very attractive compared to other intermetallic phases [139]. Zhang *et al.* [140] reported excellent atomic matching between Al_3Ti and the aluminium matrix according to the *edge-to-edge* model, identifying that Al_3Ti is the best grain refiner for aluminium alloys if compared to more conventional TiC, TiB_2 and AlB_2 grain refiners. *In-situ* formation of Al_3Ti could potentially contribute to enhancement of properties in the AA5183TiC-CG section of the WAAM wall. Further studies are required to explore this effect.

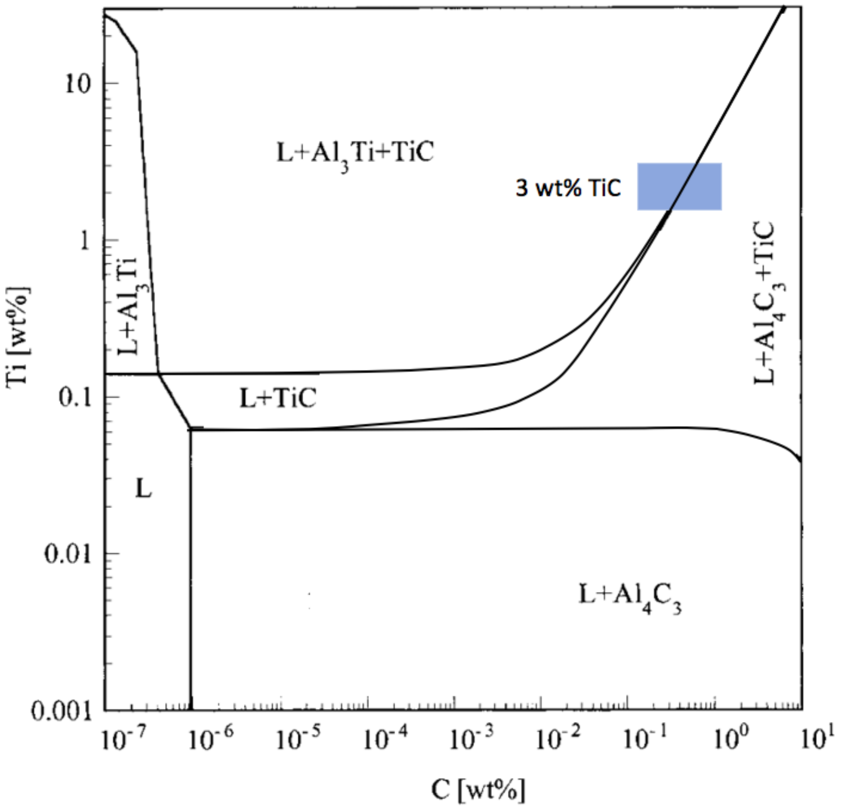

Figure 5.8: Isothermal (700 °C) section of the Al-Ti-C phase diagram, where weight fractions (wt%) of titanium and carbon are indicated on the axes. The blue box indicates phases at approximately 3 wt% addition of TiC nanoparticles to the aluminium matrix. Modified diagram, originally proposed by Vandyyoussefi *et al.* [136].

5.4 Porosity

In this section, characterization of porosity in the WAAM thin wall will be evaluated and discussed in detail.

The extreme porosity in the AA5183TiC-CG section of the WAAM thin wall differs greatly from the observed porosity in the AA5183-CG section, as shown in Figure 4.17. Comparing commercially supplied AA5183 welding wire with extruded AA5183-CG and AA5183TiC-CG welding wires, it can be observed that porosity differs greatly, as shown in Figure 5.9.

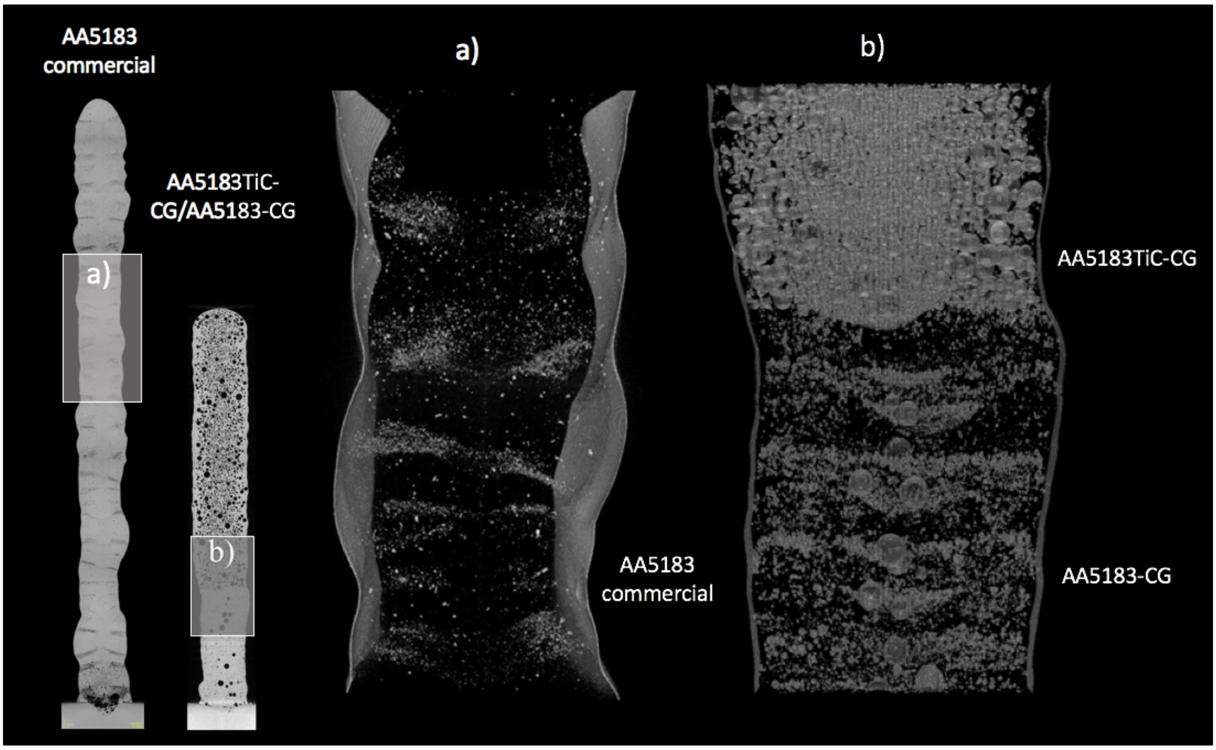

Figure 5.9: Two and three-dimensional mapping of porosity in an (a) commercial AA5183 WAAM thin wall and (b) MCSE AA5183TiC-CG/AA5183-CG WAAM thin wall obtained through *Micro X-ray computational tomography* (micro-CT). Commercial AA5183 WAAM thin wall micro-CT obtained and adapted from [18].

For the commercial AA5183 WAAM thin wall, porosity was observed mainly between each deposited layer. The layer-wise accumulation of porosity is believed to originate from flotation of pores during deposition and surface contamination [18]. The AA5183-CG WAAM thin wall section in present work showed layer-wise porosity consistent with observations from the AA5183 commercial welding wire WAAM thin wall. It appears that extruded welding wires contain larger amounts of gas, forming spherical pores. The AA5183TiC-CG section appears to contain mainly large spherical pores evenly distributed in the whole section.

In order to address and explain the observed porosity, several possible contributors to pore formation will be explored in this section,

5.4.1 Oxides

Formation of surface oxides on aluminium alloys are known to deteriorate properties of several as-manufactured Al-Mg alloys [33]. Manufacturing of WAAM welding wires through MCSE demands that the feedstock material is properly sized and cleaned prior to compaction in the extruder. The feedstock shavings/granules possess a fairly large surface area exposed to the ambient atmosphere. It is assumed that a significant amount of oxides are introduced to the material already prior to MCSE.

As the feedstock material enters the screw extruder, temperatures reach upwards of 500 °C. This gradual temperature increase as feedstock material is transported through the screw channel leads to rapid oxide formation on the granule surfaces. Magnesium as an alloying element is known to contribute to increased hydrogen adsorption in Al-Mg alloys, due to the high diffusion constant of magnesium and the affinity for hydrogen at the surface, in which MgO will adsorb hydrogen molecules from the ambient atmosphere. The surface coverage of MgO is shown to increase with increasing magnesium content in the alloy [33]. The reader is encouraged to revisit the discussion in Section 5.1.1, for the heat-treated MCSE extrudate from screw extrusion work by Ragnvaldsen [12], shown in Figure 4.1.

Application of CO_2 cover gas during screw extrusion appears to have had great effect, reducing oxide formation in the extrudate. The AA5183 aluminum alloy used for WAAM in the present work was produced with CO_2 cover gas during screw extrusion and had visible cracking after heat treatment, far more than AA5183TiC-CG with CO_2 cover gas. Thus, it is an interesting observation that the AA5183TiC-CG section in the WAAM thin wall shows greater porosity than AA5183 without TiC nanoparticles, as the bifilm theory suggests increased porosity content from oxide formation during manufacturing. Considering the almost perfect spherical shape of pores above $20\,\mu m$ in the WAAM thin wall, shown in Figure 4.19 and Figure 4.17, it may be argued that porosity occurs due to several mechanisms in the WAAM thin wall. As shown inFigure 4.23 and Figure 4.24, small irregular pores are squeezed in between grains, while the larger spherical pores span several grains, up to hundreds of grains for the largest pores. The resolution of the CT scanner limits the lower visible pore diameter to 20 μm, and thus will not be able to detect the small irregular pores in the WAAM thin wall.

An alternative explanation of porosity from oxide formation is put forward by Campbell [141] in the *bifilm theory*, arguing that oxides are closely related to hydrogen porosity in all aluminium alloys. The bifilm theory suggests that surface oxide layers in the melt are entrained during production, meaning that the surface film of the metal folds and mutually collides. The surface of the two films touches dry-to-dry, resulting in an unbonded interface of two ceramic oxides as illustrated in Figure 5.10. The surface oxide films has a thickness of only few tens of nanometers, making observations difficult.

A quality index for aluminium alloy castings named *bifilm index* is proposed, summing total length of bifilms measured over cross sectional area. Total number of pores in an cast aluminium alloy was shown to correlate with the bifilm index. The proposed explanation for this correlation, is hydrogen diffusion into the double oxide layer, ballooning the internal volume, as the illustration in Figure 5.10 shows. As there is no interfacial energy between the colliding oxide layers, hydrogen is believed to diffuse rather effortlessly into the entrained double oxide layer, forming a pore [141].

Formation of bifilm may occur during several processing steps as formation occurs due to turbulence in the melt. Whether bifilm is formed during screw extrusion is unknown, but surface oxides are most likely to be mixed into the extrudate during screw extrusion, causing

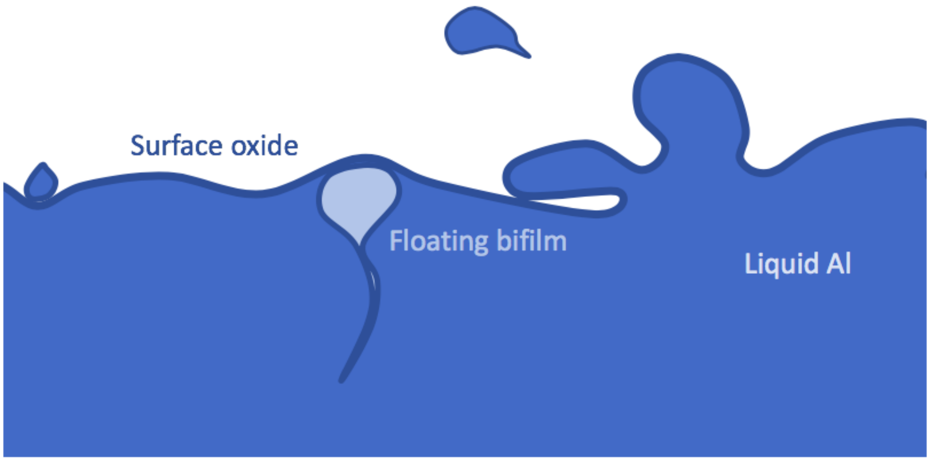

Figure 5.10: Illustration of double oxide film entrainment due to turbulence of the molten aluminium. Hydrogen can diffuse into the double oxide layer, causing flotation of the film.

the oxide content in the extrudate to increase, as new surface oxide is formed on the as-extruded material. Drawing of screw extruded extrudate with a diameter of 10 mm down to 1.2 mm will lower the cross-sectional area of the wire. Lower cross-sectional area will naturally result in a larger fraction of surface oxide per unit volume of wire. In particular, WAAM of aluminum alloys will prove to be very problematic as welding introduces great turbulence in the melt pool. The temperature during WAAM will not reach the melting temperatures of the oxides, as these are many thousands of degrees. Hence the bifilm theory indicates further oxide formation during WAAM, as the turbulence from the welding torch will constantly form new oxides by bringing new melt to the surface, thus experiencing contact with air and then being mixed into the material which then solidifies.

Observation of the surface oxides at the interior of pores, as shown in Figure 4.22, indicated a large presence of oxides on the pore surface. Several hexagonal oxides were observed. EDS mapping suggests that these oxides are MgO and $MgAl_2O_4$. It is believed that magnesium is evaporated during WAAM, as magnesium exhibits a boiling point at 1090 ° [27]. The evaporated magnesium is assumed to be trapped along with hydrogen forming pores during the rapid solidification process, as reported by Katayama *et al.* [142]. Mg enrichment is thus expected on the internal pore surface, and the observation of magnesium-rich oxides should be expected, as confirmed by present work.

Although the surface oxides may contribute to increased hydrogen content in the screw extruded wires, as well as the WAAM thin wall, it is believed that the effect of this contribution is too small to explain the extreme porosity seen in the WAAM section from the AA5183-TiC wire. If the surface oxides were to be a major contributor to the porosity of the material, it would be logical to expect a larger pore content in the AA5183-CG section as well. Therefore, it is assumed that the root cause for porosity is more likely to originate from other contributions.

5.4.2 TiC nanoparticles

It is of interest to investigate the porosity contribution from the introduction of TiC nanoparticles, as it is the sole difference between the AA5183-CG and AA5183TiC-CG welding wires used for deposition of the WAAM thin wall in present work.

The physical nature of nanoparticles present them with large surface areas, that could form network-like structures when agglomerated. Such structures and the nanoparticles themselves, could easily trap the ambient atmosphere and adsorb hydrogen onto its surfaces. The agglomerated particles could be said to function as a sponge, storing relatively large amounts of ambient air and adsorbed hydrogen.

As the TiC nanoparticle coating of AA5183 was carried out in advance of screw extrusion, it is reasonable to assumed that the hydrogen content of the two feedstock granules differed already prior to MCSE. A network-like structure of TiC nanoparticles could potentially have formed on the surface of the AA5183 granules. Zhao *et al.* [143] found that metallocarbohedrene Ti_8C_{12} and nanocrystal $Ti_{14}C_{13}$ showed hydrogen storage capacity at ambient temperature of 6.6 wt% and 7.7 wt%, respectively. An illustration of the TiC nanoparticles with bonded hydrogen is shown in Figure 5.11.

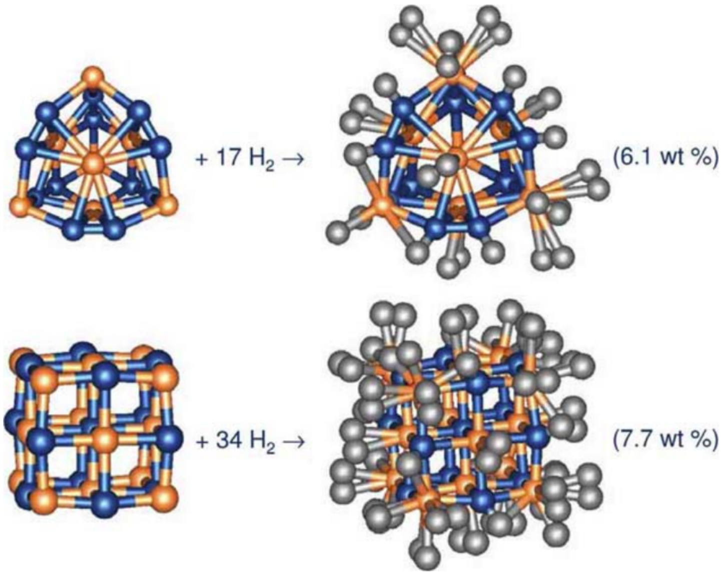

Figure 5.11: Illustration of hydrogen storage capacity of titanium carbide particles at ambient temperature. The upper particle is metallocarbohedrene Ti_8C_{12} and the lower particle is nanocrystal $Ti_{14}C_{13}$. Obtained from [143].

Metal hydrides that form as hydrogen adsorbs are typically reported to have hydrogen release temperatures in the range 250-400 °C, varying with material specific thermodynamics [144]. A obvious challenge in the present production method using MCSE, will then be the elevated temperatures during screw extrusion of the TiC nanoparticle coated AA5183 aluminium alloy. Assuming a hydrogen release temperature in the vicinity of other known metal hydrides, it is believed that molecular hydrogen could be released in the front screw channel, as well as in the extrusion chamber during manufacturing. The different locations are illustrated in Figure 5.12. Temperature during screw extrusion was measured by Ragnvaldsen [12] in his preliminary work on AA5183TiC-CG and is presented in Figure 5.13, showing temperatures measured by thermocouple sensors.

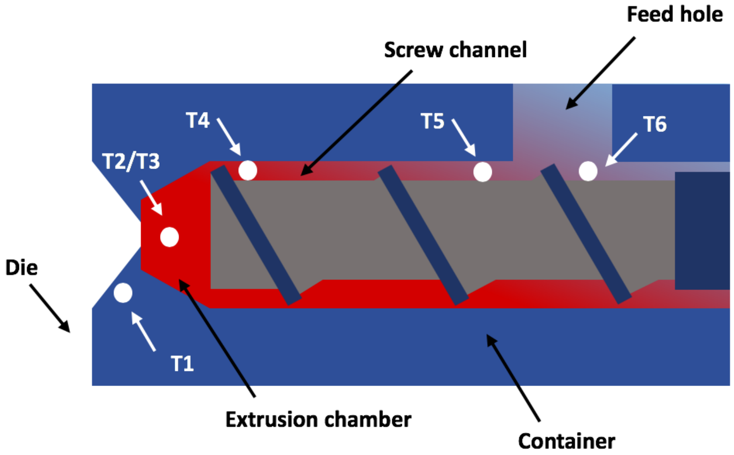

Figure 5.12: Cross-sectional illustration of the screw extrusion interior, with thermocouple locations indicated by white circles. The color gradient indicate the gradual increase in temperature along the screw.

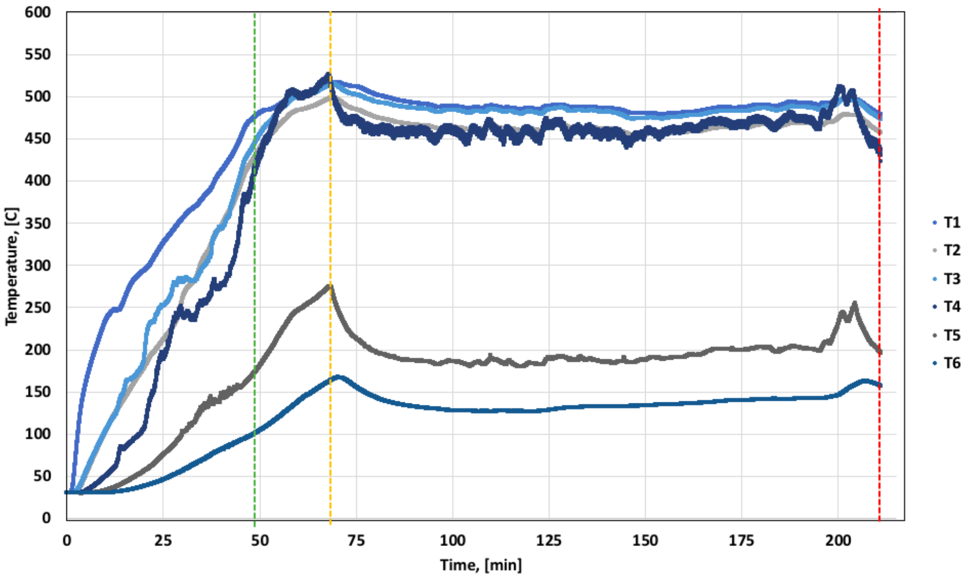

Figure 5.13: Temperature through screw extrusion of AA5183TiC-CG with CO_2 cover gas. Dashed green line indicates extrusion start, orange dashed line indicates air-cooling start and red dashed line indicates screw extrusion stop. Position of temperature measurements are: T1 (die), T2/T3 (left/right side extrusion chamber), T4 (front screw channel), T5 (back screw channel) and T6 (screw stem). Temperature data was collected by Ragnvaldsen [12] in his preliminary work on processing of AA5183TiC-CG.

Consultation of screw extrusion temperatures in the extrusion chamber (T2/T3), and front screw channel (T4) confirms that release of hydrogen from TiC nanoparticles during screw extrusion could be possible. It is difficult to quantify how much hydrogen is dissolved in the metal. In the extrusion chamber, AA5183TiC-CG will form a solid plug of the feed material under high pressure. Whether hydrogen escapes from the screw channel or is trapped in the metal has not been investigated.

Trapped hydrogen from MCSE could potentially precipitate out during solidification of the WAAM melt pool, as the solubility of hydrogen is approximately 20 times lower for solid aluminium compared to liquid aluminium. TiC nanoparticles is suggested to act as solid interfaces, facilitating precipitation of hydrogen. Evenly distributed particles in the melt will thus increase the probability for pore formation. It is believed that it is the increased number of potential nucleation sites, combined with increased hydrogen content that makes the largest contribution towards AA5183TiC-CG exhibiting a high degree of porosity, compared to the TiC-free AA5183CG section.

5.4.3 WAAM parameters

Careful control of WAAM parameters and feedstock cleaning processes are essential in producing pore-free WAAM components. Identical feedstock material could exhibit widely different properties and characteristics parameters and cleaning inconsistent. This topic will be discussed in this section.

Firstly, a few notes on the importance of cleaning of feedstock wires. Prior to WAAM, the feedstock wires are susceptible to contamination from moisture and hydrocarbons during drawing. Proper cleaning of the wire before WAAM is essential to avoid contamination that will develop gas during deposition. Haboudou *et al.* [145] found through X-ray inspections that surface oxides could contribute to increase in porosity in the WAAM build if not removed pre-production. Polishing and laser cleaning of feedstock wire showed dramatic reduction in porosity due to surface oxide removal, and should be attempted removed in any case. Insufficient surface cleaning of the wires could have a large effect on porosity of the final build, as found by AlShaer *et al.* [146]. Laser cleaning reduced the overall porosity from 10-80% down to under 0.5% In present work, both wires went through the same exact procedure for drawing and cleaning, and it is therefore assumed that the contribution to porosity would be equal, hence not responsible for the excess porosity in AA5183TiC-CG.

Secondly, during WAAM deposition, porosity is mainly caused by gas bubbles induced by hydrogen, due to reduction in hydrogen solubility during solidification, and vaporization of magnesium [147, 148]. Klein and Schnall [149] quantified the change elemental concentrations of AA5183 by comparing welding wire composition to WAAM composition, showing a significant vaporization of elemental magnesium during WAAM, as shown in Figure 5.14.

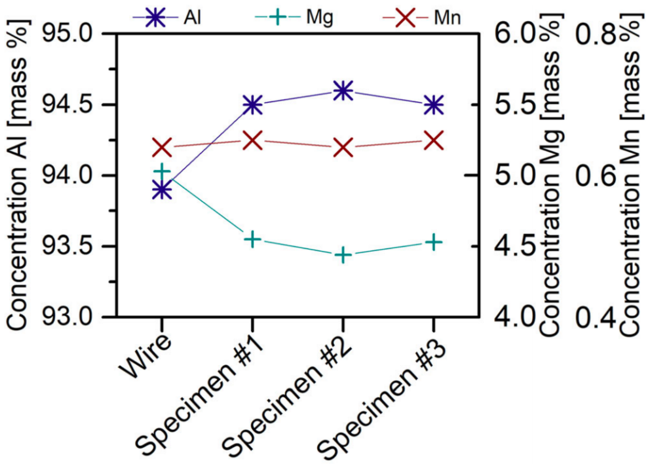

Figure 5.14: Change in elemental concentration of major alloying elements in AA5183 before and after WAAM. Mg is reduced significantly, Mn remains unchanged and Al appears to increase. Specimen 2 was manufactured at highest temperature. Obtained from [149].

The major sources of hydrogen into the WAAM build are humidity in the ambient atmosphere, moisture in the shielding gas, moisture on the wire surface, and inherent hydrogen in the material. Hydrogen does not react with aluminium, and absorb into a interstitial position on the aluminium lattice. Dissolution of hydrogen from the aluminium melt follows *Sieverts' Principle* and *Henry's Principle*, which means that higher hydrogen partial pressure in the atmosphere, combined with higher temperature temperature, leads to higher hydrogen concentration in the molten pool of aluminium alloy [150]. As described in the previous section, pores is believed to nucleate at solid interfaces, such as inclusions or particles. For the AA5183TiC-CG section, a higher number of solid interfaces is present through the evenly distributed TiC nanoparticles in the melt. After precipitation, pores tend to float due to buoyant forces, and get trapped due to the fast solidification of the solid/liquid interface.

The porosity of the as-built WAAM thin wall is controllable to a certain degree, by tailoring processing parameters such as weld method, voltage, travel speed, wait time and wire feed speed. Cong *et al.* [92] found that weld method greatly impacted the porosity of additive manufactured aluminium alloys. Different weld methods results in varying heat input and shape of the melt pool. The advantage of the short-circuiting pulse using cold metal transfer (CMT) is the low heat input, low spatter and high deposition rates achieved. Several extensions of the CMT technology has been proposed, namely CMT-pulse (CMT-P), CMT-advanced (CMT-ADV) and CMT pulse advanced (CMT-PADV). Common for these, are varying arc current and voltage waveforms. The pulse mode is a higher frequency pulse, compared to conventional CMT. Advanced mode adds alternating polarity, which produce a significant oxide cleaning effect [151]. The combination of these modes is applied in CMT-PADV, thus resulting in reduction of hydrogen from the oxide layer, as well as stirring of the melt pool to facilitate gas pore escape [152]. Conventional CMT is found to produce elongated fingershaped melt pools during deposition, causing long distance for pore escape from the melt [92]. Shallow melt pools are advantageous.

Arc voltage and travel speed during deposition is closely related to the heat input to the melt pool. At low travel speeds, heat input will naturally be higher in the melt pool, so that excessive absorption of hydrogen from the ambient atmosphere may be possible. This, together with coarsening of preexisting pores through *Ostwald ripening* due to elevated temperatures, will lead to increased pore content in the material [116]. Although some pores may float to the surface and escape due to slower solidification in the melt pool, it is not assumed that the effect will be significant enough. The vacancy diffusion also increases with temperature, which should be avoided [153]. Satisfactory travel speed , as well as wire feed speed should be sought at initial attempts, before the commencement of full-size component construction. Cong *et al.* [92] found that too low travel speed and wire feed speed resulted in pore formation between deposition layers, as high heat input led to the nucleation of gas pores by particles from dendritic solidification structures.

By using commercially supplied feedstock wire, Fang *et al.* [154] reported an average pore diameter of $33\,\mu\mathrm{m}$ in a AA5183 WAAM thin wall manufactured by CMT. Gu *et al.* [116] reported an average pore diameter of $6\,\mu\mathrm{m}$ of an AA5183 WAAM thin wall manufactured by CMT. When applying 45 kN inter-layer rolling, they reported a decrease in pore diameter to an average of $4\,\mu\mathrm{m}$. Gu *et al.* [116] performed pore scanning at a synchrotron facility, enhancing the spatial resolution of the tomographic imaging to $0.65\,\mu\mathrm{m}$ compared to $10\,\mu\mathrm{m}$ utilized in present work. By utilizing fifteen times better resolution, it is possible to obtain scans for inter-dendritic porosity, which contribute drastically lower average pore size measured in the material.

5.5 Microhardness

In this section, hardness of the WAAM thin wall is evaluated and discussed.

The microhardness measurements were performed only for the AA5183TiC-CG section of the WAAM thin wall. Preliminary work on a AA5183 WAAM thin wall manufactured by commercial welding wire showed a microhardness of 78 ± 6 $HV_{0,1}$, compared to the present 88 ± 5 $HV_{0,1}$ for AA5183TiC-CG [18]. An increase of 13% was thus achieved through incorporation of TiC nanoparticles to the AA5183 aluminium alloy. It is assumed that the substantial grain refinement contributes to increased volume fraction of grain boundaries, as well hardness contribution from local strain fields due to thermal coefficient mismatch between TiC particles and the aluminium matrix. Built-up dislocations close to the TiC particles is believed to increase hardness. Due to the porous nature of the AA5183TiC-CG WAAM thin wall, it is reason the believe that the *true hardness* is higher than the measured hardness, as indentations have a high probability of being affected by nearby weakness in the matrix due to subsurface pores.

The present work found hardness levels exceeding those found by Horgar *et al.* [155], ranging 70-75 $\mathrm{HV}_{0,1}$ in AA5183 WAAM. Gungor *et al.* [156] found hardness levels ranging as high as 80-90 $\mathrm{HV}_{0,1}$ in aluminium alloy AA5083 using CMT.

5.6 Tensile properties

In this section, tensile properties of the WAAM thin wall samples are evaluated and discussed.

Comparison of the parallel (x) and perpendicular (z) tensile tests in Figure 4.25, show a very large difference in strength obtained, up to about 100 MPa. Compared to the strength shown in preliminary work for an AA5183 WAAM thin wall from commercial welding wire, it is evident that the porosity is detrimental to the WAAM thin wall manufactured from MCSE welding wires. Comparison of tensile results with AA5183 WAAM thin wall manufactured by commercial welding wire is shown in Figure 5.15. The low tensile strength achieved in the present work can, with a high degree of certainty, be explained primarily by high porosity in the material. Anisotropy in the microstructure will also be part of the explanation, although to a much lesser extent.

Tensile sample (x1) represents an outlier, as a large pore in the middle of the sample led to early fracture. The lower relative strength of longitudinal tests (y) could mainly be explained by weakness in the interlayer regions in the WAAM thin wall, as the tensile samples spans across multiple layers. As seen from Figure 4.17, high density of pores is found in the interlayer regions, thus it is expected that these weakens the overall strength in the z-direction. When conducting tensile tests in the z-direction, microstructural anisotropy will be devastating to the material. Columnar regions, as shown in Figure 4.7b is thought to weaken the material, as the long parallel grains results in low fraction of grain boundaries hindering slip dislocations. High density of grain boundaries is preferred, and will hinder slip motion into another grain, as the slip planes have different orientation [27].

Tensile tests conducted in the transversal (x) direction shows highest strength, presumably due to sample machining from only a few deposition layers in the WAAM thin wall, which are also longitudinal with the sample direction. The elongation at fracture was found to be highest in the x-direction. The lower elongation z-direction is likely explained by the already described interlayer regions, as well as the columnar grain structure in the AA5183-CG portion of the WAAM thin wall. Compared to commercial AA5183 WAAM thin wall, a harder and more brittle material was expected when TiC nanoparticles were added. The large porosity has probably yielded a lower result for elongation than what would have been the case if the material was fully dense.

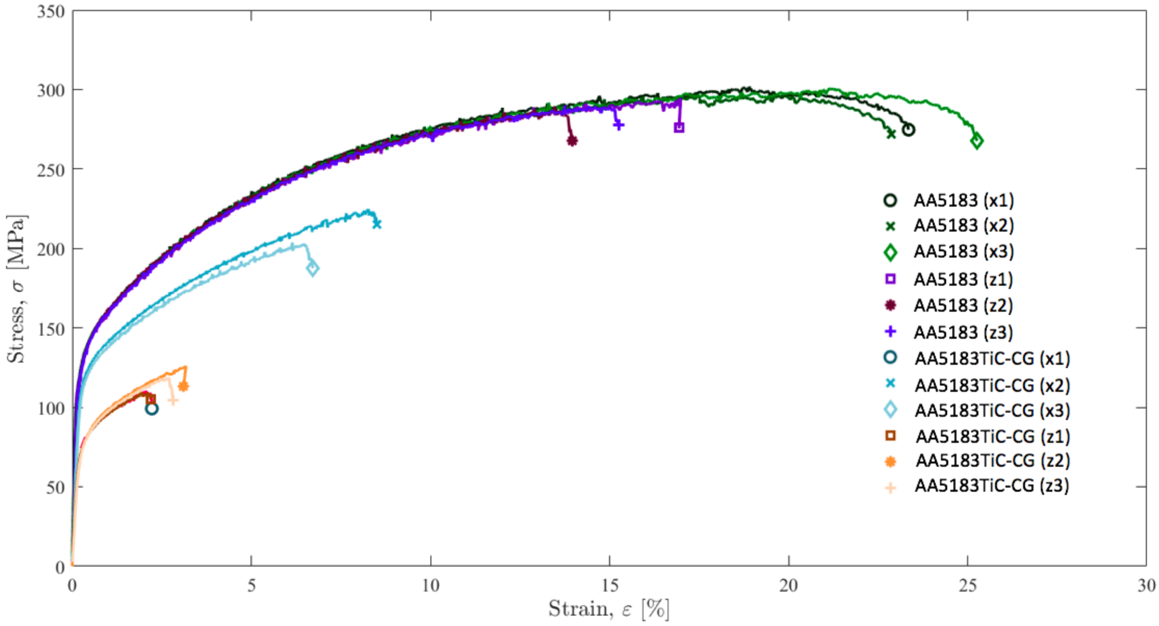

Figure 5.15: Stress-strain curves from tensile tests of cross-sectional WAAM thin wall sample. Tests performed on samples parallel to welding direction is denoted x, and perpendicular samples denoted z. A constant strain rate of $2\,\mathrm{mm\,min^{-1}}$was applied. AA5183 stress-strain curves obtained from [18]

The results of the tensile tests makes it difficult to account for the strength contribution from the addition of the TiC nanoparticles. The largest contributions were expected to come from CTE mismatch, Orowan strengthening, Hall-Petch and elastic modulus mismatch (EM) and will be discussed briefly.

Silva *et al.* [157] demonstrated a novel thermal management technique *near-immersion active cooling* (NIAC) for mitigation of heat accumulation during WAAM by using a cooling liquid for heat dissipation during manufacturing. The novel technique led to lower anisotropy in the WAAM thin wall, with no significant difference in ultimate tensile strength (σ_{UTS}) for the (x) and (z) directions in the thin wall, which is contrary to recent research and present work. The geometrical and mechanical quality may be increased utilizing NIAC for future applications. The proposed technique is illustrated in Figure 5.16.

Thermally induced dislocations are generated during solidification of the melt, due to the considerable difference in thermal expansion coefficients between the aluminium matrix (α_{Al}= $21.4\,\mathrm{\mu m\,mK^{-1}}$) and TiC nanoparticles (α_{TiC}= $7.7\,\mathrm{\mu m\,mK^{-1}}$). The mismatch between thermal expansion coefficients results in plastic strain around the nanoparticles in the composite, increasing dislocation density. The theoretical strengthening contribution from CTE mismatch can be calculated from Equation (2.3.4), yielding a strengthening contribution of 134 MPa for 3 wt% addition of TiC nanoparticles with average particle diameter of $50\,\mathrm{\mu m}$. Assuming a non-uniform dispersion of nanoparticles, it is suggested that the true contribution from CTE mismatch will be less than theoretical calculated contribution for present work, as indications have been found that nanoparticles agglomerates and are pushed to the grain boundaries.

Impenetrable particles in the aluminium matrix, such as TiC will contribute to increased

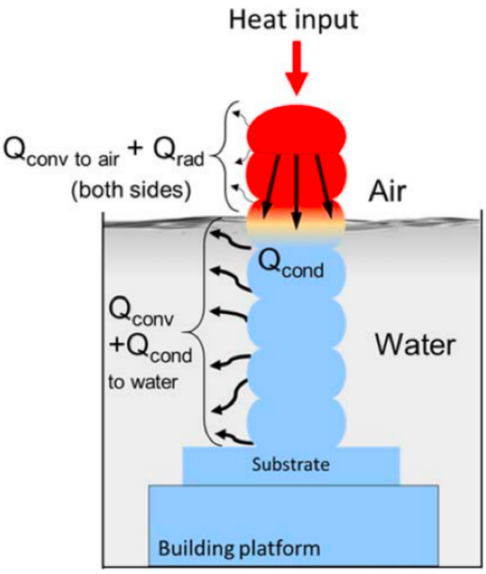

Figure 5.16: Illustration of the novel thermal management technique, near-immersion active cooling (NIAC). Water or other coolant liquids can be used to enhance the heat dissipation from the WAAM component during manufacturing, decreasing building time and enhancing mechanical properties. Obtained from [157].

strength through Orowan strengthening, as dislocations are forced to form *dislocation loops* around the TiC nanoparticles. Theoretical strengthening contribution from Orowan strengthening can be calculated from Equation (2.3.3), yielding a strengthening contribution of 68 MPa for 3 wt% addition of TiC nanoparticles with average particle diameter of $50\,\mu\mathrm{m}$. Insufficient dispersion of TiC nanoparticles during solidification, combined with agglomeration suggests that the true contribution from Orowan strengthening is far lower than the theoretical calculated contribution.

As shown by the three-dimensional microstructure cubes presented in Figure 4.10, TiC nanoparticle addition introduced significant grain reduction for the AA5183TiC-CG section of the WAAM thin wall, suggesting a strengthening contribution from the Hall-Petch relation. By increasing the crystallographic misorientation, dislocation motion is hindered, thus piling up dislocations. The reduction of grain size corresponds to a linear theoretical strengthening contribution of 57 MPa for a grain size of $9\,\mu\mathrm{m}$ for AA5183TiC-CG against 23 MPa for a grain size of $64\,\mu\mathrm{m}$ for AA5183-CG. The grain size reduction in the AA5183TiC-CG section increased the theoretical strengthening contribution by approximately 150. The *Zener pinning* effect of nanoparticles is sometimes used to approximate expected grain size from nanoparticle additions to metal matrix composites [58]. According to Equation (2.3.2), a grain size of $1\,\mu\mathrm{m}$ was expected for 3 wt% addition of TiC nanoparticles with average particle diameter of $50\,\mu\mathrm{m}$. The effect of particle pushing of TiC nanoparticles to the grain boundaries will likely distort the calculation of grain size from Zener pinning. The effect of particle accumulation during solidification was discussed in subsection 5.2.4, where calculations yielded a expected grain size of $6\,\mu\mathrm{m}$. It is assumed that agglomeration of TiC nanoparticles during solidification reduces the effect of zener pinning, may explaining the larger grain size observed. The elastic modulus mismatch for 3 wt% addition of TiC nanoparticles with average particle diameter of $50\,\mu\mathrm{m}$ was calculated according to Equation (2.3.6), yielding a strengthening contribution of 40 MPa.

By summing root squares of each strength contribution, it was calculated according to Equation (2.3.7), a total strength contribution of 166 MPa from 3 wt% addition of TiC nanoparticles with average particle diameter of $50\,\mu\mathrm{m}$. Comparison with existing research of unreinforced Al-Mg aluminim alloys presented in Table 5.1 suggests that 3 wt% TiC nanoparticle reinforced AA5183 may theoretically exhibit a ultimate tensile strength in the vicinity of 450 MPa. A grain-refined and pore-free AA5183TiC-CG WAAM thin wall, with a low degree of agglomerated TiC nanoparticles at the grain boundaries, would probably have achieved theoretically calculated strength to a greater extent.

Table 5.1: Comparison of yield strength (σ_Y) and ultimate tensile strength (σ_{UTS}) with previous research on wire arc additive manufactured (WAAM) Al-Mg components.

Alloy	σ_Y **[MPa]**	σ_{UTS} **[MPa]**	**Author**
Al4.5MgMn	96	148	Present work
Al4.5MgMn	125	283	Klein (2020) [149]
Al4.5MgMn	154	296	Flåm (2019) [18]
Al4.5MgMn	-	290	Gu *et al.* (2019) [116]
Al5Mg	128	255	Su *et al.* (2019) [158]
Al4.5MgMn	-	289	Fang *et al.* (2018) [154]
Al4.5MgMn	145	293	Horgar *et al.* (2018) [155]
Al6.4Mg,	124	273	Geng *et al.* (2017) [159]
Al4.5MgMn	146	283	Dutra *et al.* (2015) [160]
Al4.5MgMn	120	-	Babu *et al.* (2012) [161]
Al4.5MgMn	130	275	Standard wrought [27]

5.7 Other ceramic nanoparticles for use in aluminium matrix composites

As present work on TiC nanoparticle addition to AA5183 aluminium alloy has shown, it appears that additional nanoparticles may be investigated in order to achieve the desired properties of the aluminum matrix composite. For the selection of nanoparticles for both grain refinement and strength enhancement, it will be important to take into account factors discussed in this work.

From theoretical considerations discussed in Section 5.3.2, it emerged that it is advantageous to use a nanoparticle with high thermal conductivity. This will favour engulfment of the particle during WAAM solidification, leading to an even distribution throughout the as-built component. Grain refinement potency and strengthening contributors, as briefly discussed in Section 2.4, does not apply in the same way to nanoparticles as micron-sized particles. Nanoparticles will to a greater extent contribute to grain refinement by zener pinning of the solid/liquid interface during solidification, as described in Section 5.3.2 and 5.3.3. According to equations presented in Section 2.4, strengthening contribution from different nanoparticles does not vary much, as only the thermal expansion coefficient is a material specific property.

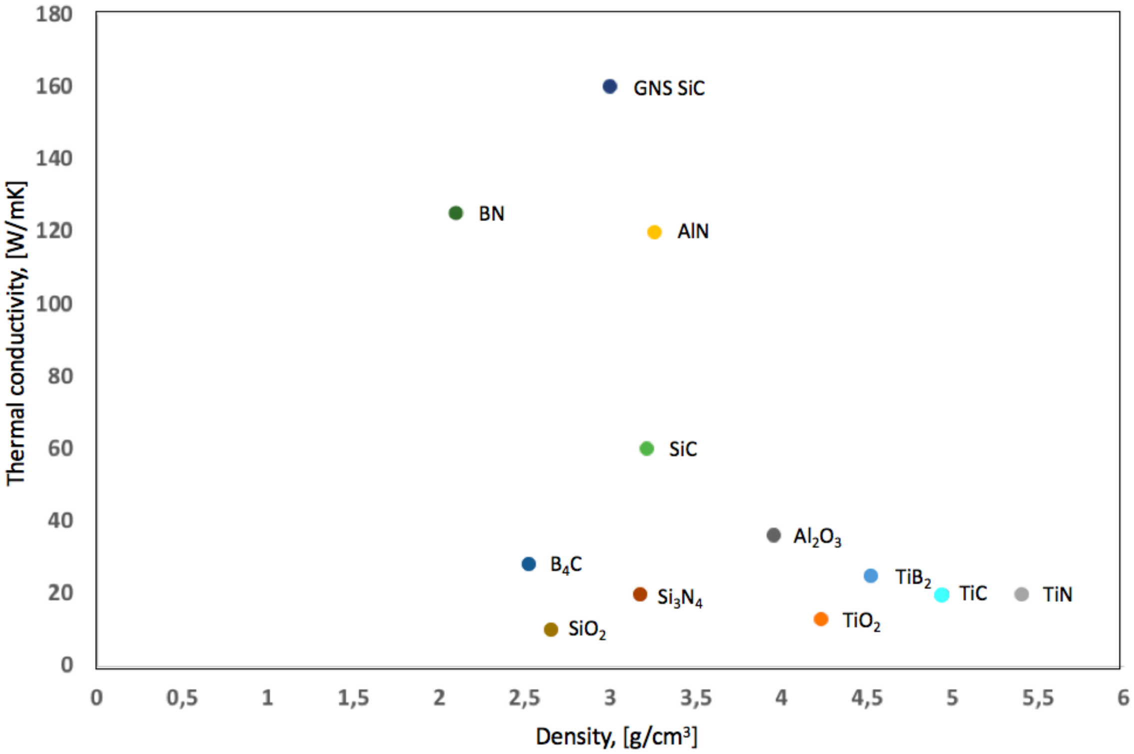

Figure 5.17: Thermal conductivity of different nanoparticles plotted against the particles density.

Reinforcement particles with superior strengthening contribution properties are of no use if pushed against the grain boundaries, hence lowering the ductility and overall strength of the composite. It is of great importance to obtain an even distribution of nanoparticles before strengthening contributions are considered, especially in manufacturing processes with rapid solidification, such as WAAM. Thus, the primary objective should be to find nanoparticles that exhibit high thermal conductivity sufficient for engulfment, with strengthening contributions as secondary objective. A selection of ceramic nanoparticles is presented in Figure 5.17, ranked according to thermal conductivity and density.

Three of the ceramic nanoparticles presented in the figure above stands out, showing superior thermal conductivity combined with low density:

BN: It has been reports confirming that boron nitride shows good mechanical properties in the BN/Al-system [162]. Fujii *et al.* [163] found an equilibrium contact angle as low as 0° at 1000°C, suggesting that BN may be an promising candidate for nanoparticle reinforcement of aluminium. Lee *et al.* [164] investigated tensile properties of an Al-Mg alloy reinforced with BN particles, reporting a 3.5 times decrease in grain size, in addition to a significant increase of 118 MPa in ultimate tensile strength. Partly due to *in-situ* formation of AlN.

GNS SiC: Graphene nanosheet encapsulated SiC nanoparticles is believed to exploit the superior thermal conductivity of single sheet sp^2 hybridized carbon atoms, allowing SiC nanoparticles to be engulfed in the grain interior rather than agglomerating at grain boundaries. Boostani *et al.* [123] proposed and investigated a innovative processing route for incorporation of GNS SiC into a aluminium matrix, showing superior enhancement of yield strength and tensile elongation of composites by 350% and 258%, respectively, compared to a unreinforced A357 aluminium alloy.

AlN: AlN is inert to aluminium, causing no reactions during processing, although instability is reported towards oxygen and magnesium. Wang *et al.* [165] fabricated AlN particle composites by powder metallurgy, using pure aluminium. Although issues due to oxidation of the aluminium powder during manufacturing were reported, ultimate tensile strength was found 4.5 times higher for the composite compared to commercially pure aluminium alloy.

Chapter 6

Conclusion

In this thesis, wire arc additive manufacturing (WAAM) was performed using two different metal continuous screw extruded (MCSE) wires, with and without TiC nanoparticle additions to a AA5183 aluminium alloy. The main focus was characterization and testing of the AA5183TiC-CG aluminium matrix composite (AMC) section of the WAAM thin wall. This section summarizes the key findings in this thesis.

- Metal continuous screw extruded (MSCE) welding wires were used as feedstock material for deposition of a thin wall manufactured by wire arc additive manufacturing (WAAM) using cold metal transfer (CMT) weld mode.
- Heat-treatment of MCSE extrudate 10 mm profiles revealed circular cracking in the transversal cross-section, as well as cracking along the longitudinal direction for the AA5183-CG extrudate without TiC nanoparticle additions. It is believed that hydrogen release during heat treatment expands already existing micro-cavities in the material, suggesting a hydrogen-rich extrudate. AA5183TiC-CG extrudate showed no signs of cracking. Heat-treatment of drawn and shaved 1.2 mm welding wires showed minor porosity for the AA5183TiC-CG welding wire. It is believed that TiC nanoparticle coating of the feedstock before MCSE introduces unwanted hydrogen residing at interstitial sites in the metal.
- Investigation of both WAAM thin wall sections revealed highly different microstructure. The TiC nanoparticles led to a equiaxed grain structure with 86% decrease in grain size, a significant grain refining effect. Successfully inhibiting formation columnar grain structure. The AA5183-CG section had sections of columnar grain growth, explained by large temperature gradients in the thin wall during deposition, inhibiting columnar to equiaxed growth transitioning.
- Observations by scanning electron microscopy (SEM) revealed that TiC nanoparticles mainly resided at grain boundaries. The low thermal conductivity of the TiC nanoparticles is suggested to alter the solidification behaviour of the aluminum melt, in which the solid/liquid interface facilitates particle pushing instead of particle engulfment. Particle pushing is suggested to inhibit grain growth, thus contributing further to grain refinement. TiC nanoparticles ($50\,\mathrm{nm}$) was found to not meet criteria for engulfment, thus making it difficult to achieve an even particle distribution.

- Intermetallic Al_3Ti phase was observed to form *in-situ* at grain boundaries using elemental EDS point mapping. It is suggested that elevated temperatures during wire arc additive manufacturing (WAAM) facilitated the reaction between TiC nanoparticles and the aluminium matrix to form Al_3Ti.
- Porosity examination of the AA5183TiC-CG section of the WAAM thin wall revealed 25 vol% porosity. The extreme porosity is suggested to originate from several possible contributors, such as surface oxides, hydrogen storage capacity of TiC nanoparticles, MCSE processing and WAAM parameters.
- The mechanical properties of the WAAM thin wall was found to be inferior to previous research. Mainly because of skewed properties due to extreme porosity in the WAAM thin wall. It is assumed that a pore-free material would exhibit a ultimate tensile strength in the vicinity of 450 MPa, based on theoretical strengthening contributions from 3 wt% TiC nanoparticle addition.
- For further improvement of nanoparticle strengthened aluminium matrix composites, nanoparticles with high thermal conductivity should be explored in order to achieve an even distribution of nanoparticles, thus increases strength and isotropic mechanical properties in the manufactured material.

Chapter 7

Further work

For large-scale production of additive manufactured aluminium alloy components, wire arc additive manufacturing (WAAM) is superior. Advantages such as high raw material utilization and environmentally friendly production is promising. For production of aluminium matrix composites (AMCs) through metal continuous screw extrusion (MCSE) and wire arc additive manufacturing (WAAM), some challenges still remains to be solved before commercialisation of the production technology. Suggestions for further work are presented as follows:

- Investigations of processing parameters during MCSE in order to minimize pore formation of MCSE extrudate profiles. It is believed that the feedstock material and the air cooling system may introduce unwanted hydrogen to the extruder chamber.
- Investigations into nanoparticle coating procedures, and whether nanoparticle introduction to feedstock aluminium alloy contribute to higher hydrogen content. Assess whether hydrogen is released in the screw extruder during processing.
- Further improvement of feedstock cleaning procedure should be investigated for both screw extrusion feedstock material and welding wires for WAAM. Oxide removal prior to WAAM should be explored to minimize oxide rich regions in as-build components.
- Assess the mechanical properties of AA5183 with the addition of TiC nanoparticles, once the porosity is minimized to a satisfactory level through processing and cleaning procedures.
- Nanoparticles exhibiting high thermal conductivity should be explored in order to obtain full engulfment and even distribution of particles in the as-solidified component, increasing strengthening contributions as well as isotropic mechanical properties.
- Explore whether *in-situ* formation of strengthening phases could improve mechanical properties of aluminium matrix composites (AMCs) through carefully tailored nanoparticles introduction.
- Explore thermal management techniques for heat dissipation to lower building time and anisoptropy of WAAM components.

Bibliography

[1] Allied Market Research. “Aluminum Market by End User (Transport, Building Construction, Electrical Engineering, Consumer Goods, Foil Packaging, Machinery Equipment, and Others), Processing Method (Flat Rolled, Castings, Extrusions, Forgings, Pigments Powder, and Rod Bar) and Series (Series 1, Series 2, Series 3, Series 4, Series 5, Series 6, Series 7 and Series 8)”. In: *Global Opportunity Analysis and Industry Forecast, 2019-2026* (2019).

[2] A.M. Sayed Tofail, E.P. Koumoulus, A. Bandyopadhyay, S. Bose, L. O’Donoghue, and C. Charitidis. “Additive manufacturing: scientific and technological challenges, market uptake and opportunities”. In: *Materials Today* 21 (2017), pp. 22–37. DOI: `10.1016/j.mattod.2017.07.001`.

[3] J.E. Allison and G.S. Cole. “Metal-matrix composites in the automotive industry: Opportunities and challenges”. In: *The Journal of The Minerals* 45 (1993), pp. 19–24. DOI: `10.1007/BF03223361`.

[4] R. Casati and M. Vedani. “Metal Matrix Composites Reinforced by Nano-Particles—A Review”. In: *Metals* 4,1 (2014), pp. 65–83. DOI: `10.3390/met4010065`.

[5] A.R. Kennedy, D.P. Weston, and M.I. Jones. “Reaction in Al – TiC metal matrix composites”. In: *Materials Science and Engineering A* 316 (2001), pp. 2–38. DOI: `10.1016/S0921-5093(01)01228-X`.

[6] K.G. Skorpen. “Screw Extrusion of Light Metals: Development of materials, characterization and process analysis”. Doctoral thesis NTNU Trondheim. 2018. URL: `http://hdl.handle.net/11250/2565656`.

[7] J. Werenskiold, L. Auran, H.J. Roven, N. Ryum, and O. Reiso. “Screw extruder for continous extrusion of materials with high viscosity. International patent number: EP2086697B1 WO2008 06307. Patent reference: JP-A-2004 035 961, US-A-2 787 022”. In: ().

[8] G. Langelandsvik, T. Furu, O. Reiso, and H.J. Roven. “Effects of iron precipitation and novel metal screw extrusion on electrical conductivity and properties of AA1370 aluminium”. In: *Materials Science and Engineering: B* 254 (2020), p. 114505. DOI: `10.1016/j.mseb.2020.114505`.

[9] F. Widerøe and T. Welo. “Using contrast material techniques to determine metal flow in screw extrusion of aluminium”. In: *Journal of Materials Processing Technology* 213 (2013), pp. 1007–1018. DOI: `10.1016/j.jmatprotec.2012.11.013`.

[10] T.J. Stedje. “Characterization of Screw Extruded Rapid Solidified AA6061”. Master thesis NTNU Trondheim. 2014. URL: `http://hdl.handle.net/11250/249577`.

[11] T. Berulfsen. “Screw Extrusion from various Binary Al-XMg Feed Materials - Effects of Heat Treatment on Microstructure”. Master thesis NTNU Trondheim. 2016. URL: `http://hdl.handle.net/11250/2409945`.

[12] O. Ragnvaldsen. “Characterisation of an aluminium matrix nanocomposite wire manufacuted by screw extrusion”. Master thesis NTNU Trondheim. 2019. URL: `http://hdl.handle.net/11250/2624249`.

[13] R. Huang, M. Riddle, D. Graziano, J. Warren, S. Das, S. Nimbalkar, J. Cresko, and E. Masanet. “Energy and emissions saving potential of additive manufacturing:the case of lightweight aircraft components”. In: *Journal of Cleaner Production* 135 (2016), pp. 1559–1570. DOI: `10.1016/j.jclepro.2015.04.109`.

[14] W.E. Frazier. “Metal Additive Manufacturing: A Review”. In: *Journal of Materials Engineering and Performance* 23 (2014), pp. 1917–1928. DOI: `10.1007/s11665-014-0958-z`.

[15] S.W. Williams, F. Martina, A.C. Addison, J. Ding, G. Pardal, and P. Colegrove. “Wire+Arc Additive Manufacturing”. In: *Materials Science and Technology* 32 (2016), pp. 641–647. DOI: `10.1179/1743284715Y.0000000073`.

[16] C.R. Cunningham, J.M. Flynn, A. Shokrani, V. Dhokia, and S.T. Newman. “Invited review article: Strategies and processes for high quality wire arc additive manufacturing”. In: *Additive Manufacturing* 22 (2018), pp. 672–686. DOI: `10.1016/j.addma.2018.06.020`.

[17] C. Zhang, Y. Li, M. Gao, and X. Zeng. “Wire arc additive manufacturing of Al-6Mg alloy using variable polarity cold metal transfer arc as power source”. In: *Materials Science Engineering A* 711 (2018), pp. 415–423. DOI: `10.1016/j.msea.2017.11.084`.

[18] J. Flåm. “Wire Arc Additive Manufacturing of AA5183 using Cold Metal Transfer Technology”. Specialization project NTNU Trondheim. 2019.

[19] International Aluminium Institute. *Global Aluminium Cycle 2018*. 2018. URL: `http://www.world-aluminium.org/statistics/massflow/` (visited on 06/10/2020).

[20] J.K. Solberg. *Teknologiske metaller og legeringer*. Tapir Forlag, 2017.

[21] M. Bertrama, S. Ramkumar, H. Rechberger, G. Rombach, C. Bayliss, K.J. Martchek, D.B. Müller, and G. Liu. “A regionally-linked, dynamic material flow modelling tool for rolled, extruded and cast aluminium products”. In: *Resources, Conservation Recycling* 125 (2017), pp. 48–69. DOI: `10.1016/j.resconrec.2017.05.014`.

[22] M. Tisza and I. Czinege. “Comparative study of the application of steels and aluminium in lightweight production of automotive parts”. In: *International Journal of Lightweight Materials and Manufacture* 1 (2018), pp. 229–238. DOI: `10.1016/j.ijlmm.2018.09.001`.

[23] A. Morita. “Aluminum alloys for automotive applications”. In: International Conference on Aluminium Alloys (ICCA-6) (Toyohashi, Japan, 1998). 1998.

[24] E. Dinsmore. *Electric vehicles to transform aluminium demand*. 2018. URL: `https://www.crugroup.com/knowledge-and-insights/insights/2018/electric-vehicles-to-transform-aluminium-demand/?utm_medium=Press%5C%20release&utm_source=PR%5C%20Newswire&utm_campaign=CRU%5C%20Insight%5C%20-%5C%20ED%5C%20Feb%5C%2018` (visited on 06/11/2020).

[25] G. Djukanovic. *Aluminium vs. steel in electric vehicles – the battle goes on*. 2018. URL: `https://aluminiuminsider.com/aluminium-vs-steel-in-electric-vehicles-the-battle-goes-on/` (visited on 06/05/2020).

[26] International Aluminium Institute. *Primary aluminium production*. 2018. URL: `http://www.world-aluminium.org/statistics/#data` (visited on 05/29/2020).

[27] G.E. Totten and D.S. MacKenzie. *Handbook of Aluminium*. 1st ed. CRC Press, 2003. ISBN: 0-8247-0494-0.

[28] J.L. Murray. "The Al-Mg (Aluminium-Magnesium) system". In: *Journal of Phase Equilibria* 3 (1982), p. 60. DOI: `10.1007/BF02873413`.

[29] E. Huskins, B. Cao, and K. Ramesh. "Strengthening mechanisms in an Al–Mg alloy". In: *Materials Science Engineering: A* 526 (2020), pp. 2292–1298. DOI: `10.1016/j.msea.2009.11.056`.

[30] D.J. Lloyd and S.A. Court. "Influence of grain size on tensile properties of Al-Mg alloys". In: *Materials Science and Technology* 19 (2003), pp. 1349–1354. DOI: `10.1179/026708303225006088`.

[31] R.E. Sanders, S.F. Baumann, and J.D. Embury. "Wrought Non–Heat-Treatable Aluminum Alloys". In: *Treatise on Materials Science Technology* 31 (1989), pp. 65–105. DOI: `10.1016/B978-0-12-341831-9.50008-5`.

[32] M. Bethencourt, F.J. Botana, M.A. Cauqui, M. Marcos, M.A. Rodrıguz, and J.M. Rodrıguez-Izquierdo. "Protection against corrosion in marine environments of AA5083 Al–Mg alloy by lanthanide chlorides". In: *Journal of Alloys and Compounds* 250 (1997), pp. 455–460. DOI: `10.1016/S0925-8388(96)02826-5`.

[33] C. Lea and J.Ball. "The oxidation of rolled and heat treated Al-Mg alloys". In: *Applications of Surface Science* 17 (1984), pp. 344–362. DOI: `10.1016/0378-5963(84)90023-0`.

[34] K.D. Carlson, Z. Lin, and C. Beckermann. "Modeling the Effect of Finite-Rate Hydrogen Diffusion on Porosity Formation in Aluminum Alloys". In: *Metallurgical and Materials Transactions B* 38 (2007), pp. 541–555. DOI: `10.1007/s11663-006-9013-2`.

[35] A. Atrens, N. Winzer, G. Song, W. Dietzel, and C. Blawert. "Stress Corrosion Cracking and Hydrogen Diffusion in Magnesium". In: *International Journal of Hydrogen Energy* 8 (2006), pp. 749–751. DOI: `10.1002/adem.200600050`.

[36] P.D. Lee and J.D Hunt. "Hydrogen porosity in directional solidified aluminium-copper alloys:in situ observation". In: *Acta Materialia* 45 (1997), pp. 4155–4169. DOI: `10.1016/S1359-6454(97)00081-5`.

[37] R. Hardian et al. “Waste Mg-Al based alloys for hydrogen storage”. In: *International Journal of Hydrogen Energy* 43 (2018), pp. 16738–16748. DOI: `10.1016/j.ijhydene.2017.12.014`.

[38] D.W. Aylmore, S.J. Gregg, and W.B. Jepson. “The oxidation of aluminium in dry oxygen in the temperature range 400-500 C”. In: *J. Inst. Metals* 88 (1960).

[39] I.M. Ritchie, J.V. Sanders, and P.L. Weickhardt. “Oxidation of a dilute aluminum magnesium alloy”. In: *Oxidation of Metals* 3 (1971), pp. 91–101. DOI: `10.1007/BF00604741`.

[40] R.K. Hart and J.K Maurin. “The nucleation and growth of oxide islands on aluminum”. In: *Surface Science* 20 (1970), pp. 285–303. DOI: `10.1016/0039-6028(70)90182-2`.

[41] M.J. Dignam. *Electrochemical Materials Science*. 1970, pp. 247–306. DOI: `10.1007/978-1-4757-4825-3_5`.

[42] C.N. Cochran, D.L. Belitskus, and D.L. Kinosz. “Oxidation of Aluminum-Magnesium Melts in Air, Oxygen, Flue Gas and Carbon Dioxide”. In: *Mater. Trans. B.* 8 (1977), pp. 323–332. DOI: `10.1007/BF02657663`.

[43] N. Smith, B. Gleeson, W.A. Saidi, A. Kvithyld, and G. Tranell. “Mechanism behind the Inhibiting Effect of CO2 on the Oxidation of AlMg Alloys”. In: *Ind. Eng. Chem. Res* 58 (2019), pp. 1434–1442. DOI: `10.1021/acs.iecr.8b04691`.

[44] K.K. Chawla. *Metal Matrix Composites*. 2nd ed. Springer-Verlag New York, 2013. ISBN: 978-1-4614-9548-2.

[45] M.K. Surappa. “Aluminium matrix composites: Challenges and opportunities”. In: *Sadhana* 28 (2003), pp. 319–334. DOI: `10.1007/BF02717141`.

[46] T.W. Clyne. *An Introduction to Metal Matrix Composites*. 1993. DOI: `10.1017/CBO9780511623080`.

[47] J. Wadsworth and D.R. Lesuer. “Ancient and modern laminated composites – from theG reat Pyramid of Gizeh to Y2K”. In: *Materials Characterization* 45 (2000), pp. 289–313. DOI: `10.1016/S1044-5803(00)00077-2`.

[48] A.J. Cyriac. “Metal matrix composites: History, status, factors and future”. Master thesis Oklahoma State University. 2011. URL: `https://ui.adsabs.harvard.edu/abs/2011PhDT........81C/abstract`.

[49] K.U. Kainer. *Metal Matrix Composites: Custom-made Materials for Automotive and Aerospace Engineering*. 1st ed. John Wiley Sons, 2006. ISBN: 978-3-527-31360-0.

[50] D.K. Das, P.C. Mishra, S. Singh, and S. Pattanaik. “Fabrication and heat treatment of ceramicreinforced aluminium matrix composites - a review”. In: *Materials Characterization* 9 (2014). DOI: `10.1186/s40712-014-0006-7`.

[51] N. Fatchurrohman, I. Iskandar, S. Suraya, and K. Johan. “Sustainable Analysis in the Product Development of Al-Metal Matrix Composites Automotive Component”. In: *Applied Mechanics and Materials* 695 (2014), pp. 32–35. DOI: `10.4028/www.scientific.net/AMM.695.32`.

[52] D.K. Koli, G. Agnihotri, and R. Purohit. “Advanced Aluminium Matrix Composites: The Critical Need of Automotive and Aerospace Engineering Fields”. In: *Materials Today: Proceedings* 2 (2015), pp. 3032–3041. DOI: `10.1016/j.matpr.2015.07.290`.

[53] S. Singh D.K. Das P.C. Mishra and R.K Thakur. “Properties of ceramic-reinforced aluminium matrix composites - a review”. In: *International Journal of Mechanical and Materials Engineering* 9 (2014). DOI: `10.1186/s40712-014-0012-9`.

[54] T. Pardoen and T.J. Massart. “Interface controlled plastic flow modelled by strain gradient plasticity theory”. In: *Recent Advances in Micromechanics of Materials* 340 (2012), pp. 247–260. DOI: `10.1016/j.crme.2012.02.008`.

[55] P. Garg, A. Jamwal, D. Kumar, K. Kumar, S. Chaudhery, M. Hussain, and P. Gupta. “Advance research progresses in aluminium matrixcomposites: manufacturing applications”. In: *Journal of Materials Research and Technology* 8 (2019), pp. 4924–4939. DOI: `10.1016/j.jmrt.2019.06.028`.

[56] W.D. Callister and D.G. Rethwisch. *Materials Science and Engineering*. 9th ed. John Wiley Sons, 2014. ISBN: 9781118319222.

[57] G. Langelandsvik, O. Ragnvaldsen, J.E Flåm, O.M Akselsen, and H.J Roven. “Wire and Arc Additive Manufacturing with TiC-Nanoparticle Reinforced AA5183 Alloy”. 2020.

[58] D. Weygand, Y. Bréchet, and J. Lépinoux. “Zener pinning and grain growth: a two-dimensional vertex computer simulation”. In: *Acta Materialia* 47 (1999), pp. 961–970. DOI: `10.1016/S1359-6454(98)00383-8`.

[59] D. Hull and D.J. Bacon. *Introduction to Dislocations*. 5th ed. Butterworth-Heinemann, 2011. ISBN: 978-0-080-96673-1.

[60] A.S. Zadeh. “Comparison between current models for the strength of particulate-reinforced metal matrix nanocomposites with emphasis on consideration of Hall–Petch effect”. In: *Materials Science and Engineering A* 531 (2012), pp. 112–118. DOI: `10.1016/j.msea.2011.10.043`.

[61] N. Ramakrishnan. “An analytical study on strengthening of particulate reinforced metal matrix composites”. In: *Acta Materialia* 44 (1996), pp. 69–77. DOI: `10.1016/1359-6454(95)00150-9`.

[62] T.W. Clyne and P.J. Withers. *An introduction to metal matrix composites*. 1st ed. Cambridge University Press, 1993. ISBN: 978-0-511-62308-0.

[63] M. Fattahi, M. Mohammady, N. Sajjadi, M. Honarmand, Y. Fattahi, and S. Akhavan. “Effect of TiC nanoparticles on the microstructure and mechanical properties of gas tungsten arc welded aluminum joints”. In: *Journal of Materials Processing Technology* 2017 (2015), pp. 21–29. DOI: `10.1016/j.jmatprotec.2014.10.023`.

[64] S. Jayalakshmi and M. Gupta. *Metallic Amorphous Alloy Reinforcements in Light Metal Matrices*. 1st ed. Springer International Publishing, 2015. ISBN: 978-3-319-15016-1.

[65] M. Sokoluk, C. Cao, S. Pan, and X. Li. “Nanoparticle-enabled phase control for arc welding of unweldable aluminum alloy 7075”. In: *Nature Communications* 10 (2019). DOI: `10.1038/s41467-018-07989-y`.

[66] P.M. Kelly and M.X. Zhang. “Edge-to-edge matching—The fundamentals”. In: *Metallurgical and Materials Transactions A* 37 (2006), pp. 833–839. DOI: `10.1007/s11661-006-0056-4`.

[67] M.X. Zhang, P.M. Kelly, M.A. Easton, and J.A. Taylor. “Crystallographic study of grain refinement in aluminum alloys using the edge-to-edge matching model”. In: *Acta Materialia* 53 (2005), pp. 1427–1438. DOI: `10.1016/j.actamat.2004.11.037`.

[68] B.S. Murty, S.A. Kori, and M. Chakraborty. "Grain refinement of aluminium and its alloys by heterogeneous nucleation and alloying". In: *International Materials Reviews* 47 (2002), pp. 3–29. DOI: `10.1179/095066001225001049`.

[69] S.D. Bachchhav, S. Roy, and M. Mukhopadhyay. "Parametric analysis of homogeneous and heterogeneous nucleation in subcritical CO2-mediated antisolvent crystallization". In: *Chemical Engineering Research and Design* 106 (2016), pp. 283–297. DOI: `10.1016/j.cherd.2015.12.016`.

[70] J.G Li. "Wetting of ceramic materials by liquid silicon, aluminium and metallic melts containing titanium and other reactive elements: A review". In: *Ceramics International* 20 (1994), pp. 391–412. DOI: `10.1016/0272-8842(94)90027-2`.

[71] S. Avraham and W.D. Kaplan. "Reactive wetting of rutile by liquid aluminium". In: *Journal of Materials Science* 40 (2005), pp. 1093–1100. DOI: `10.1007/s10853-005-6922-4`.

[72] C. Rauwendaal. *Polymer Extrusion*. 5th ed. TCarl Hanser Verlag GmbH Co. KG, 2014. ISBN: 978-1-56990-516-6.

[73] F. Widerøe. "Material Flow in Screw Extrusion of Aluminium". Doctoral thesis NTNU Trondheim. 2012. URL: `http://hdl.handle.net/11250/241707`.

[74] U.M.J. Boin and M. Bertram. "Melting standardized aluminum scrap: A mass balance model for europe". In: *The Journal of The Minerals, Metals Materials Society* 57 (2005), pp. 26–33. DOI: `10.1007/s11837-005-0164-4`.

[75] R.L. Milford, J.M. Allwood, and J.M. Cullen. "Assessing the potential of yield improvements, through process scrap reduction,for energy and CO2abatement in the steel and aluminium sectors". In: *Resources, Conservation and Recycling* 55 (2011), pp. 1185–1195. DOI: `10.1016/j.resconrec.2011.05.021`.

[76] J.R. Duflou, A.E. Tekkaya, M. Haase, T. Welo, K. Vanmeensel, K. Kellens, W. Dewulf, and D. Paraskevasa. "Environmental assessment of solid state recycling routes for aluminium alloys: Can solid state processes significantly reduce the environmental impact of aluminium recycling?" In: *CIRP Annals* 64 (2015), pp. 37–41. DOI: `10.1016/j.cirp.2015.04.051`.

[77] K.G. Skorpen, O. Reiso, and H.J. Roven. "A physical based empirical model for the accumulated strain in novel Metal Continuous Screw Extrusion (MCSE)". In: *Journal of Materials Processing Technology* 282 (2020), p. 116670. DOI: `10.1016/j.jmatprotec.2020.116670`.

[78] J.Z. Li, M.R. Alkahari, N.A. Binti Rosli, R. Hasan, M.N. Sudinand, and F.R. Ramli. "Review of Wire Arc Additive Manufacturing for 3D Metal Printing". In: *International Journal of Automation Technology* 13 (2019), pp. 346–353. DOI: `10.20965/ijat.2019.p0346`.

[79] C. Weller, R. Kleer, and F.T. Piller. "Economic implications of 3D printing: Market structure models in light of additive manufacturing revisited". In: *International Journal of Production Economics* 164 (2015), pp. 43–56. DOI: `10.1016/j.ijpe.2015.02.020`.

[80] R. Liu, Z. Wang, T. Sparks, F. Liou, and J. Newkirk. “13 - Aerospace applications of laser additive manufacturing”. In: *Laser Additive Manufacturing* (2017), pp. 351–371. DOI: `10.1016/B978-0-08-100433-3.00013-0`.

[81] A. Eckhoff. *Additive Manufacturing + Aerospace Industry = Efficiency*. 2018. URL: `https://blogs.sw.siemens.com/nx-manufacturing/additive-manufacturing-aerospace-industry-efficiency/` (visited on 06/14/2020).

[82] R.R. Unocic and J.N. DuPont. “Process efficiency measurements in the laser engineered net shaping process”. In: *Metallurgical and Materials Transactions B* 35 (2004), pp. 143–152. DOI: `10.1007/s11663-004-0104-7`.

[83] L. Rännar, A. Glad, and C.G. Gustafson. “Efficient cooling with tool inserts manufactured by electron beam melting”. In: *Rapid Prototyping Journal* 13 (2007), pp. 128–135. DOI: `10.1108/13552540710750870`.

[84] F. Wang, S. Williams, P. Colegrove, and A.A. Antonysamy. “Microstructure and Mechanical Properties of Wire and Arc Additive Manufactured Ti-6Al-4V”. In: *Metallurgical and Materials Transactions A* 44 (2013), pp. 968–977. DOI: `10.1007/s11661-012-1444-6`.

[85] J.N. DuPont and A.R. Marder. “Thermal Efficiency of Arc Welding Processes”. In: *Welding Journal-Including Welding Research Supplement* 74 (1995), pp. 406–416.

[86] N. Stenbacka. “Review of Arc Efficiency Values for Gas Tungsten Arc Welding”. In: *Soldagem inspeção* 18 (2013), pp. 380–390. DOI: `10.1590/S0104-92242013000400010`.

[87] D. Ding, Z. Pan, D. Cuiuri, and H. Li. “Wire-feed additive manufacturing of metal components: technologies, developments and future interests”. In: *The International Journal of Advanced Manufacturing Technology* 81 (2015), pp. 465–481. DOI: `10.1007/s00170-015-7077-3`.

[88] American Welding Society. *Welding Handbook*. 9th ed. American welding Society, 2004. ISBN: 0-87171-729-8.

[89] K. Furukawa. “New CMT arc welding process – welding of steel to aluminium dissimilar metals and welding of superthin aluminium sheets”. In: *Welding International* 20 (2006), pp. 440–445. DOI: `10.1533/wint.2006.3598`.

[90] P. Kah, R. Suoranta, and J. Martikainen. “Advanced gas metal arc welding processes”. In: *International Journal of Advanced Manufacturing Technology* 67 (2013), pp. 655–674. DOI: `10.1007/s00170-012-4513-5`.

[91] J. Feng, H. Zhang, and P. He. “The CMT short-circuiting metal transfer process and its use in thin aluminium sheets welding”. In: *Materials and Design* 30 (2009), pp. 1850–1852. DOI: `10.1016/j.matdes.2008.07.015`.

[92] B. Cong, J. Ding, and S. Williams. “Effect of arc mode in cold metal transfer process on porosity of additively manufactured Al-6.3%Cu alloy”. In: *The International Journal of Advanced Manufacturing Technology* 76 (2015), pp. 1593–1606. DOI: `10.1007/s00170-014-6346-x`.

[93] B. Cong, Z. Qi, B. Qi, H. Sun, G. Zhao, and J. Ding. “A Comparative Study of Additively Manufactured Thin Wall and Block Structure with Al-6.3%Cu Alloy Using Cold Metal Transfer Process”. In: *Applied Sciences* 7 (2017), p. 275. DOI: `10.3390/app7030275`.

[94] W. Kurz and D.J. Fisher. *Fundamentals of Solidification*. 4th ed. Trans Tech Publications, 1998. ISBN: 978-0-87849-804-8.

[95] J.D. Hunt. "Steady State Columnar and Equiaxed Growth of Dendrites and Eutectic". In: *Materials Science and Engineering* 65 (1984), pp. 75–83. DOI: `10.1016/0025-5416(84)90201-5`.

[96] J. Hutt and D. StJohn. "The origins of the equiaxed zone -Review of theoretical and experimental work". In: *International Journal of Cast Metals Research* 11 (1998), pp. 13–22. DOI: `10.1080/13640461.1998.11819254`.

[97] J.A. Spittle. "Columnar to equiaxed grain transition in as solidified alloys". In: *International Materials Reviews* 51 (2006), pp. 247–269. DOI: `10.1179/174328006X102493`.

[98] K.F. Kelton and A.L. Greer. *Nucleation in Condensed Matter - Applications in Materials and Biology*. 1st ed. Pergamon, 2010. ISBN: 9780080421476.

[99] A.L Greer. *Solidification and Casting*. Institute of Physics Publishing, Bristol, 2003.

[100] Q.Z Diao and H.L. Tsai. "Modeling of solute redistribution in the mushy zone during solidification of aluminum-copper alloys". In: *Metallurgical Transactions A* 24 (1993), pp. 963–973. DOI: `10.1007/BF02656518`.

[101] J.H. Martin, B.D. Yahata, J.M. Hundley, J.A. Mayer, T.A. Schaedler, and T.M. Pollock. "3D printing of high-strength aluminium alloys". In: *Nature* 549 (2017), pp. 365–369. DOI: `10.1038/nature23894`.

[102] V. Manvatkar, A. De, and T. DebRoy. "Spatial variation of melt pool geometry, peak temperature and solidification parameters during laser assisted additive manufacturing process". In: *Materials Science and Technology* 31 (2015), pp. 924–930. DOI: `10.1179/1743284714Y.0000000701`.

[103] Sindo K. *Welding Metallurgy*. 2nd ed. John Wiley Sons, Inc, 2002. ISBN: 978-0-471-43491-7.

[104] H.L. Wei, J.W. Elmer, and T. DebRoy. "Origin of grain orientation during solidification of an aluminum alloy". In: *Acta Materialia* 115 (2016), pp. 123–131. DOI: `10.1016/j.actamat.2016.05.057`.

[105] P. Schempp and C.E. Cross. "Solidification of GTA Aluminum Weld Metal : Part I – Grain Morphology Dependent upon Alloy Composition and Grain Refiner Content". In: *Welding Journal* 93 (2014), pp. 53–59.

[106] B. Wu, Z. Pan, D. Ding, D. Cuiuri, H. Li, J. Xu, and J. Norrish. "A review of the wire arc additive manufacturing of metals: properties,defects and quality improvement". In: *Journal of Manufacturing Processes* 35 (2018), pp. 127–139. DOI: `10.1016/j.jmapro.2018.08.001`.

[107] J. Gu, J. Ding, S.W. Williams, H. Gu, P. Ma, and Y. Zhai. "The effect of inter-layer cold working and post-deposition heat treatment on porosity in additively manufactured aluminum alloys". In: *Journal of Materials Processing Technology* 230 (2016), pp. 26–34. DOI: `10.1016/j.jmatprotec.2015.11.006`.

[108] Y. Zhang, J. Xu, and T. Zhai. "Distributions of pore size and fatigue weak link strengthin an A713 sand cast aluminum alloy". In: *Materials Science and Engineering A* 527 (2010), pp. 3639–3644. DOI: `10.1016/j.msea.2010.03.104`.

[109] R.J. Fruehan and P.N. Anyalebechi. *Casting*. Vol. 15. ASM International, 2008. ISBN: 978-0-87170-711-6.

[110] H. Mayer, M. Papakyriacou, B. Zettl, and S.E. Stanzl-Tschegg. "Influence of porosity on the fatigue limit of die cast magnesium and aluminium alloys". In: *International Journal of Fatigue* 25 (2003), pp. 245–256. DOI: `10.1016/S0142-1123(02)00054-3`.

[111] D.E.J. Talbot. "Effects of Hydrogen in Aluminium, Magnesium, Copper, and Their Alloys". In: *International Metallurgical Reviews* 20 (1975), pp. 166–184. DOI: `10.1179/imtlr.1975.20.1.166`.

[112] J.P. Harvey and P. Chartrand. "A review of the wire arc additive manufacturing of metals: properties, defects and quality improvement". In: *Metallurgical and Materials Transactions B* 41 (2010), pp. 908–924. DOI: `10.1007/s11663-010-9381-5`.

[113] A.P. Boeira, I.L. Ferreira, and A. Garcia. "Alloy composition and metal/mold heat transfer efficiency affecting inverse segregation and porosity of as-cast Al–Cu alloys". In: *Materials and Design* 30 (2009), pp. 2090–2098. DOI: `10.1016/j.matdes.2008.08.032`.

[114] D.A. Porter, K.E. Easterling, and M.Y.A. Sherif. *Phase Transformations in Metals and Alloys*. 3rd ed. CRC Press, 2009, p. 310. ISBN: 978-1-42006-210-6.

[115] J.P. Oliveira, T.G. Santos, and R.M. Miranda. "Revisiting fundamental welding concepts to improve additive manufacturing: From theory to practice". In: *Progress in Materials Science* 107 (2019), p. 100590. DOI: `10.1016/j.pmatsci.2019.100590`.

[116] J. Gu, S. Yang, M. Gao, J. Bai, Y. Zhai, and J. Ding. "Micropore evolution in additively manufactured aluminum alloys under heat treatment and inter-layer rolling". In: *Materials Design* 186 (2019), p. 108288. DOI: `10.1016/j.matdes.2019.108288`.

[117] J. Schindelin, I. Arganda-Carreras, and E. Frise. "Fiji: an open-source platform for biological-image analysis". In: *Nature methods* 9 (2012), pp. 676–682. DOI: `doi:10.1038/nmeth.2019`.

[118] M. Doube, M.M. Kłosowski, I. Arganda-Carreras, F.P. Cordelières, R.P. Dougherty, J.S. Jackson, B. Schmid, J.R. Hutchinsong, and S.J. Shefelbine. "BoneJ: Free and extensible bone image analysis in ImageJ". In: *Bone* 47 (2010), pp. 1076–1079. DOI: `10.1016/j.bone.2010.08.023`.

[119] E.A. Alberti, B.M.P. Bueno, and D'Oliveira. "Additive manufacturing using plasma transferred arc". In: *The International Journal of Advanced Manufacturing Technology* 83 (2016), pp. 1861–1871. DOI: `10.1007/s00170-015-7697-7`.

[120] J. Xiong, Y. Lei, and R. Li. "Finite element analysis and experimental validation of thermal behavior for thin-walled parts in GMAW-based additive manufacturing with various substrate preheating temperatures". In: *Applied Thermal Engineering* 126 (2017), pp. 43–52. DOI: `10.1016/j.applthermaleng.2017.07.168`.

[121] D.H. StJohn, M. Qian, M.A. Easton, and P. Cao. "The Interdependence Theory: The relationship between grain formation and nucleant selection". In: *Acta Materialia* 59 (2011), pp. 4907–4921. DOI: `10.1016/j.actamat.2011.04.035`.

[122] M.J. Bermingham, D.H. StJohn, J. Krynen, S. Tedman-Jones, and M.S. Dargusch. “Promoting the columnar to equiaxed transition and grain refinement of titanium alloys during additive manufacturing”. In: *Acta Materialia* 168 (2019), pp. 261–274. DOI: `10.1016/j.actamat.2019.02.020`.

[123] A.F. Boostani et al. “Enhanced tensile properties of aluminium matrix composites reinforced with graphene encapsulated SiC nanoparticles”. In: *Composites: Part A* 68 (2015), pp. 155–163. DOI: `10.1016/j.compositesa.2014.10.010`.

[124] M. Kok. “Production and mechanical properties of Al2O3 particle-reinforced 2024 aluminium alloy composites”. In: *Journal of Materials Processing Technology* 161 (2005), pp. 381–387. DOI: `10.1016/j.jmatprotec.2004.07.068`.

[125] X. Li, Q. Cai, B. Zhao, B.Li, B. Liu, and W. Ma. “Production and mechanical properties of Al2O3 particle-reinforced 2024 aluminium alloy composites”. In: *Journal of Alloys and Compounds* 699 (2017), pp. 283–290. DOI: `http://dx.doi.org/10.1016/j.jallcom.2016.12.367`.

[126] R. Asthana and S.N. Tewari. “The engulfment of foreign particles by a freezing interface”. In: *Journal of Materials Science* 28 (1993), pp. 5414–5425. DOI: `10.1007/BF00367810`.

[127] S.N. Omenyi, R.P. Smith, and A.W. Neumann. “Determination of solid/melt interfacial tensions and of contact angles of small particles from the critical velocity of engulfing”. In: *Journal of Colloid and Interface Science* 75 (1980), pp. 117–125. DOI: `10.1016/0021-9797(80)90355-0`.

[128] D.R. Uhlmann, B. Chalmers, and K.A. Jackson. “Interaction Between Particles and a Solid-Liquid Interface”. In: *Journal of Applied Physics* 35 (1964), p. 2986. DOI: `10.1016/0021-9797(80)90355-0`.

[129] M.K. Surappa and P.K. Rohatgi. “Preparation and properties of cast aluminium-ceramic particle composites”. In: *Journal of Materials Science* 16 (1981), pp. 983–993. DOI: `10.1007/BF00542743`.

[130] D. Shangguan, S. Ahuja, and D.M. Stefanescu. “An analytical model for the interaction between an insoluble particle and an advancing solid/liquid interface”. In: *Metallurgical Transactions A* 23 (1992), pp. 669–680. DOI: `10.1007/BF02801184`.

[131] D.M. Stefanescu, F.R. Juretzko, A. Catalina, B.K. Dhindaw, S. Sen, and P.A. Curreri. “Particle engulfment and pushing by solidifying interfaces: Part II. Microgravity experiments and theoretical analysis”. In: *Metallurgical and Materials Transactions A* 29 (1998), pp. 1697–1706. DOI: `10.1007/s11661-998-0092-3`.

[132] J. Lipton, M.E. Glicksman, and W. Kurz. “Dendritic Growth into Undercooled Alloy Melts”. In: *Materials Science and Engineering* 65 (1984), pp. 57–63. DOI: `10.1016/0025-5416(84)90199-X`.

[133] E.M. Agaliotis, M.R. Rosenberger, A.E. Ares, and C.E. Schvezovy. “Influence of the shape of the particles in the solidification of composite materials”. In: *Procedia Materials Science 1* (2013), pp. 58–63. DOI: `doi:10.1016/j.mspro.2012.06.008`.

[134] K. Wang, H.Y. Jiang, Y.W. Jia, H. Zhou, Q.D. Wang, B. Ye, and W.J. Ding. “Nanoparticle-inhibited growth of primary aluminum in Al–10Si alloys”. In: *Acta Materialia* 103 (2016), pp. 252–263. DOI: `10.1016/j.actamat.2015.10.005`.

[135] A.L Greer. “Overview: Application of heterogeneous nucleation in grain-refining of metals”. In: *J. Chem. Phys.* 145 (2016), p. 211704. DOI: `10.1063/1.4968846`.

[136] M. vandyoussefi, J. Worth, and A.L. Greer. “Effect of instability of TiC particles ongrain refinement of Al and Al–Mg alloysby addition of Al–Ti–C inoculants”. In: *Materials Science and Technology* 16 (2000), pp. 1121–1128. DOI: `10.1179/026708300101507046`.

[137] R.O.G. Blachnik, P. Gross, and C. Hayman. “Enthalpies of formation of the carbides of aluminium and beryllium”. In: *Trans. Faraday Soc.* 66 (1970), pp. 1058–1064. DOI: `10.1039/TF9706601058`.

[138] S.H. Wang and P.W. Kao. “Acta Materialia”. In: *Materials Science and Technology* 46 (1998), pp. 2675–2682. DOI: `10.1016/S1359-6454(97)00470-9`.

[139] J.A. Hawk, P.K. Mirchandani, E. Arzt, and J. Rosler. “Dispersion Strengthened Al Alloys”. In: *TMS Warrendale* (1998), pp. 31–56.

[140] Q. Zhang, B.L. Xiao, W.G. Wang, and Z.Y. Ma. “Reactive mechanism and mechanical properties of in situcomposites fabricated from an Al–TiO2systemby friction stir processing”. In: *Acta Materialia* 60 (2012), pp. 7090–7103. DOI: `10.1016/j.actamat.2012.09.016`.

[141] D. Dispinar and J. Campbell. “Porosity, hydrogen and bifilm content in Al alloy castings”. In: *Materials Science and Engineering: A* 528 (2011), pp. 3860–3865. DOI: `10.1016/j.msea.2011.01.084`.

[142] S. Katayama, A. Matsunawa, and K. Kojima. “Hydrogen diffusion in aluminium at high temperatures”. In: *Welding International* 12 (1998), pp. 774–789. DOI: `10.1080/09507119809448977`.

[143] Y. Zhao, A.C. Dillon, Y.H. Kim, M.J. Heben, and S.B. Zhang. “Self-catalyzed hydrogenation and dihydrogen adsorption on titanium carbide nanoparticles”. In: *Chemical Physics Letters* 425 (2006), pp. 273–277. DOI: `https://doi:10.1016/j.cplett.2006.05.034`.

[144] S. McWhorter, K. O’Malley, J. Adams, G. Ordaz, K. Randolph, and N.T. Stetson. “Moderate Temperature Dense Phase Hydrogen Storage Materials within the US Department of Energy (DOE) H2 Storage Program: Trends toward Future Development”. In: *Crystals* 2 (2012), pp. 413–445. DOI: `https://doi:10.3390/cryst2020413`.

[145] A. Haboudou, P. Peyre, A.B. Vannes, and G. Peix. “Reduction of porosity content generated during Nd:YAG laser welding of A356 and AA5083 aluminium alloys”. In: *Materials Science and Engineering: A Volume 363, Issues 1–2, 20 December 2003, Pages 40-52* 363 (2003), pp. 40–52.

[146] A.W. AlShaer, L. Li, and A. Mistry. “The effects of short pulse laser surface cleaning on porosity formationand reduction in laser welding of aluminium alloy for automotive-component manufacture”. In: *Optics Laser Technology* 24 (2014), pp. 162–171. DOI: `10.1016/j.optlastec.2014.05.010`.

[147] M.J. Cieslak and P.W. Fuerschbach. “On the Weldability, Composition, and Hardness of Pulsed and Continuous Nd:YAG Laser Welds in Aluminum Alloys 6061,5456, and 5086”. In: *Metallurgical Transactions B* 19 (1988), pp. 319–329. DOI: `10.1007/BF02654217`.

[148] J-B. Wang, H. Nishimura, S. Katayma, and M. Mizutani. “Evaporation phenomena of magnesium from droplet at welding wire tip in pulsed MIG arc welding of aluminium alloys”. In: *Science and Technology of Welding and Joining* 16 (2011), pp. 418–425. DOI: `10.1179/1362171810Y.0000000030`.

[149] T. Klein and M. Schnall. “Control of macro-/microstructure and mechanical properties of a wire-arc additive manufactured aluminum alloy”. In: *The International Journal of Advanced Manufacturing Technology* 108 (2020), pp. 235–244. DOI: `10.1007/s00170-020-05396-6`.

[150] M. Kutsuna and Q. Yan. “Study on porosity formation in laser welds in aluminium alloys (Report 1): Effects of hydrogen and alloying elements”. In: *Welding International* 12 (1998), pp. 937–949. DOI: `10.1080/09507119809448539`.

[151] D.D. Harwig, J.E. Dierksheide, D. Yapp, and S. Blackman. “Arc behavior and melting rate in the VP-GMAW process”. In: *Welding Journal* 85 (2006), pp. 52–62.

[152] R. Kumar, U. Dilthey, D.K. Dwivedi, and P.K.Ghosh. “Thin sheet welding of Al 6082 alloy by AC pulse-GMA and AC wave pulse-GMA welding”. In: *Materials Design* 30 (2009), pp. 306–313. DOI: `10.1016/j.matdes.2008.04.073`.

[153] E. Hashimoto and T. Kino. “Hydrogen diffusion in aluminium at high temperatures”. In: *Journal of Physics F: Metal Physics* 13 (1983), pp. 1157–1165. DOI: `10.1088/0305-4608/13/6/013`.

[154] X. Fang, L. Zhang, G. Chen, X. Dang, K. Huang, L. Wang, and B. Lu. “Correlations between Microstructure Characteristics and Mechanical Properties in 5183 Aluminium Alloy Fabricated by Wire-Arc Additive Manufacturing with Different Arc Modes”. In: *Materials* 11 (2018). DOI: `10.3390/ma11112075`.

[155] A. Horgar, H. Fostervoll, B. Nyhus, X. Ren, M. Eriksson, and O.M. Akselsen. “Additive manufacturing using WAAM with AA5183 wire”. In: *Journal of Materials Processing Technology* 259 (2018), pp. 68–74. DOI: `10.1016/j.jmatprotec.2018.04.014`.

[156] B. Gungor, E. Kaluc, E. Tabanb, and A. Sik. “Mechanical and microstructural properties of robotic Cold Metal Transfer (CMT) welded 5083-H111 and 6082-T651 aluminum alloys”. In: *Materials Design* 54 (2014), pp. 207–211. DOI: `10.1016/j.matdes.2013.08.018`.

[157] L.J Silva, D.M. Souza, D.B. Araújo, R.P. Reis, and A. Scotti. “Concept and validation of an active cooling technique to mitigate heat accumulation in WAAM”. In: *The International Journal of Advanced Manufacturing Technology* 107 (2020), pp. 2513–2523. DOI: `10.1007/s00170-020-05201-4`.

[158] C. Su, X. Chen, C. Gao, and Y. Wang. “Effect of heat input on microstructure and mechanical properties of Al-Mg alloys fabricated by WAAM”. In: *Applied Surfaces Science* 486 (2019), pp. 431–440. DOI: `10.1016/j.apsusc.2019.04.255`.

[159] H. Geng, J. Li, J. Xiong, X. Lin, and F. Zhang. “Geometric Limitation and Tensile Properties of Wire and Arc Additive Manufacturing 5A06 Aluminum Alloy Parts”. In: *Journal of Materials Engineering and Performance* 26 (2017), pp. 621–629. DOI: `10.1007/s11665-016-2480-y`.

[160] J.C. Dutra, R.H. Gonçalves e Silva, B.M. Savi, C. Marques, and O.E. Alarcon. “Metallurgical characterization of the 5083H116 aluminum alloy welded with the cold metal transfer process and two different wire-electrodes (5183 and 5087)”. In: *Welding in the World* 59 (2015), pp. 797–807. DOI: `10.1007/s40194-015-0253-0`.

[161] N.K. Babu, M.K Talari, P. Dayou, S. Zheng, W. Jun, and K. SivaPrasad. “Influence of titanium–boron additions on grain refinement of AA6082 gas tungsten arc welds”. In: *Materials Design* 40 (2012), pp. 467–475. DOI: `10.1016/j.matdes.2012.03.056`.

[162] K.L. Firestein, S. Corthay, A.E. Steinman, A.T. Matveev, A.M. Kovalskii, I.V. Sukhorukova, D. Golberg, and D.V. Shtansky. “High-strength aluminum-based composites reinforced with BN, AlB2 and AlN particles fabricated via reactive spark plasma sintering of Al-BN powder mixtures”. In: *Materials Science and Engineering: A* 681 (2017), pp. 1–9. DOI: `10.1016/j.msea.2016.11.011`.

[163] H. Fujii, H. Nakae, and K. Okada. “Interfacial reaction wetting in the boron nitride/molten aluminum system”. In: *Acta metallurgica et materialia* 41 (1993), pp. 2963–2971. DOI: `10.1016/0956-7151(93)90111-5`.

[164] K.B. Lee, H.S. Sim, S.W. Heo, H.R.Yoo, S.Y.Cho, and H. Kwon. “Tensile properties and microstructures of Al composite reinforced with BN particles”. In: *Composites: Part A* 33 (2002), pp. 709–715. DOI: `10.1016/S1359-835X(02)00011-8`.

[165] J. Wang, D. Yi, X. Su, F. Yin, and H. Li. “Properties of submicron AlN particulate reinforced aluminum matrix composite”. In: *Materials Design* 30 (2009), pp. 78–81. DOI: `10.1016/j.matdes.2008.04.039`.

Appendices

A AA6082 aluminium alloy

In this section, experimental work on nanoparticle introduction to AA6082 aluminium alloy is presented. A flow chart outlining the additional work is shown in Figure 7.1.

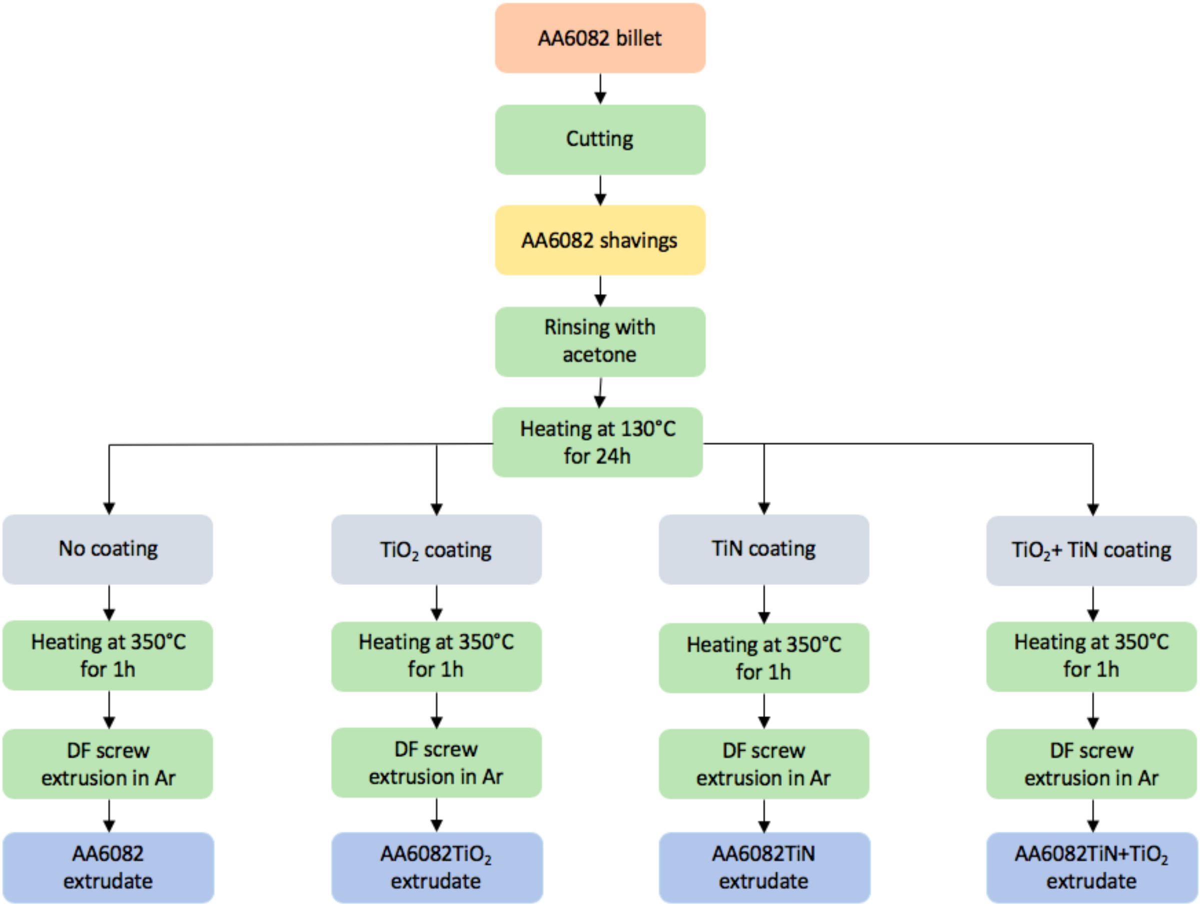

Figure 7.1: Flow chart illustrating experimental work on nanoparticle introduction in AA6082 aluminium alloys.

A.1 Preparation of material

In this section, pre-processing of the feedstock material for metal continuous screw extrusion is outlined.

The feedstock material was delivered as a AA6082 billet from *Hydro Sunndalsøra*. The billet was cut to produce shavings for later nanoparticle milling. Shavings were cleansed both thermally and chemically.

Firstly, chemical cleansing were performed. The shavings were rinsed with acetone for about 1 min, and dried over a sieve. Contact with water was avoided due to possible unwanted oxide formation. Secondly, the shavings were thermally cleansed in for 24h in a *Termaks* heating cabinet to remove organic residue by heating.

A.2 Nanoparticle coating

The thermally and chemically cleansed aluminium alloy AA6082 were coated with nanoparticles. Three different compositions were used, TiO_2, TiN and a mixture of TiO_2/TiN.

- 3 wt% TiO_2 AA6082
- 3 wt% TiN AA6082
- 1 wt% TiO_2 + 2 wt% TiN AA6082

The nanoparticles was produced and supplied by *SINTEF Industri*, with particle diameter of $20\,\mathrm{nm}$ for TiN and $50\,\mathrm{nm}$ for TiO_2. Before MCSE, each batch of nanoparticle-coated AA6082 shaving were heated at 350°C for 1h in a *Nabertherm P300* thermal convection oven at ambient atmosphere.

A.3 Metal continuous screw extrusion

The feedstock aluminium alloy AA6082 shavings were extruded using a laboratory prototype metal continuous screw extruder with double flight screw developed by *NTNU* in collaboration with *Norsk Hydro*. The screw extruder was pre-heated using an copper induction coil before each run to mitigate the risk of thermal cracking of hardware during manufacturing. The heating effect was regulated according to temperature recorded from the thermocouple wires. The diameter of the nozzle opening was 0.6 mm for all of the produced wires.

To avoid oxidation of the AA6082 wire, chemically pure argon gas was used as a shielding gas during screw extrusion for all four experiments.

The AA6082 extrudates were intended for comparison of different nanoparticle contributions, both in terms of grain refining and strength increase. Each extrudate were drawn to a diameter of 1.2 mm to be used for welding wires in WAAM.

B Identification of phases by EDS point analysis

In this section, EDS analysis of phases in the AA5183TiC-CG/AA5183-CG WAAM thin wall is presented. EDS point analysis of grey phase assumed to be Al_3Ti in Figure 4.15 and Figure 4.16 is shown in Figure 7.2. EDS point analysis of white particles assumed to be TiC in Figure 4.13 and Figure 4.14, is shown in Figure 7.3. EDS point analysis of grey spherical particles assumed to be SiO_2 in Figure 4.13 and Figure 4.14, is shown in Figure 7.4. EDS point analysis of oxide particles in the pore interior volume shown Figure 4.22 is shown in Figure 7.6. EDS point analysis of aluminium matrix Figure 4.13 and Figure 4.14, is shown in Figure 7.4. EDS point analysis of interface between irregular pore and grain in Figure 4.24 is shown in Figure 7.7 and Figure 7.8.

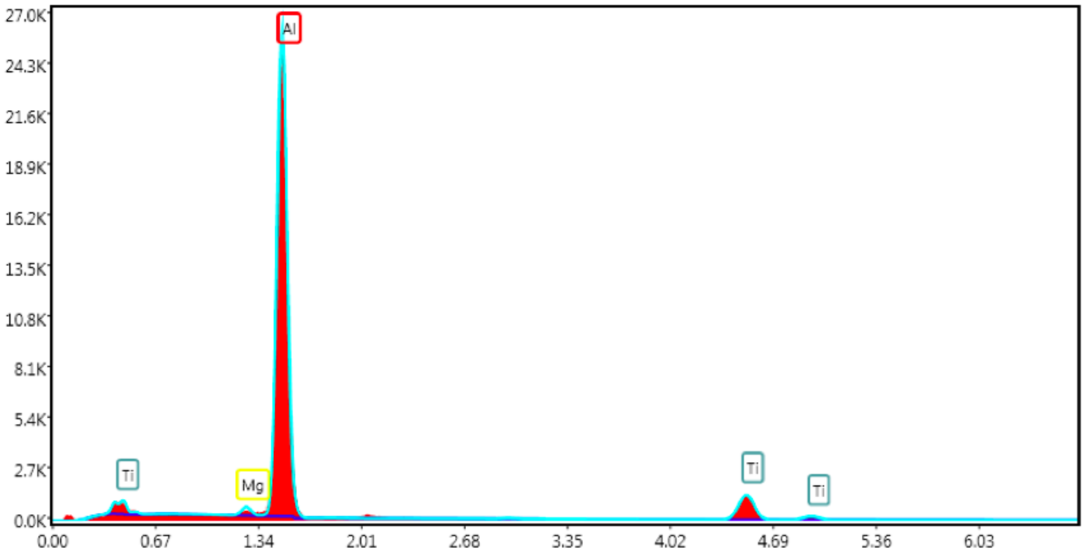

Figure 7.2: EDS point analysis of grey phase in Figure 4.16, assumed to be intermetallic Al_3Ti phase

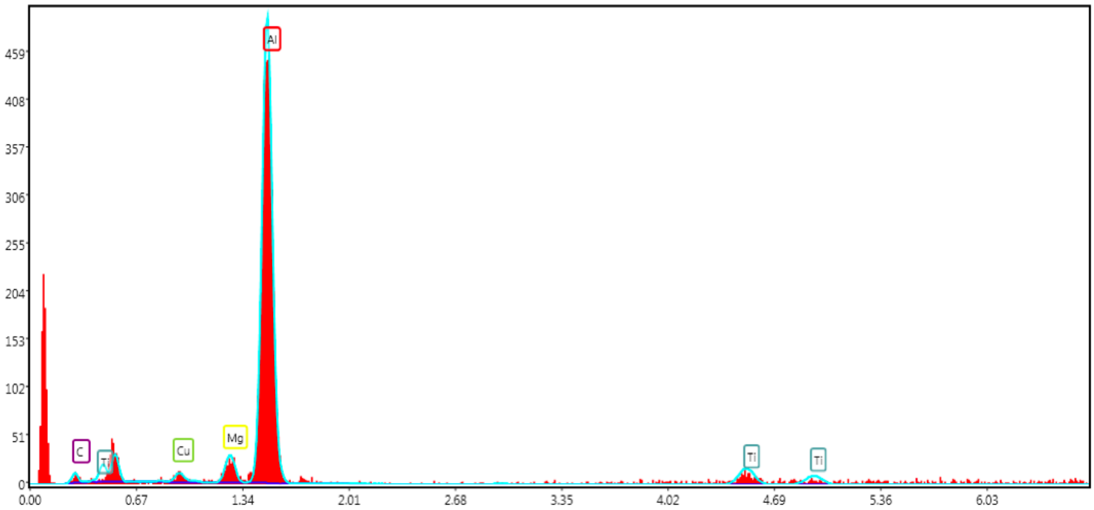

Figure 7.3: EDS point analysis of white particles in Figure 4.14, assumed to be clustered TiC nanoparticles.

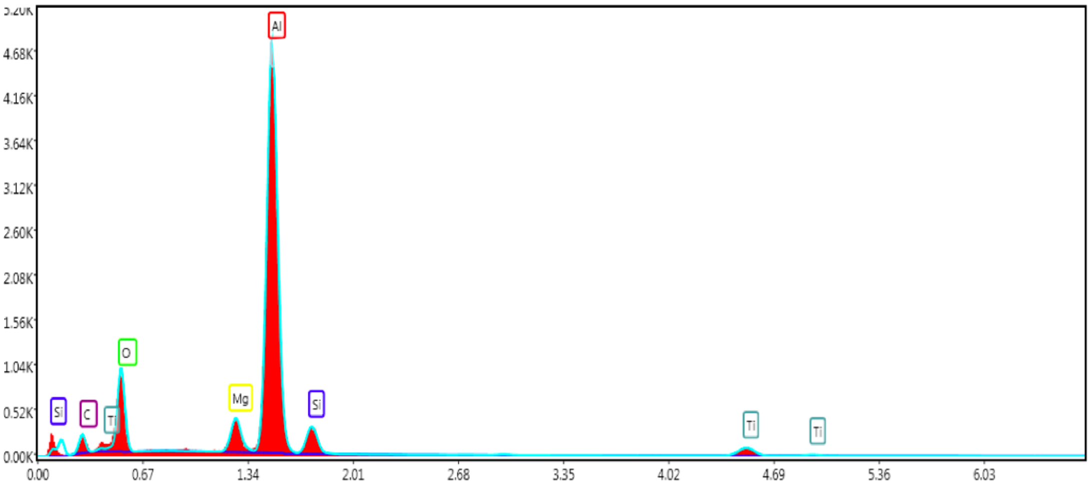

Figure 7.4: EDS point analysis of white particles in Figure 4.14, assumed to be spherical SiO_2 polishing particles.

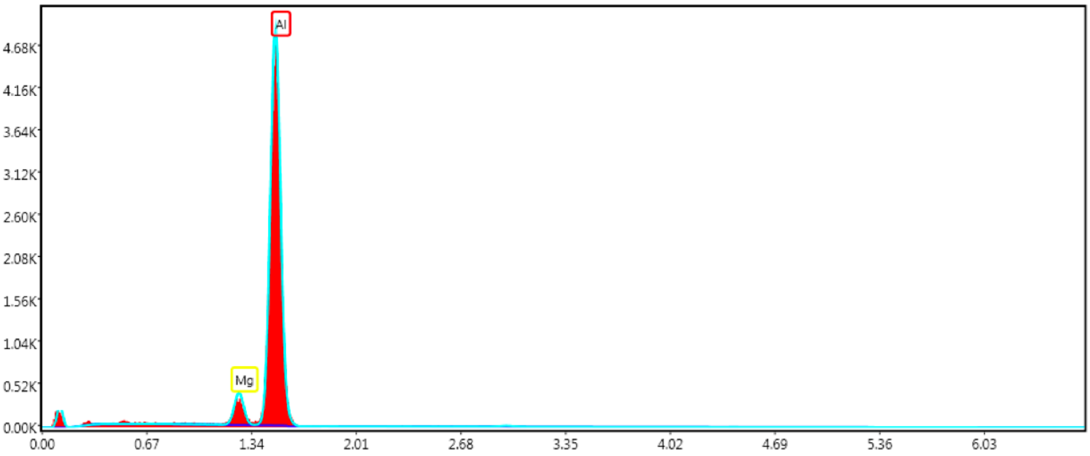

Figure 7.5: EDS point analysis of aluminium matrix in Figure 4.14.

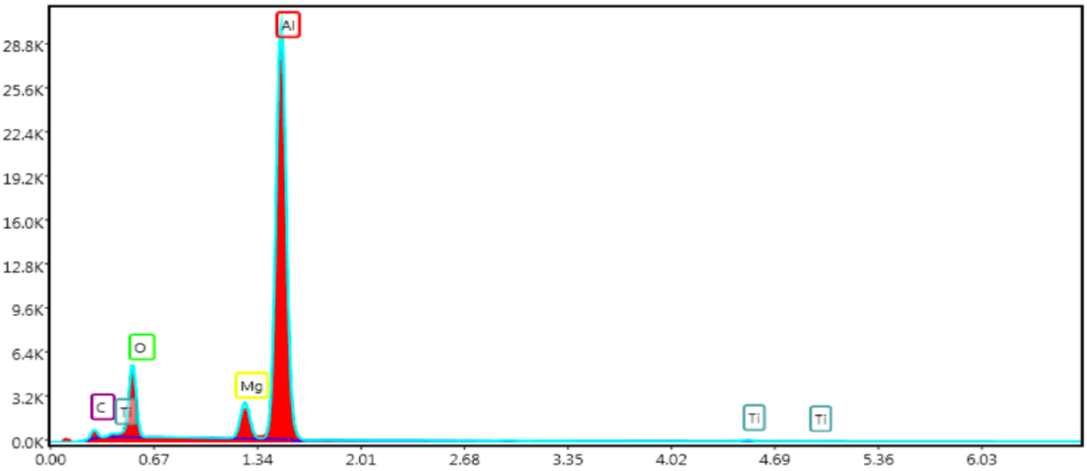

Figure 7.6: EDS point analysis of oxide particle $MgAl_2O_4$ at pore surface shown in Figure 4.22.

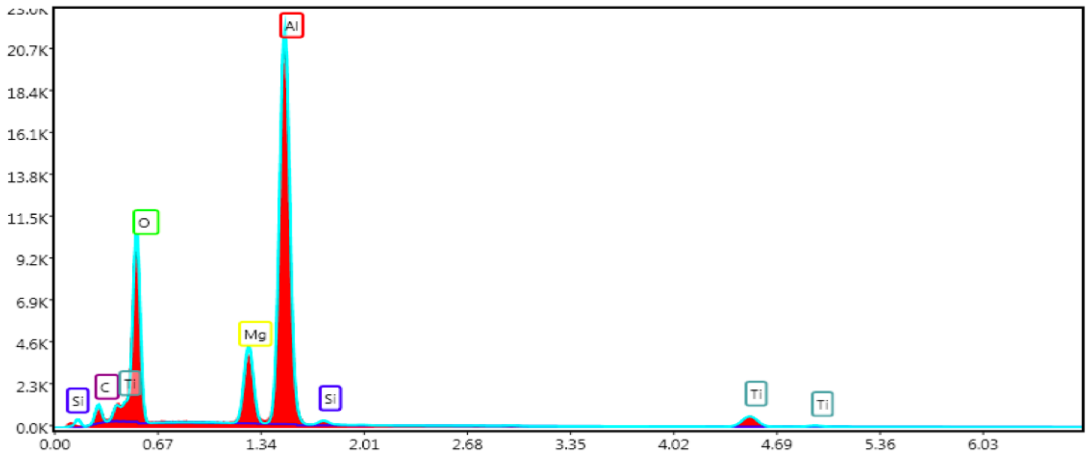

Figure 7.7: EDS point analysis of white phase in Figure 4.24, indicate oxides.

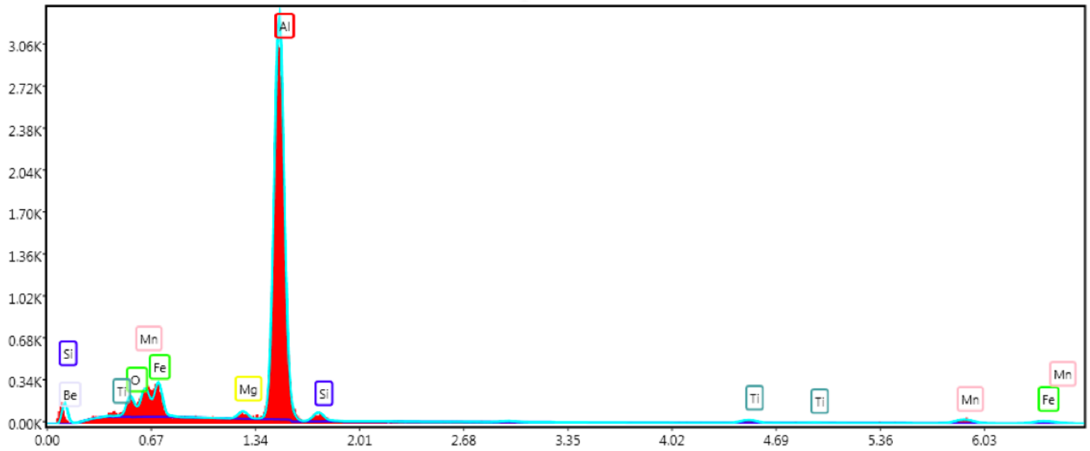

Figure 7.8: EDS point analysis of grey phase in Figure 4.24, indicate manganese rich phase.

C Characterization of AA5183 heat-treated welding wires

1.2 mm drawn and shaved welding wires from AA5183 extrudate were subject to heat-treatment in a *NaberthermN17/HR* at 560 ^{c}ircC for 2h in inert argon atmosphere, as described in section 3.3.

The heat-treated AA5183 welding wire from *Safra* is presented in Figure 7.9, and non-heat-treated in Figure 7.10. Heat-treated AA5183-CG extrudate welding wire is presented in Figure 7.12, non-heat treated in Figure 7.11. It appears that heat-treated wires show recrystallization of grain structure, due to the elevated temperatures. There was no sign of increasing porosity in the welding wires after heat-treatment

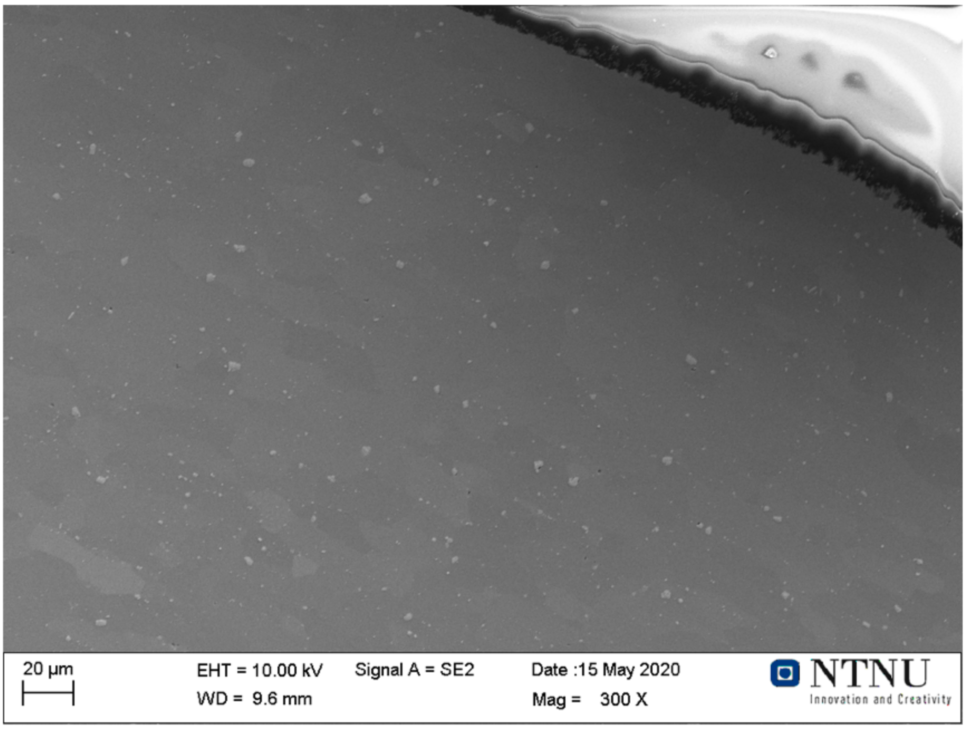

Figure 7.9: Scanning electron spectroscopy by secondary electron imaging of heat-treated (560 ^{circ}C in a *NaberthermN17/HR* thermal convection oven for 2h in inert argon atmosphere) 1,2 mm AA5183 welding wire commercially supplied by *Safra*.

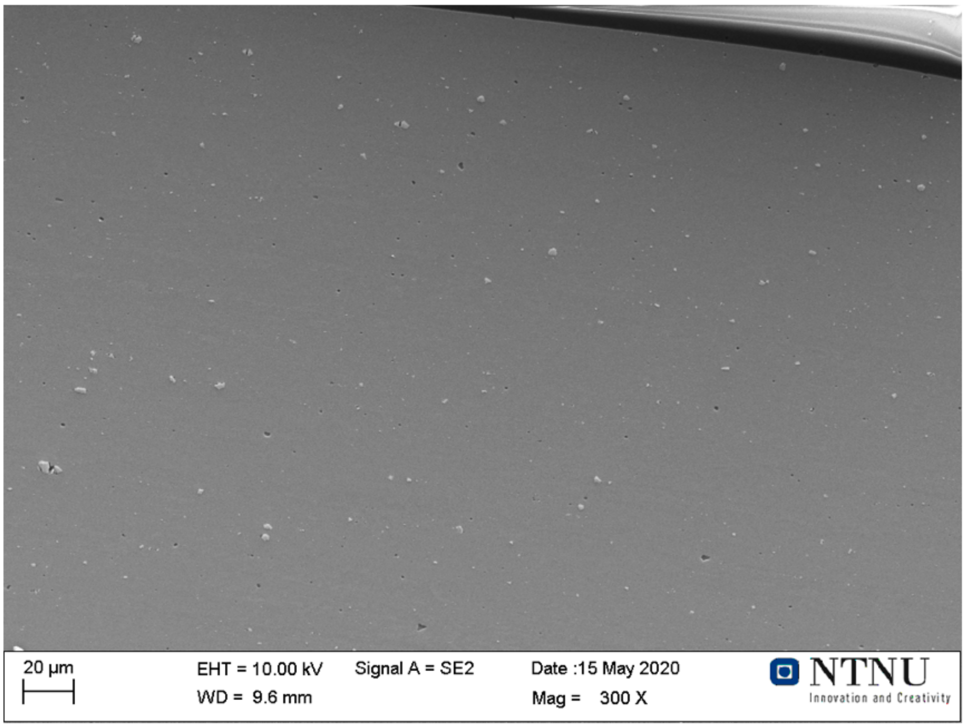

Figure 7.10: Scanning electron spectroscopy by secondary electron imaging of non-heat-treated (560 ^{circ}C in a *NabertherrmN17/HR* thermal convection oven for 2h in inert argon atmosphere) 1,2 mm AA5183 welding wire commercially supplied by *Safra*.

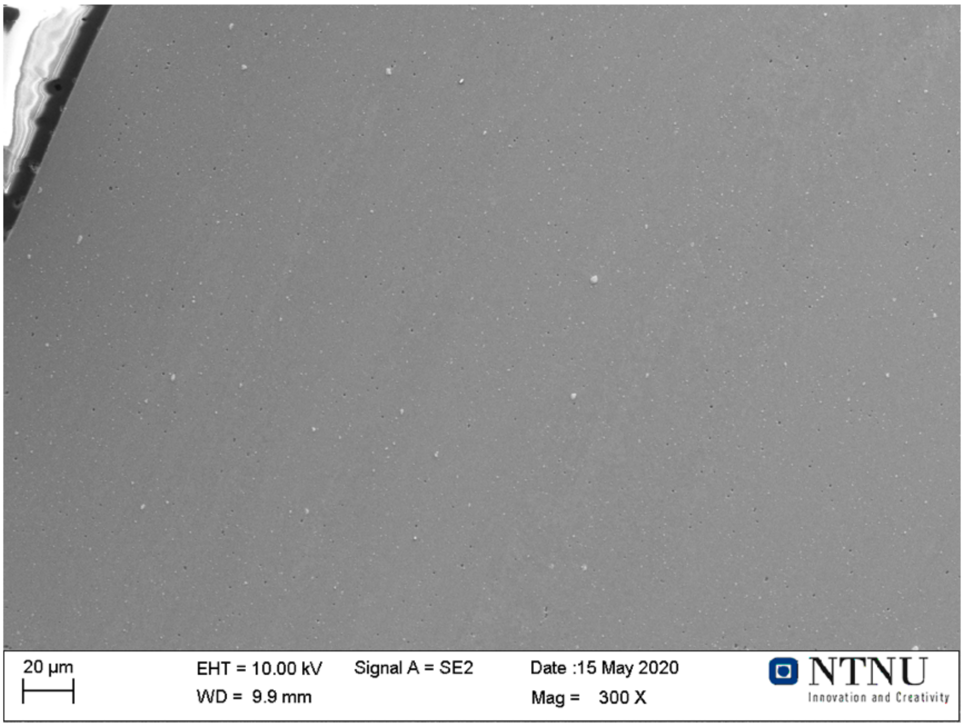

Figure 7.11: Scanning electron spectroscopy by secondary electron imaging of non-heat-treated (560 ^{circ}C in a *NabertherrmN17/HR* thermal convection oven for 2h in inert argon atmosphere) 1,2 mm AA5183-CG welding wire manufactured by MCSE

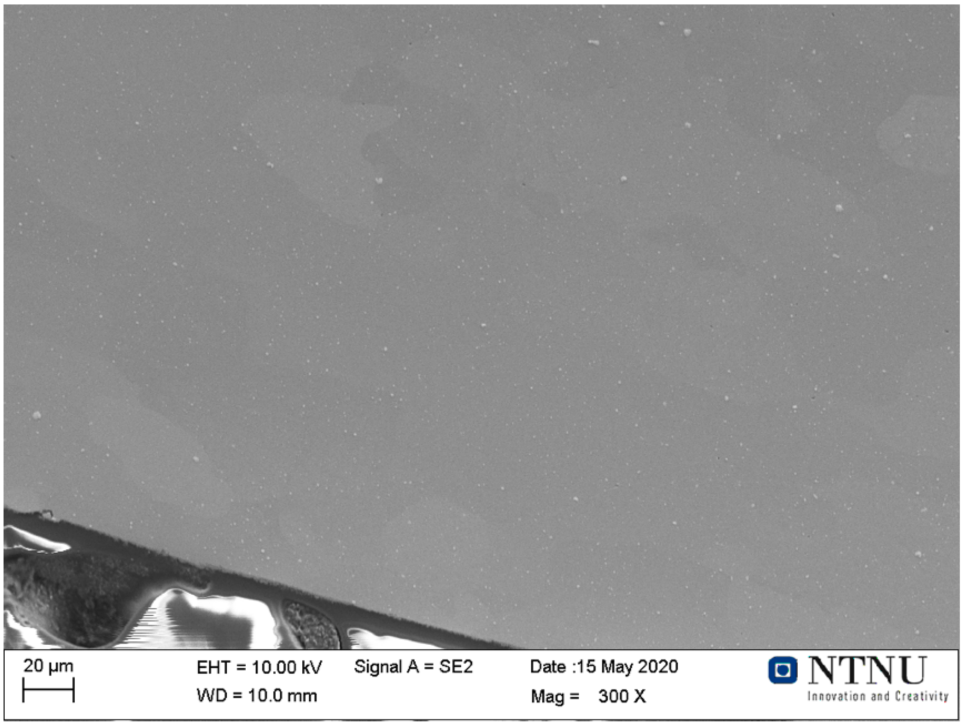

Figure 7.12: Scanning electron spectroscopy by secondary electron imaging of heat-treated (560 ^{circ}C in a *NabethermN17/HR* thermal convection oven for 2h in inert argon atmosphere) 1,2 mm AA5183-CG welding wire manufactured by MCSE

D Additional SEM images of porosity

Figure 7.13 show a overview image of porosity in the AA5183TiC-CG section of the WAAM thin wall. Figure 7.14 show a large pore, while **??** show the agglomeration of TiC nanoparticle and formation of oxides at the grain boundaries both in the pore and between grains.

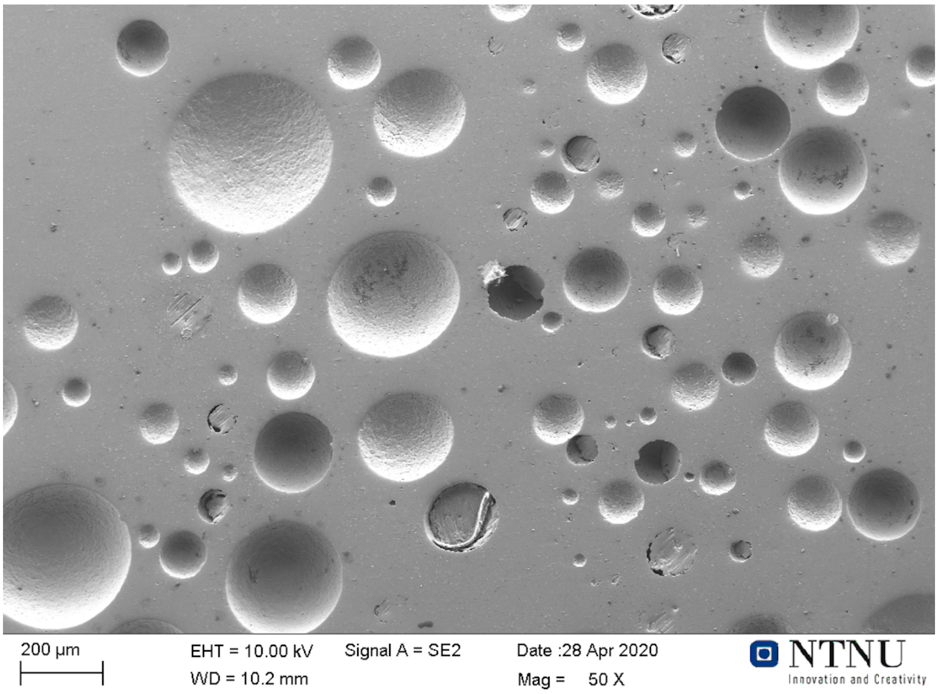

Figure 7.13: Scanning electron spectroscopy by secondary electron imaging of porosity in the AA5183TiC-CG section a the WAAM thin wall. Showing overview image of extreme porosity.

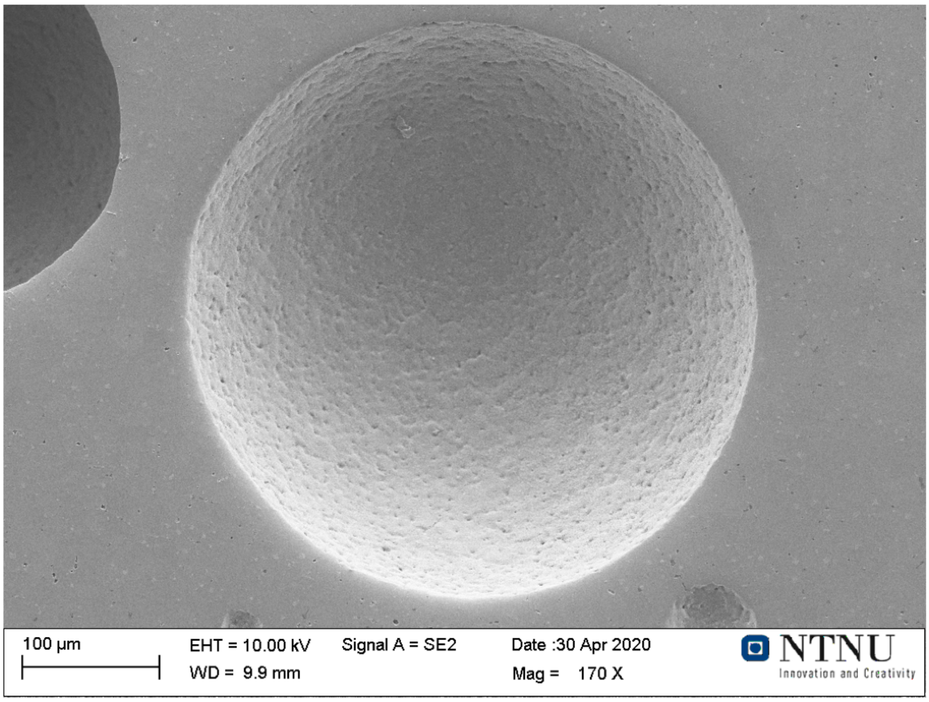

Figure 7.14: Scanning electron spectroscopy by secondary electron imaging of porosity in the AA5183TiC-CG section a the WAAM thin wall. Showing a large pore.

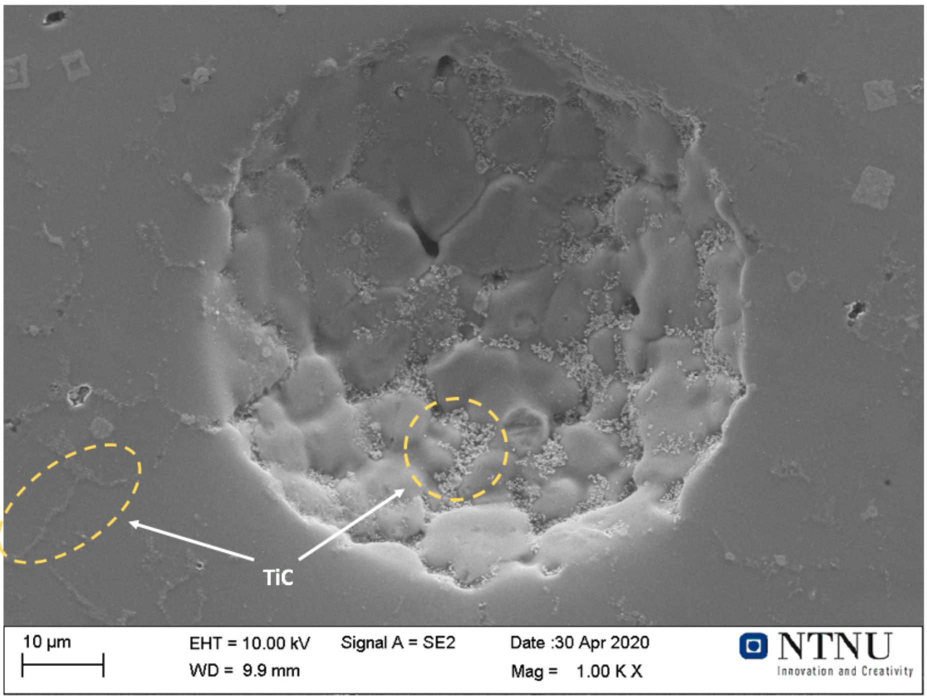

Figure 7.15: Scanning electron microscopy by secondary electron imaging show the AA5183TiC-CG section of WAAM thin wall. The image show agglomeration of TiC nanoparticles and growth of believed oxides at the grain boundaries.

Jan Eskil Flåm

NTNU
Norwegian University of
Science and Technology